Tropospheric Ozone Precursors: Global and Regional Distributions, Trends, and Variability

Yasin Elshorbany[1*], Jerald R. Ziemke[2], Sarah Strode[2,3], Hervé Petetin[4], Kazuyuki Miyazaki[5], Isabelle De Smedt[6], Kenneth Pickering[7], Rodrigo J. Seguel[8], Helen Worden[9], Tamara Emmerichs[10], Domenico Taraborrelli[10], Maria Cazorla[11], Suvarna Fadnavis[12], Rebecca R. Buchholz[9], Benjamin Gaubert[9], Néstor Y. Rojas[13], Thiago Nogueira[14], Thérèse Salameh[15], Min Huang[16]

[*]Correspondence to: elshorbany@usf.edu

[1] School of Geosciences, College of Arts and Sciences, University of South Florida, St. Petersburg, FL, USA

[2] NASA Goddard Space Flight Center, Greenbelt, Maryland, USA

[3]Goddard Earth Sciences Technology and Research (GESTAR II), Maryland, USA

[4]Earth Sciences Department, Barcelona Supercomputing Center, Barcelona, Spain

[5]Jet Propulsion Laboratory, California Institute of Technology, Pasadena CA

[6]BIRA-IASB, Ringlaan 3 Av. Circulaire, 1180 Brussels, Belgium

[7]Dept. of Atmospheric and Oceanic Science, University of Maryland, College Park, MD USA

[8]Center for Climate and Resilience Research, Department of Geophysics, Faculty of Physical and Mathematical Sciences University of Chile, Chile.

[9]Atmospheric Chemistry Observations and Modeling (ACOM), National Center for Atmospheric Research (NCAR), Boulder CO, USA.

[10]Institute of Energy and Climate Research, IEK-8: Troposphere, Forschungszentrum Jülich, Jülich, Germany.

[11]Universidad San Francisco de Quito USFQ, Instituto de Investigaciones Atmosféricas, Diego de Robles y Av Interoceánica, Quito, Ecuador.

[12]Center for Climate Change Research, Indian Institute of Tropical Meteorology, MoES, Pune, India.

[13]Department of Chemical and Environmental Engineering, Universidad Nacional de Colombia, Bogota, Colombia.

[14]University of São Paulo, São Paulo, Brazil.

[15] IMT Nord Europe, Institut Mines-Télécom, Univ. Lille, Centre for Energy and Environment, 59000, Lille, France. ~~IMT Lille Douai, Institut Mines-Télécom, Univ. Lille, Centre for Energy and Environment, F-59000 Lille, France.~~

[16] Earth System Science Interdisciplinary Center, University of Maryland, College Park, MD, USA.

Abstract

Tropospheric ozone results from in-situ chemical formation and stratosphere-troposphere exchange (STE), with the latter being more important in the middle and upper troposphere than in the lower troposphere. Ozone photochemical formation is nonlinear, and results from the ~~photochemical~~ oxidation of methane and non-methane hydrocarbons (NMHCs) in the presence of nitrogen oxide ($NO_x=NO+NO_2$). Previous studies showed that O_3 short- and long-term trends are nonlinearly controlled by near-surface anthropogenic emissions of carbon monoxide (CO), volatile organic compounds (VOCs), and nitrogen oxides. In addition, several studies have demonstrated the important role of STE in enhancing ozone levels, especially in the midlatitudes. In this article, we investigate tropospheric ozone spatial variability and trends from 2005 to 2019 and relate those to ozone precursors on global and regional scales. We also investigate the spatiotemporal characteristics of the ozone formation regime in relation to ozone chemical sources and sinks. Our analysis is based on remote sensing products of the Tropospheric Column of Ozone (TrC-O_3) and its precursors, nitrogen dioxide (TrC-NO_2), formaldehyde (TrC-HCHO), and total column of CO (TC-CO) as well as ozonesonde data and model simulations. Our results indicate a complex relationship between tropospheric ozone column levels, surface ozone levels, and ozone precursors. While the increasing trends of near-surface ozone concentrations can largely be explained by variations in VOC and NO_x concentration under different regimes, TrC-O_3 may also be affected by other variables such as tropopause height and STE. Decreasing or increasing trends in TrC-NO_2 have varying effects on the TrC-O_3, which is related to the different local chemistry in each region. ~~The concomitant increase or decrease in TrC-O_3 and TrC-NO_2 over the eastern US, and central Europe is due to dominant NO-sensitive conditions resulting from the strict measures to control NO_x emissions over the last two decades. The decreasing trends of TrC-NO_2 but increasing trends of TrC-O_3 in some regions in the central US and parts of eastern Asia are due to high NO_x conditions leading to VOC sensitivity in these regions.~~ We also shed light on the contribution of NO_x lightning and soil NO and nitrous acid (HONO) emissions to trends of tropospheric ozone on regional and global scales.

1.   Introduction

Tropospheric ozone (O_3) is an important air pollutant due to its diverse effects on air quality, ecosystem (Mills et al., 2018), health (Lefohn et al., 2018; Fleming et al., 2018), and climate (Boucher et al., 2013; Myhre et al., 2013; Zanis et al., 2022). O_3 is a photochemical product that results from the oxidation of methane (CH_4) and non-methane hydrocarbons (NMHCs) in the presence of nitrogen oxides (NO_x). Tropospheric ozone burdens can also be affected by stratosphere-troposphere exchange (STE) (Stohl et al., 2003; Zeng et al., 2010; Trickl et al., 2011; Li et al., 2024). O_3 is considered a short-lived climate forcer (SLCF) and is the third-most important greenhouse gas with a ~~global averagen~~ effective radiative forcing of (0.~~3447~~$^{+0.0923}_{-0.0623}$) W m^{-2}; Forster et al., 2021~~IPCC, 2023~~). Since the mid-1990s, free tropospheric ozone trends based on in situ measurement and satellite retrievals have increased with high confidence by 1-4 nmol mol^{-1} decade^{-1} across the northern mid-latitudes and 1-5 nmol mol^{-1} decade^{-1} within the tropics (Gulev et al., 2021). In the Southern Hemisphere, with more limited observation coverage compared with the Northern Hemisphere, the tropospheric column ozone shows an increase since the mid-1990s by less than 1 nmol mol^{-1} decade^{-1} with medium confidence at southern mid-latitudes (Gulev et al., 2021, Cooper at al., 2020). ~~Recent studies showed increasing trends of tropospheric O₃, especially in the temperate and polar regions of the Northern Hemisphere, while the evidence in the Southern Hemisphere is unclear (Tarasick et al., 2019; Archibald et al., 2020).~~ Tropospheric O_3 short- and long-term trends are nonlinearly controlled by anthropogenic emissions of carbon monoxide (CO), volatile organic compounds (VOCs), and nitrogen oxides (NO_x=NO+NO_2) as well as STE, especially in the midlatitudes (Li et al., 2024). Coupled Model Intercomparison Project Phase 6 (CMIP6) overestimates observed surface O_3 concentrations in most regions, with larger variability over Northern Hemisphere (NH) continental regions (e.g., Tarasick et al., 2019; Turnock et al., 2020). ~~The higher variability in the northern continental regions is due to the variable emissions of ozone precursors (i.e., CO, VOCs, and NO_x).~~ CMIP6 models simulate large increasing trends of surface concentrations of O_3 and $PM_{2.5}$ in East and South Asia with an annual mean increase of up to 40 ppb and 12 μgm^{-3}, respectively, over the historical periods (1850-2014; Turnock et al., 2020). However, these studies found also that CMIP6 models consistently underestimate $PM_{2.5}$ concentrations in the NH, especially during the winter months, and with larger variability near natural source regions, indicating missing sources (e.g., HONO) of O_3 (e.g., Elshorbany et al., 2014). Future scenarios show that emission control measures can influence future changes to air pollutants. Although the global increases in CH_4 abundance may offset benefits to surface O_3 from local emission reductions (Fiore et al., 2002; Shindell et al., 2012; Wild et al., 2012), recent reports (e.g., Zanis et al., 2022), showed the dominant role of precursor emission changes in projecting surface ozone concentrations under future climate change scenarios. In this study, we investigate the relation between ozone trends and the trends of its precursors.

Satellite observations have the advantage of large spatial and consistent temporal coverage. Tropospheric columns of ozone (TrC-O_3), in Dobson unit (1 DU=2.69×10^{20} molecules m^{-2}), are usually used to represent tropospheric ozone levels. The tropospheric column of a species is the species' concentration integrated from the surface to the top of the troposphere, the tropopause. The tropopause height is dynamically changing, and it varies over time, increasing or decreasing as a function of several factors, including tropospheric and stratospheric temperature (warming or cooling). Steinbrecht et al (1998) found that observed tropospheric warming of 0.7± 0.3 K per decade leads to an increase in the tropopause high and a decrease (at a rate of 16 DU/decade) in the observed column ozone levels. Similarly, after removing the

variations related to major natural forcings, including volcanic eruptions, ENSO (El Niño–Southern Oscillation), and QBO (Quasi–Biennial Oscillation), Meng et al. (2021) concluded that a continuous rise of the tropopause in the Northern Hemisphere (NH) from 1980 to 2020 is evident, which they related mainly to tropospheric warming caused by anthropogenic emissions. ~~Both~~ Steinbrecht et al (1998) and Meng et al. (2021) calculate the same rate of tropopause increase for the periods 1980-2000 and 1980-2020, respectively. ~~These results could affect calculated tropospheric ozone trends by changing the volume of the troposphere.~~ We investigate the trends in TrC-O$_3$ and ozone precursors at different column depths and determine their ~~causal~~ relationships.

Global models play a vital role in interpreting the observed trends in ozone precursors, verifying the consistency of emission inventories with observed precursor concentrations, and relating trends in ozone precursor emissions to ozone trends. Because satellite measurements are often sensitive to species concentrations above the surface, models provide additional information on the vertical distribution of ozone precursors needed to relate emissions or surface trends to a column or free tropospheric observations. For example, chemical transport models are used to relate Ozone Monitoring Instrument (OMI) NO$_2$ columns to surface NO$_2$ concentrations and their trends over the United States (e.g. Lamsal et al 2008, 2015; Kharol et al, 2015) since they provide vertical information on the NO$_2$ distribution. Models are also used to infer NO$_x$ emission trends from observations (e.g. Richter et al., 2005; Stavrakou et al., 2008; Miyazaki et al, 2016) or to examine whether simulations driven by state-of-the-art emissions inventories can reproduce observed changes in NO$_x$ (Itahashi et al., 2014; Godowitch et al, 2010). Models also provide insight into the role of background NO$_2$ versus local sources in relating satellite-observed NO$_2$ columns to NO$_x$ emissions changes (Silvern et al, 2019). Similarly, global models are vital for understanding trends in CO, since the lifetime of CO allows both local emissions and long-range transport and the global background to influence regional trends of CO and O$_3$. Duncan and Logan (2008) attributed the decreasing CO in the NH from 1998-1997 to decreasing European emissions and highlighted the role of Indonesian fires in driving interannual variability. Numerical models can also be used to assimilate satellite CO observations to invert for CO emission fluxes, often highlighting differences between bottom-up and top-down inventories (e.g., Kopacz et al., 2010; Fortems-Cheiney et al., 2011; Elguindi et al., 2020; Gaubert et al., 2020). For instance, several modeling studies found that the increasing emissions from China in recent years in some emission inventories were inconsistent with the negative trends observed by MOPITT (Yin et al, 2015; Strode et al., 2016; Zheng et al, 2019), while the decreases over the United States and Europe are supported by the observed decrease in CO. Jiang et al (2017) and Zheng et al (2019) also found that a decrease in biomass burning contributes to the negative CO trend in the NH. Mean calculated O$_3$ burden using CMIP6 simulation (Griffiths et al, 2021) revealed an increase of 44% from 1850 to the mean of the period of 2005-2014 and by another 17% until 2100 using the SSP370 experiments. Other sources of NO$_x$ such as lightning and soil emissions play an important role in controlling the O$_3$ budget, especially in low-NO$_x$ regions. We investigate these sources and the role they play in determining O$_3$ trends and variability on regional and global scales, as well as their determining factors.

Previous literature demonstrates the importance of controlling the emissions of ozone precursors to effectively reduce surface O$_3$ levels. Therefore, a thorough and rigorous understanding of the trends and variability for O$_3$ precursors is of paramount importance for a global abatement strategy of O$_3$ levels. In this study, we use ozonesonde, remote sensing, and

158 global models to evaluate tropospheric O_3 and O_3 precursor trends of CO, HCHO, and NO_2,
159 on regional and global scales.

2. Methodology

2.1. Trend Analysis

162 We analyze the historical trends of tropospheric ozone and its precursors CO, NO_2, and HCHO,
163 from 2005 to 2019. For trend analysis, we use two methods, the Quantile regression (QR)
164 method (Chang et al., 2023), and the Weighted Least Squares (WLS). For NO_2~~,~~, CO, and HCHO
165 ~~, and CO~~ trends are calculated based on the QR method (Chang et al., 2023), as follows: (1) we
166 first compute the deseasonalized monthly time series of NO_2 and HCHO tropospheric columns
167 (hereafter referred to as TrC-NO_2, TrC-HCHO), and CO atmospheric column (TC_CO), (2) we
168 use the quantile regression method for computing the trend, focusing here on the median, and (3)
169 uncertainties at a 95% confidence level are estimated using the block bootstrapping approach,
170 through 1000 iterations with blocks size of $N^{0.25}$ with N the number of monthly values. They are
171 calculated over a 1°x1° grid and only in cells where at least 75% of the monthly values are
172 available. TC_CO column (see sec. 2.2.1) time series trends are also calculated as Weighted
173 Least Squares (WLS) of the monthly anomaly, weighted by the monthly regional standard
174 deviation (for comparison with the QR method). ~~For the CO trend map, we use a 12-month~~
175 ~~running average before computing the linear trend (Buchholz et al., 2021).~~ The tropospheric
176 ozone column (TrC-O_3), trends are calculated based on the WLS method.~~.~~ Tropospheric columns
177 of satellite observations are calculated based on the WMO thermal definition of the tropopause.
178 To account for varying tropospheric column definitions used in previous literature, we also
179 evaluate the trends at ~~different~~ varying column depths.

2.2. Data resources

181 In this section, we present the different data repositories and their characteristics.

2.2.1. Satellite data

183 A list of the applied satellite data products and their resolution is shown in Table 1~~Table 1~~. For
184 Tropospheric ozone data, we use the Ozone Monitoring Instrument/Microwave Limb Sounder
185 (OMI/MLS) product (Ziemke et al., 2006). The OMI/MLS product is the residual of the OMI total
186 ozone column and the MLS stratospheric ozone column, available as gridded monthly means. The
187 tropospheric NO_2 column retrievals used were the QA4ECV project (http://www.qa4ecv.eu/ecvs)
188 version 1.1 level 2 (L2) product for OMI (Boersma et al., 2017a), GOME-2 (Boersma et al.,
189 2017b), and SCIAMACHY (Boersma et al., 2017c). The ground pixel sizes of the OMI, GOME-
190 2, and SCIAMACHY retrievals are 13 km×24 km, 80 km×40 km, and 60 km×30 km, with local
191 Equator overpass times of 13:45, 09:30, and 10:00 LT, respectively. We also use HCHO
192 tropospheric columns retrieved from OMI (De Smedt et al. 2018) from the QA4ECV project.
193 Atmospheric total column CO daytime observations were obtained from the MOPITT instrument
194 aboard the Terra Satellite (Barret et al., 2003; Buchholz et al., 2017). Monthly daytime L3 data
195 were obtained at 1º gridded horizontal resolution from the NASA Langley Research Center
196 Atmospheric Science Data Center (ASDC, 2024), using version 9 (V9) retrievals, and the joint
197 near-infrared/thermal-infrared product (Deeter et al., 2022).

198

199 Table 1: Satellite data products and their reference periods.

Parameter	Resolution (Satellite pixel size)	Instrument/Platform	Reference Period	Reference
NO_2	1°x1° (13 km x 24 km)	OMI/Aura	2005–2020	Boersma et al., 2017a
NO_2	1°x1° (40 km x 80 km)	GOME-2/METOP-A	2007–2018	Boersma et al., 2017b
NO_2	1°x1° (30 km x 60 km)	SCIAMACHY/ENVISAT	2005–2011	Boersma et al., 2017c
CO	1°x1° (22 km x 22 km)	MOPITT/TERRA	2002–2020	Deeter et al., 2022
HCHO	1°x1° (13 km x 24 km)	OMI/Aura	2004–2020	De Smedt et al., 2018
Ozone	1°x1°	OMI/MLS	2004–2020	Ziemke et al., 2006

200

2.2.2.   Ozonesonde Data

Direct sampling of ozone throughout the atmospheric column by ozonesondes on board of high-altitude balloons is a primary source of information of the ozone abundance and changes in the free troposphere. Ozonesonde data have been used extensively for satellite ozone product validations, trend analyses, and as a priori climatology profiles for satellite retrieval algorithms (McPeters and Labow, 2012; Labow et al., 2015; Hubert et al., 2021; Christiansen et al., 2022; Newton et al., 2016). Ozonesondes networks around the globe have been providing the ozone community with accurate in situ measurements of high vertical resolution (100-m) for the last 5 decades in the Northern Hemisphere (Krizan and Lastovicka, 2005), nearing 3 decades at stations in the tropics (Thompson et al., 2017), and in the last decade, new efforts are contributing with data from undersampled regions such as the tropical Andes (Cazorla and Herrera, 2022). Other important contributions include dedicated campaigns for regional studies (i. ee.g. Newton et al., 2016; Fadnavis et al., 2023). Figure 1 shows a map with ozonesonde stations around the globe whose data are publicly available from data providers (station names, coordinates, and links for data access in the Supplementary Material, Table S1). In this work, we present a review of ozonesonde trends calculated and published in previous studies (Wang et al., 2022 and Christiansen et al., 2022).

218
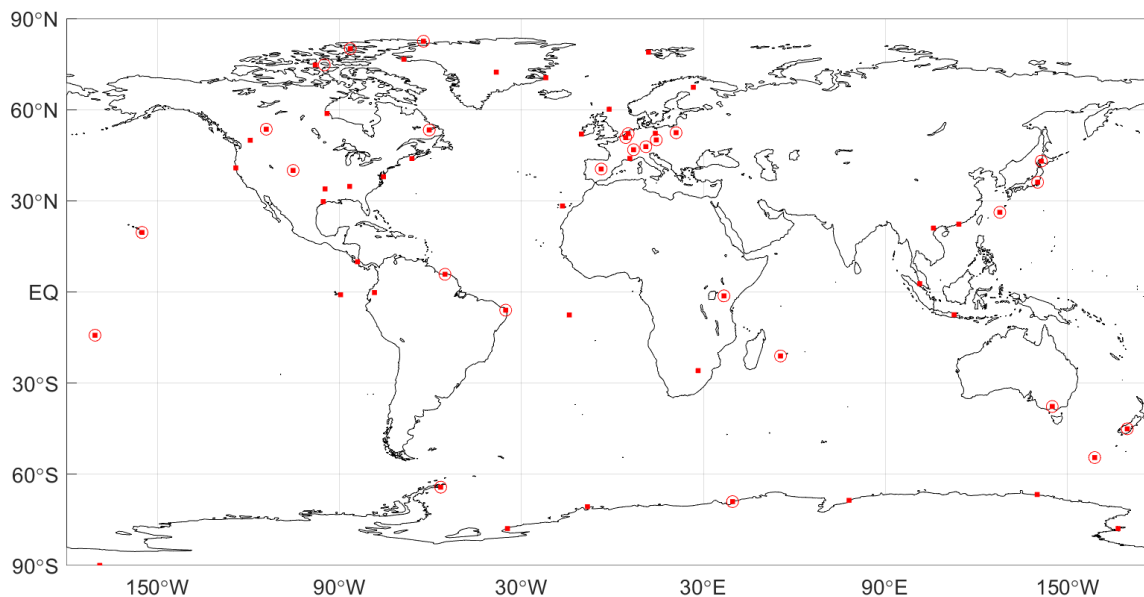
219

220 Figure 1: Ozone-sounding stations around the globe (red squares) whose data are publicly
221 available (Table S1). Stations that meet the criteria to calculate trends (Wang et al., 2022) are
222 circled in red.

223

2.2.3. Model simulations of ozone precursors and their vertical distribution

225 Model simulations provide information on the vertical distribution of trace gases that can help
226 interpret the observed columns. Here, we use ~~the~~ a Goddard Earth Observing System (GEOS)
227 Earth System Model (Molod et al, 2015) simulation run~~ning~~ with the GMI chemistry mechanism
228 (Duncan et al, 2007; Strahan et al, 2007; Nielsen et al, 2017) to simulate the contributions of the
229 lower, middle, and upper troposphere to the tropospheric columns of ozone and its precursors.
230 The model configuration is described in Fisher et al (2024) and summarized here. The MERRA-
231 2 reanalysis (Gelaro et al., 2017) constrains the GEOS-GMI meteorology. The GEOS-GMI
232 meteorology is replayed to the MERRA-2 meteorology as described in Orbe et al (2017).
233 Anthropogenic emissions of NO_2, CO, and VOCs are based on the MACCity inventory (Granier
234 et al, 2011) through 2010 and the RCP8.5 emissions afterward, with NO_2 emissions scaled based
235 on OMI. The emissions are downscaled to higher resolution using the EDGAR 4.2 emission
236 inventory (Janssens-Maenhout et al., 2013). Biomass burning emissions for the analysis period
237 come from the Fire Energetics and Emissions Research (FEER) product (Ichoku and Ellison,
238 2014). Liu et al (2022) evaluated another GEOS simulation with GMI chemistry with satellite
239 observations of $TrC-O_3$, $TrC-NO_2$, $TrC-HCHO$, and $TC-CO$.

3. Data Analysis and Discussion

3.1. $TrC-O_3$ Sensitivity to Tropopause

242 Calculated $TrC-O_3$ depends on several factors such as tropospheric ozone levels, atmospheric
243 warming (e.g., due to GHG emissions) or cooling (stratospheric or tropospheric (e.g., after major
244 volcanic eruptions), and tropopause height (TH). Atmospheric warming or cooling can lead to a
245 decrease or an increase, respectively, of $TrC-O_3$ due to the respective change in the TH. Several
246 methods are used to determine the TH. The WMO thermal definition ~~(WMO)~~ for the first TH,
247 the lowest altitude level at which the lapse rate decreases to 2º K km⁻¹ or less, provided that the
248 average lapse rate between this level and all higher levels within 2 km does not exceed 2º K km⁻

249 [1]. A second tropopause may be also found if the lapse rate above the first tropopause exceeds
250 3°K km^{-1} (WMO, 1992; Hoffmann and Spang (2022). Other studies define the TH based on
251 fixed pressure levels (from ground to 150, 200, 300, and 400 hPa). Mean OMI/MLS TrC-O$_3$
252 values in July (2005-2019) calculated based on the WMO thermal definition, are shown in
253 Figure 2. TrC-O$_3$ values are comparable to previously reported CMIP6 and satellite
254 measurements (Griffiths et al., 2021). Partial ozone columns (OC) calculated from the ground to
255 different pressure levels, 150, 200, and 300 hPa show increasing OC values with increasing
256 column depth, with calculated OC at 150 and 200 hPa being the closest to the TrC-O$_3$ WMO
257 values, still overestimating OC in the northern hemisphere (50-90° N), especially for the 150 hPa
258 OC, see Figure 2.

259
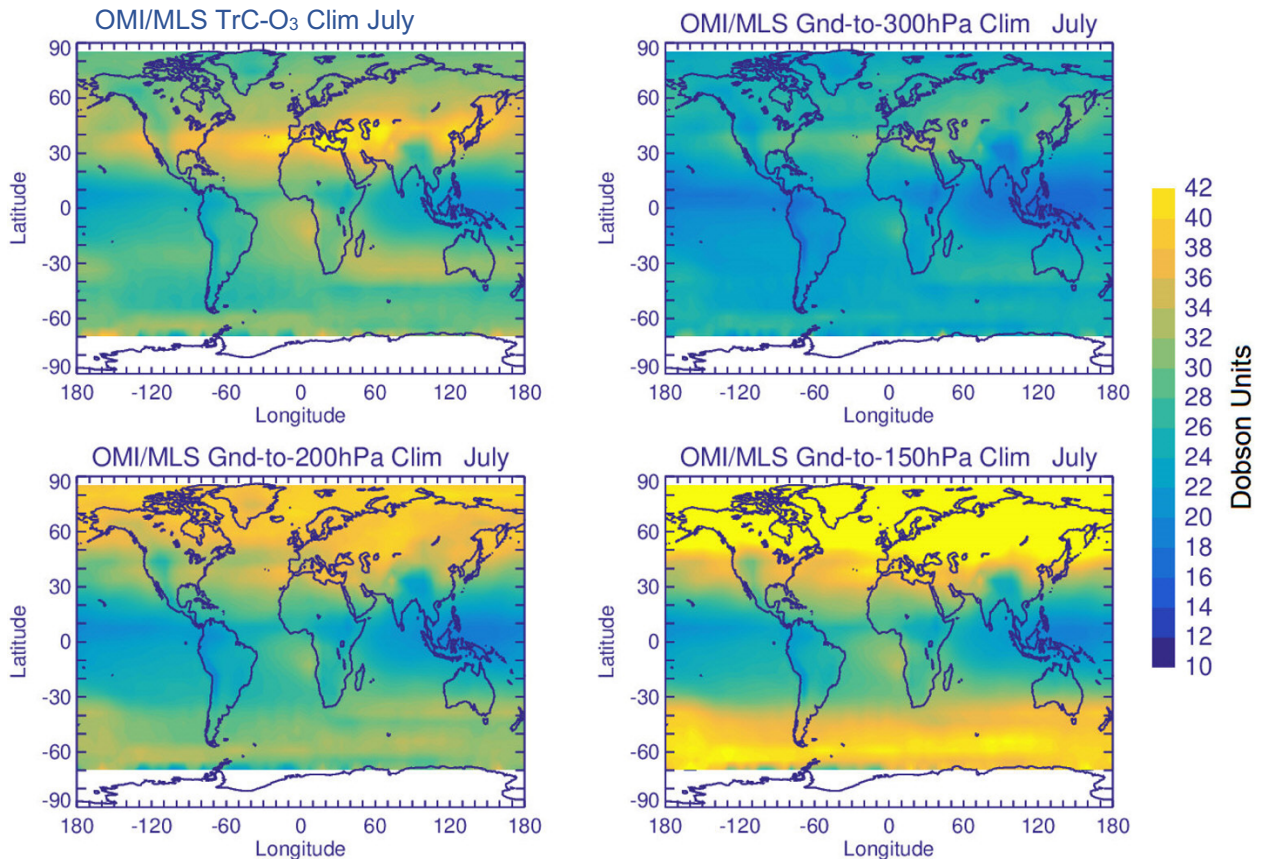
261 Figure 2: Global Mean (2005-2019) Column Ozone based on the WMO definition, ~~as well as~~
262 ~~to~~and for different ~~pressure levels~~column depths.

263

264 Steinbrecht et al (1998) found that observed tropospheric warming of 0.7± 0.3 K per decade
265 leads to an increase in the TH and a decrease in total ozone. They also calculated a decrease of
266 16 DU per ~~/k~~kilometer~~m~~ increase in TH. These results indicate the importance of TH on
267 calculated long-term ozone trends. This could also affect comparisons between trends calculated
268 based on different TrC-O$_3$ definitions and near-surface ozone levels. The time series of
269 deseasonalized TH from 2004 to 2021 are shown in Figure 3 together with their zonal mean
270 trends. Trends in TH are positive reaching 60 meters/decade except in a narrow band in the
271 tropics from 10°S to 20°N and at 30°S, where TH decreases at a rate up to 30 meters/decade. TH
272 in the tropical regions is also characterized by high variability (see Figure 3). These results are

273 also consistent with recent reports showing a positive trend of TH from 20-80ºN at a rate of 50-
274 60 m/decade (Meng et al., 2021). They related this increase primarily to tropospheric warming.
275 ~~The decrease of the TH in the tropics may contribute by some extent to the increasing TrC-O₃~~
276 ~~trend in this region (see sec. 3.4).~~ These results show ~~also~~ that using a fixed pressure level for the
277 tropopause may not be accurate given the change in TH over time. In the following sections,
278 tropospheric columns will be calculated based on the WMO tropopause definition.
279
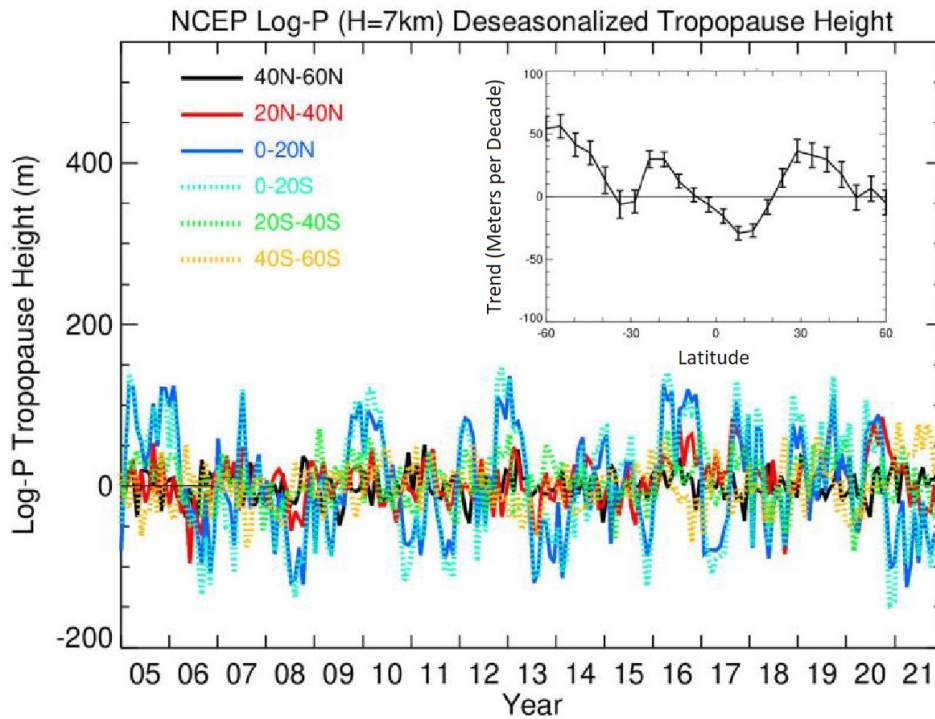
281 Figure 3: National Centers for Environmental Prediction (NCEP) WMO (2K/km) tropopause
282 log-P height time series with trends (meters/decade) embedded.

283

284 **3.2. Spatial Distribution of O₃ and its Precursors**

285 Tropospheric O_3 results from in-situ photochemical formation and STE. is a In-
286 situphotochemical product thatO_3 results from the photolysis of NO_2. Therefore, the sources and
287 fate of NO_2 in the atmosphere determine O_3 burden and distribution. NO_2 is formed from the
288 reaction of hydrogen proxyperoxyl (HO_2) and alkyl proxyperoxyl (RO_2) radicals with NO (R
289 3.2-1R 3.2-1). While photolysis of NO_2 is the main source of ozone, high NO_2 levels can
290 suppress O_3 levels as NO_2 reacts with OH radical forming HNO_3 (R 3.2-2R 3.2-2 to R 3.2-4R
291 3.2-4), thus reducing the oxidation rate of hydrocarbons and respectively HO_2 and RO_2 levels,
292 leading to a net loss of O_3 (e.g., Finlayson-Pitts and Pitts, 2000; Elshorbany et al., 2010,
293 Archibald et al., 2020). Ozone production efficiency is calculated as the ratio of the number of
294 NO_2 molecules photolyzed to form O_3 to that lost due to the reaction with OH forming HNO_3.
295 Under NO-sensitive conditions, the decrease in NO_x leads to a reduction in OH, HCHO, and O_3.
296 However, under high NO conditions, a reduction in NO_x could lead to an increase in
297 photochemical products, OH, HCHO, and O_3 because a reduction in NO_2 leads to a decrease in
298 OH loss rate, thus higher HO_2 and RO_2 production (Elshorbany et al., 2009; 2010; 2012;
299 Archibald et al., 2020).

300	R 3.2-1	HO_2/RO_2	+	NO			$\rightarrow$	NO_2		
301	R 3.2-2	NO_2	+	$h\nu$ ($h\nu < 424$ nm)			$\rightarrow$	$O(^3P)$	+	NO
302	R 3.2-3	$O(^3P)$	+	O_2	+	M	$\rightarrow$	O_3	+	M
303	R 3.2-4	OH	+	NO_2 (M)			$\rightarrow$	HNO_3 (M)		
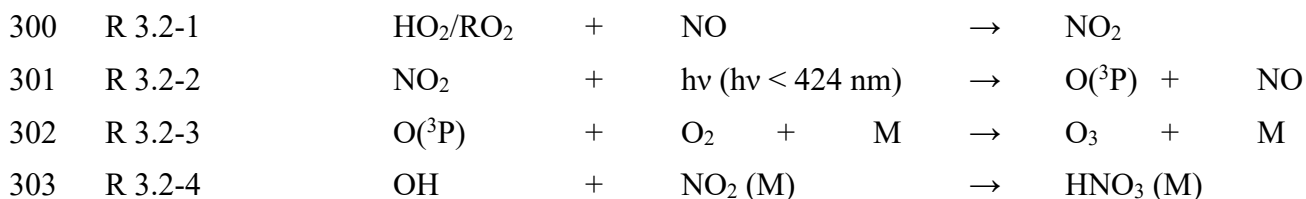
304

305 While this paper focuses on ozone precursors with higher reactivity, we note that methane, with
306 an assessed total atmospheric lifetime of 9.1 ± 0.9 years (Szopa et al., 2021), is also a crucial
307 driver (Fiore et al., 2002; Isaksen et al., 2014), given its accelerated growing rate of 7.6 ± 2.7
308 nmol mol^{-1} yr^{-1} between 2010 and 2019 (Canadell et al., 2021), largely driven by anthropogenic
309 activities (Szopa et al., 2021).

310 The observed mean tropospheric columns of O_3, NO_2, and HCHO and atmospheric column of
311 CO from 2005 to 2019 are shown in Figure 4. The unit for column number density is
312 Pmolec/cm^2 ($\times 10^{15}$ molecules per square centimeter), except for TrC-O_3, which is Dobson. NO_2
313 concentration has ~~been decreasing since 2005 in North America, Europe, and Australia, mainly~~
314 ~~due to the applied~~decreased since 2005 in North America, Europe, and Australia, mainly due to
315 strict measures to reduce air pollution (Lamsal et al., 2015). Since O_3 is a photochemical product
316 that is formed based on non-linear chemistry, a reduction in NO_2 may lead to an increase or
317 decrease in tropospheric O_3 levels based on the dominant photochemical regime in the respective
318 region. In addition, tropospheric ozone levels, especially in the middle and upper troposphere
319 may be affected by STE (Li et al., 2024). The highest values of the NO_2 tropospheric column are
320 in the northern hemisphere between 10 ºN and 50ºN, especially over the eastern US, northern
321 Europe, and east and south Asia, with elevated levels in the Southern Hemisphere (SH) between
322 10 and 30ºS, especially in sub-Saharan Africa, and Brazil. TrC-O_3 is also highest over the band
323 of 20-50º N, especially over the eastern coast of the US, southern Europe, and east Asia. Some
324 differences exist between TrC-O_3 and TrC-NO_2 spatial patterns which is due to factors including
325 ~~the~~ different lifetime, photochemical sensitivity (see sec. 3.4), and STE.~~3.4).~~ On average, the
326 northern hemisphere has higher TC-CO than the southern hemisphere due to a larger number of
327 sources (Buchholz et al., 2021). Additionally, high amounts of CO are found in regions with
328 large anthropogenic sources (e.g., eastern China) or in regions with large and regular fire seasons
329 (e.g., central Africa) (Buchholz et al., 2021). HCHO and CO show a similar spatial pattern over
330 western Africa due to emissions from biomass burning (Marais et al., 2012, Buchholz et al.,
331 2021). In the following sections, global and regional trends of TrC-O_3 are investigated along
332 with tropospheric ozone precursors.

333
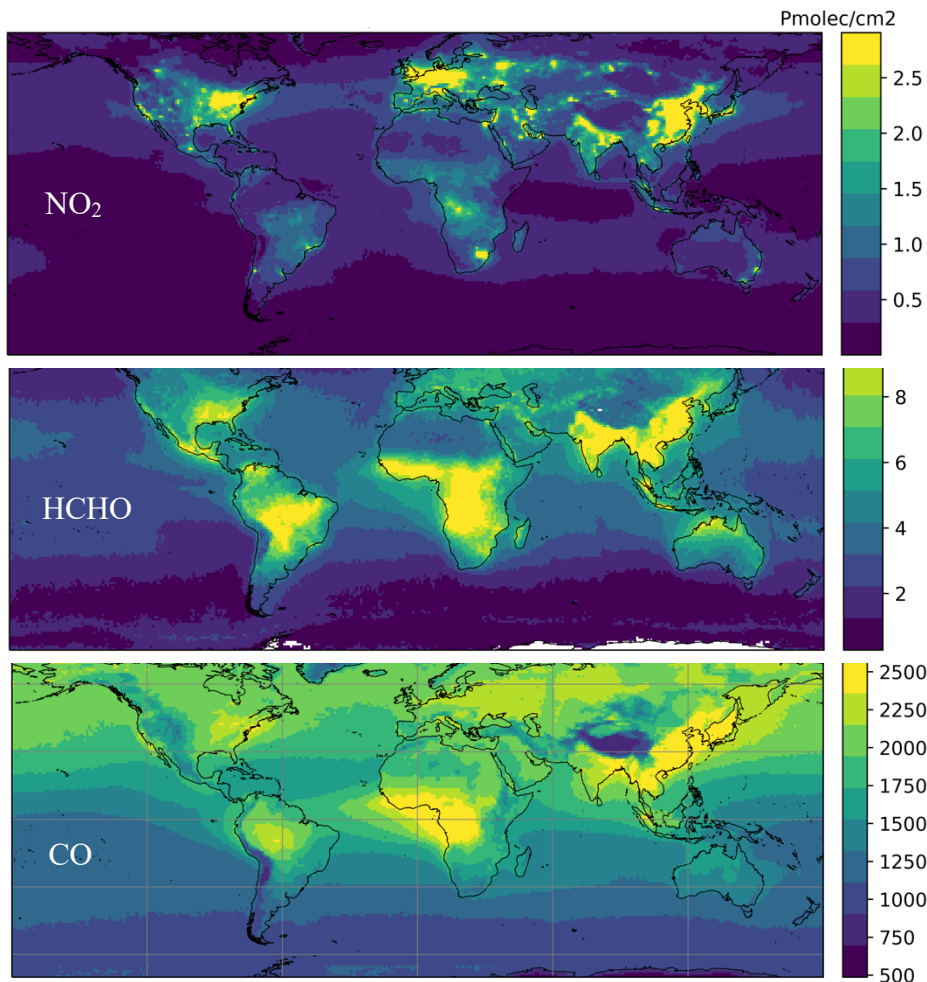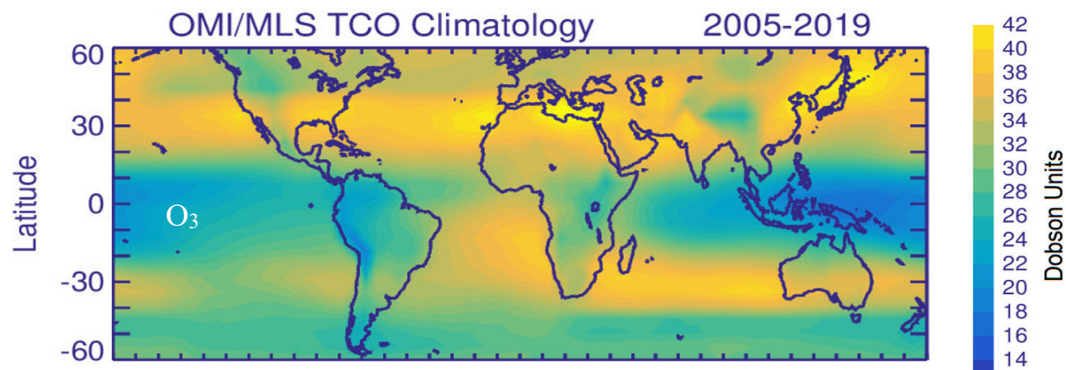
Figure 4: Mean (2005-2019) of TrC-O_3, TrC-NO_2, TrC-HCHO, and TC-CO.

3.3. Simulated O_3 Precursors

Ozone and its precursors differ in their vertical distribution through the troposphere. In this section, we use the GEOS ~~GMI~~ simulations to show how the lower, middle, and upper troposphere contribute to the simulated columns of O_3 and its precursors to complement the column information from satellites. Figure 5 shows the simulated mean (2005-2019) contributions to tropospheric columns of O_3, NO_2, formaldehyde, and CO, partitioned into the lower (up to 700hPa), middle (700-400hPa), and upper (400hPa to tropopause) portions of the troposphere~~opause~~ for the tropical band (30ºS:30ºN) and the global mean. The middle and upper

344 troposphere make large contributions to the simulated TrC-O₃ and its variability (Figure 5)₅.
345 ~~while~~ Tthe lower troposphere makes the largest contribution to the TrC-HCHO ~~column~~ since it is
346 mainly a photochemical product (e.g., Elshorbany et al., 2009), and all three levels make
347 substantial contributions to the CO column. Globally, the relative contributions for TrC-O₃, TrC-
348 HCHO and CO are similar to those of the tropics. However, for TrC-NO₂ the lower troposphere
349 make~~ss the~~ a smaller contribution in the tropics than globally~~largest contribution to the simulated~~
350 ~~tropospheric NO₂ column due to the larger NOₓ emissions in the northern hemisphere~~.

351
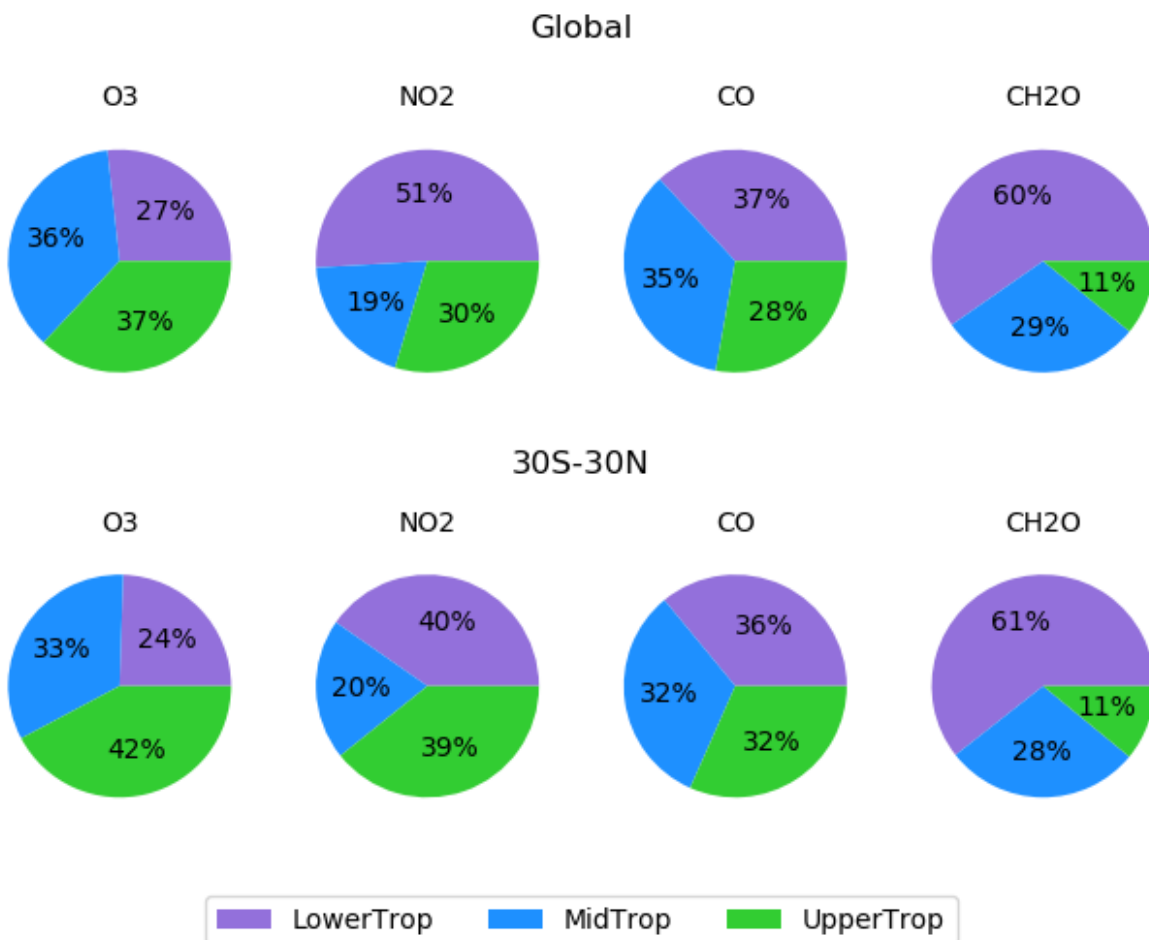
352
353 Figure 5: Simulated average (2005-2019) contributions to the tropospheric columns of O₃, NO₂,
354 formaldehyde, and CO from the lower (surface-700hPa), middle (700-400hPa), and upper
355 troposphere (400hPa-tropopause) using NASA GEOS5-GMI. The top row is for the global
356 mean, while the bottom row is averaged from 30°S-30°N.

3.4. Tropospheric Trends

3.4.1.   Global Tropospheric Ozone

359 Global TrC-O₃ trends calculated for different column depths are shown in Figure 6. Compared to
360 TrC-O₃, OC trends up to 150 hPa seem to be the closest despite OC values being much higher
361 than that of the TrC-O₃ (Figure 2). All significant trends are positive indicating increasing trends
362 of ozone columns, regardless of the tropopause height. Insignificant (at 2 σ levels) decreasing
363 TrC-O₃ trends were also found in some locations, e.g., South Australia, South Africa, and the

364 northeastern coast of the US. ~~As mentioned in sec. 3.1, TrC-O₃ trends in the northern tropics may~~
365 ~~be slightly enhanced by the decreasing TH trends in that region (Steinbrecht et al., 1998). In~~
366 ~~contrast, increasing TrC-O₃ trends in other regions may be slightly offset by the increasing TH~~
367 ~~trends (see Figure 3).~~ Increasing trends in the northern midlatitudes may also be partially related
368 to STE (Willimas et al, 2019; Li et al., 2024)
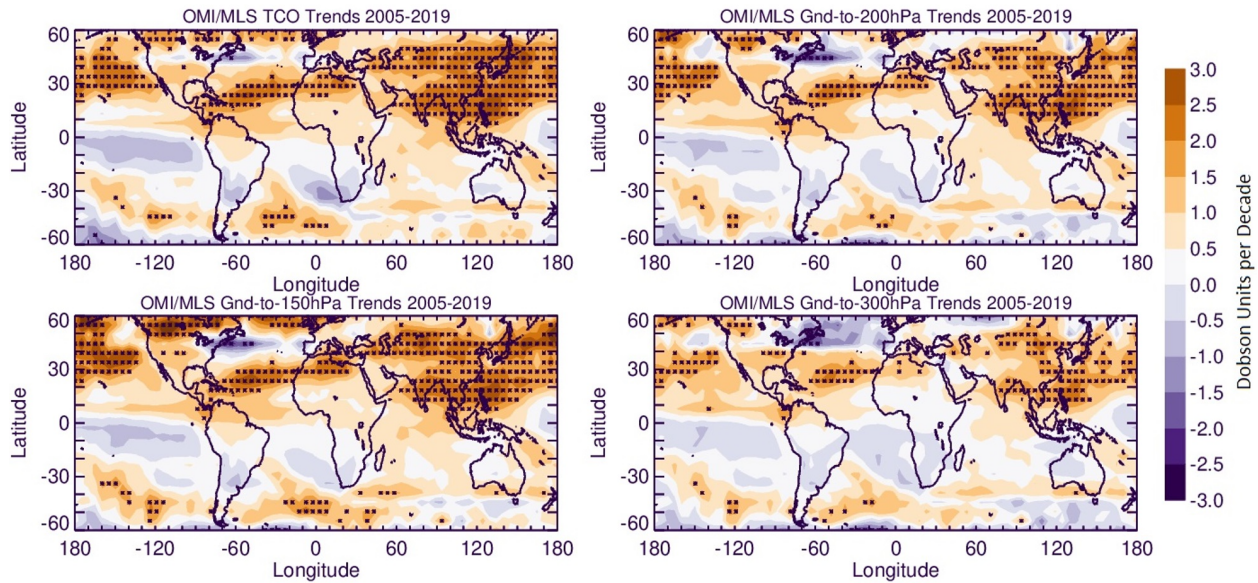
369

370 Figure 6: Trends in tropospheric column ozone, based on the WMO thermal definition, and the
371 trends on ozone columns (from ground to 150, 200, and 300 hPa). Trends are calculated based on
372 deseasonalized monthly data from 200~~4~~5 to 201~~1~~92. Asterisks denote significant trends
373 (different from zero at 2σ level).

374

375 The time series of OMI/MLS TrC-O₃ averaged over several latitudinal bands ~~as well as~~and at
376 different column depths are shown in ~~Figure 7~~Figure 7. Zonal mean TrC-O₃ compares well with
377 partial ozone columns in the tropics (from 30ºS to 30ºN) with the OC of up to 300 hPa differing
378 by about 10 DU from the TrC-O₃ (~~Figure 7~~Figure 7b). The lowest TrC-O₃ trends are located in
379 the northern hemisphere (30~~ºN~~— 60ºN) at 0.78±1.16 DU/decade, followed by the southern
380 hemisphere (30~~ºS~~ -60ºS (0.95±0.75 DU/decade) and the tropical band (30~~ºS~~ -30ºN (1.06±0.40
381 DU/decade). In addition, the continental trends over Australia, South Africa, and South America
382 in the 30 ºS -60ºS band are essentially negative and the positive trends in this band are ~~driven~~
383 ~~com~~antributed ma~~inly~~ by oceanic ~~emissions~~ regions (see (Figure 6). The positive trends in the
384 30ºN -60ºN band are slightly offset by the negative trends over the northe~~E~~astern US and
385 western Europe (see Figure 6).

386
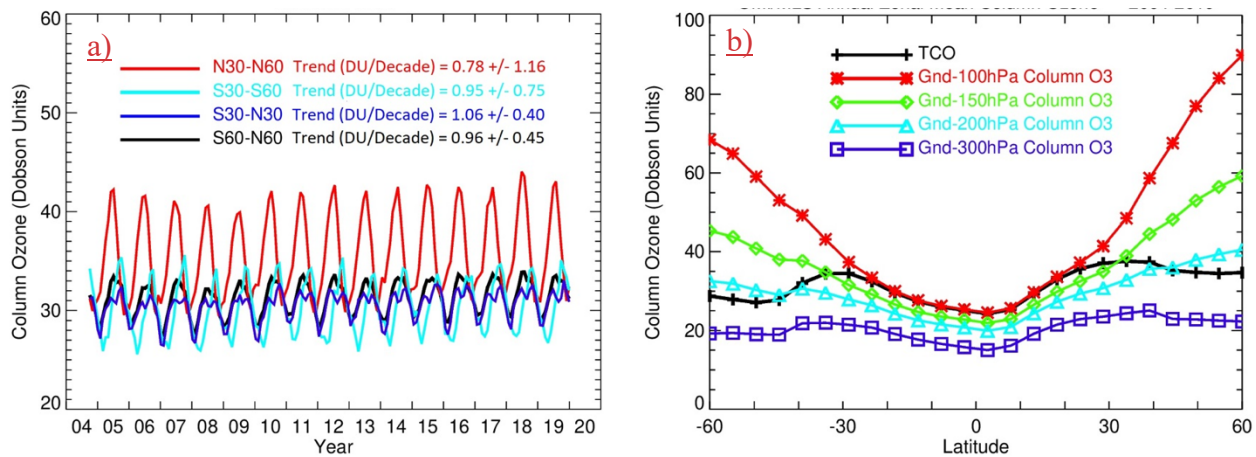
387

388 Figure 7: Time series and zonal mean trends of OMI/MLS TrC-O₃ in different latitudinal bands
389 (left) and zonal mean of different column depths (right) from 2005-2019.

390

391   Observed trends for the time period before COVID-19 (2005-2019) show that OC trends
392 were highest in the northern latitudes (0-30º N) reaching about 1.5 DU/decade, followed by the
393 northern midlatitudes 30-60ºN (Figure 8). The high trends in the 30-60ºN band are dominated by
394 transpacific impacts as well as some impacts from East Asia. The positive trends in the southern
395 hemisphere (0-30º S) are mainly over Amazonia and Southeast Asia, being offset by small
396 negative trends over Western Australia and South Africa. The trends during the time period
397 (2005-2021) show a ~~significant~~ decline in O₃ column trends in the northern hemisphere but a
398 slightly increasing trend in the southern hemisphere (Figure 8b). The decreasing trends in the
399 northern hemisphere during the COVID-19 is consistent with previous literature showing a
400 ~~significant~~ decrease in several pollutants including NO₂ and O₃ due to the extended lockdown
401 periods imposed during the pandemic (e.g., Bauwens et al., 2020; Elshorbany et al., 2021;
402 Steinbrecht et al., 2021; Putero et al., 2023). The decrease of NO₂ ~~under the dominant NO~~
403 ~~sensitive conditions~~ in some parts of Europe and the northeastern USA led to a decrease in
404 tropospheric O₃. ~~The increase in the southern hemisphere is due to a variety of reasons including~~
405 ~~the lesser impact of the pandemic (Oleribe et al., 2021), and persistent pollution issues, even~~
406 ~~during the pandemic (Matandirotya et al., 2023). In addition, most regions in the southern~~
407 ~~hemisphere are VOC-sensitive regions, conditions under which the reduction in NO₂ would lead~~
408 ~~to an increase in tropospheric O₃ (see sec. 3.4)~~

409   Zonal mean trends (Figure 8) show that OC up to 150 hPa is almost identical to that of
410 TrC-O₃ except for the high latitudes 45º-60º S and 45º-60º N. The decreasing trends above 30ºN
411 and 30ºS are due to the offsetting impact of negative trends over the northe~~E~~astern US and
412 western Europe in the north, and Australia and South Africa in the south, respectively. This
413 impact is less apparent in the 150 hPa OC due to the lower positive trends in that band compared
414 to TrC-O₃. The 200 hPa OC comes next with a very good agreement from 60º S to 10º N.
415 followed by the 100 hPa which is only in good agreement from 30º S to 30ºN, while the 300 hPa
416 OC was the farthest from the TrC-O₃. The decrease of O₃ in the northeastern US and western
417 Europe is ~~a result of~~consistent with decreasing NO₂ trends ~~demonstrating the~~and NO-sensitive
418 conditions dominating these regions. The decreasing trends ~~of O₃ over Eastern US and Europe~~
419 ~~are consistent with the decreasing trend~~ of NO₂ (see below) ~~, which is~~are due to the successful
420 measures applied since 2004 to mitigate air pollution in these regions. ~~The decrease of O₃ is a~~

423

424

425

426
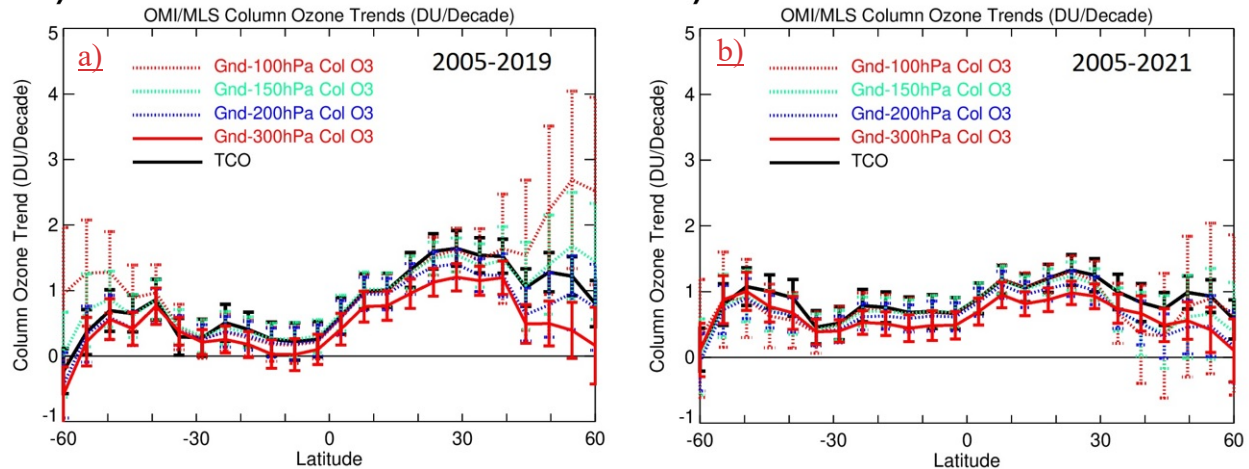
Figure 8: Tropospheric column ozone (TrC-O₃) and trends for different column depths before the
COVID-19 pandemic (2005-2019) and including the pandemic (2005-2021).

429

3.4.2. Free tropospheric trends

Trends of ozone in the free troposphere presented here are based on previous work published in
~~ozonesonde data from~~ the literature. Despite the high stability of ozonesonde measurements
across the global networks over several decades (Stauffer et al., 2022), the spatial sparsity of
sounding stations and non-uniform sampling frequency among sites is a limitation in using these
data to produce trends. These shortcomings have constrained the ability to include data from
many stations in previously published analyses. For example, Chang et. al (2020) estimated that
at least 18 profiles per month are needed at a single station to calculate accurate long-term
trends, while uncertainty increases at lower sampling rates (Chang et al 2024). However, such
high sampling frequency is only achieved at three European stations (Hohenpeissenberg,
Germany; Payerne, Switzerland, and Uccle, Belgium), while the rest of the global stations work
at lower sampling rates. Nonetheless, high-quality ozonesonde observations continue to be the
gold standard against which satellite measurements are validated. Likewise, ozonesonde data
continue to provide spaceborne observations with climatological feedback. Thus, recent studies
have softened the sampling frequency criteria in order to take advantage of the valuable data set
collected by the global ozonesonde networks. For example, the latest trend studies establish the
~~Recently, it was proven that~~ minimum ~~temporal~~ frequency requirement~~s~~ to calculate trends to
~~from ozonesondes demand sampling to be executed at~~at least three ~~times~~ profiles per month
(Wang et al., 2022; Christiansen et al., 2022) with at least eight months of sampling in a year,
and at least 15 annual means for an analysis of about two decades (Wang et al., 2022). With
these criteria, recent ozonesonde trend analyses indicate that ozone concentration increased
globally by 1.8+/-1.3 ppbv/decade in the free troposphere within 800 to 400 hPa (Christiansen et
al., 2022). However, there is significant regional variability, as illustrated in Figure 9 where
ozone trends published by Wang et. ~~a~~Al. (2022) (1995-2017 data between 950-250 hPa) are

454 organized by regions and stations. For example, ozone in East Asia (Japan) has been increasing
455 at a rate of 3.5 to 5 ppbv/decade, particularly since 2010 (Christiansen et al., 2022). Over the
456 Southwestern Indian Ocean (La Réunion), trends are of similar magnitude (>4.5 ppbv/decade).
457 In tropical South America, over the Atlantic basin region (Paramaribo and Natal), sounding
458 measurements also show ozone increases by almost 3 ppbv/decade (Natal), but other regions in
459 South America continue to lack sufficient measurements to produce trends. At tropical stations in
460 Africa (Nairobi) and the Pacific Ocean (Hilo and American Samoa) trends are also positive,
461 although of lower magnitudes (0.83-1.7 ppbv/decade). In contrast, polar stations both at the
462 Arctic and Antarctica as well as the Southern Ocean show overall decreasing ozone
463 concentrations to non-significant trends. Exceptions are the Eureka station in Canada and Lauder
464 station in New Zealand, which both show slight ozone increases (less than 0.5 ppbv/decade). The
465 direction of regional trends by Wang et. al. (2022) is consistent with regional trends presented in
466 similar independent research (Christiansen et al., 2022). As atmospheric composition continues
467 to become modified under the current regime of climate change, building consistent and longer
468 time series of ozonesonde measurements at other regions will continue to be an important source
469 of firsthand information to assess tropospheric ozone changes and trends.

470
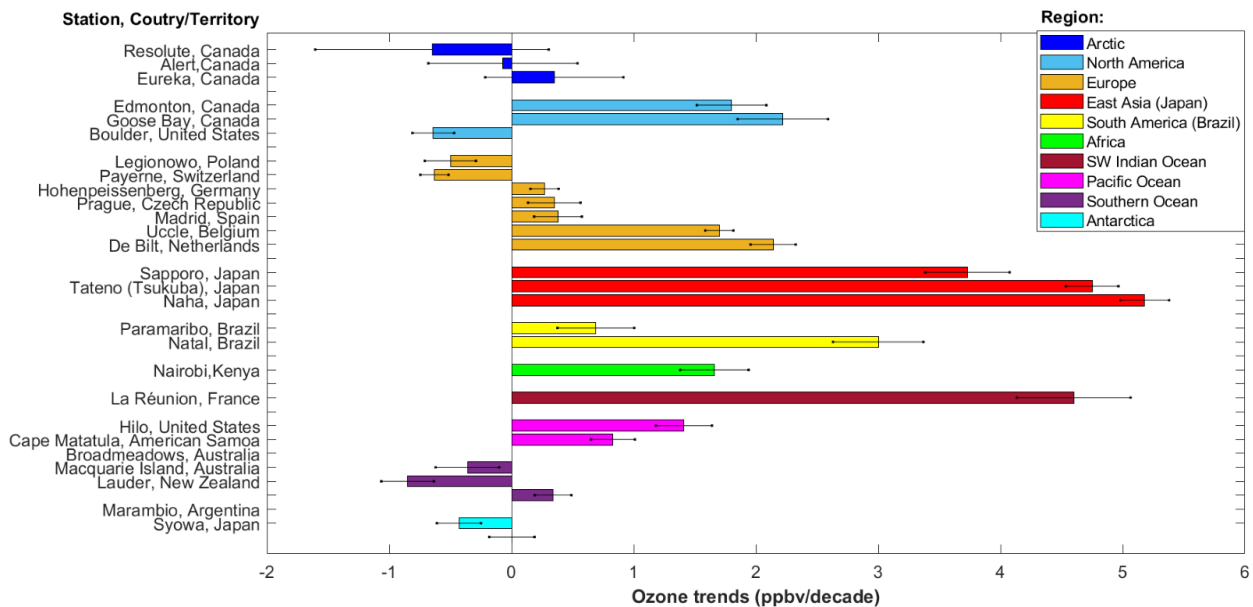
471
472 Figure 9: Ozone trends in the free troposphere from ozonesonde measurements calculated by
473 Wang et. Al. (2022) and organized by region and station. Data covers the 1995-2017 period
474 within 950 to 250 hPa. Error bars show 1-σ uncertainty. The coordinates of ozonesonde stations
475 are listed in Table S1.

476

3.4.3.   Regional Ozone Trends

478 As shown in Figure 10, the highest OMI/MLS regional trend is observed over East Asia
479 (2.16±1.27 DU/decade) while the lowest trend is calculated over Eastern USA (0.63±1.72)
480 followed by Western Europe (0.89±1.60) and Australia (1.05±1.44) DU/decade. We next
481 calculate the monthly trends from the GEOS-GMI simulation to investigate how the simulated
482 trends vary ~~by altitude~~through the tropospheric column.

483

484
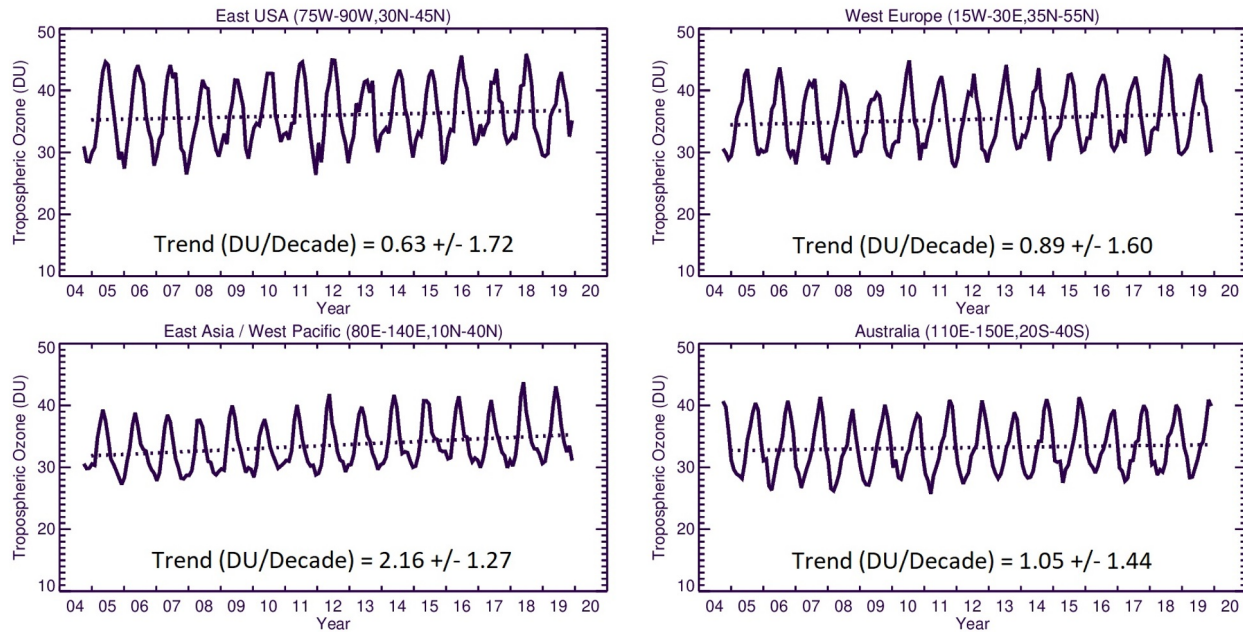
485

486   Figure 10: OMI/MLS observed regional mean trends of TrC-O_3.

487

488   The simulated trends in partial columns (lower, middle, and upper troposphere)~~of O₃, NO₂,~~
489   ~~formaldehyde, and CO from 2005 to 2019 for different pressure levels as well as the tropospheric~~
490   ~~columns~~, as well as the TrC-O_3, TrC-NO_2, TrC-HCHO, and TC-CO from 2005 to 2019, ~~-~~are
491   shown in Figure 11~~Figure 11~~. The simulated tropospheric columns of TrC-O_3 and TrC-HCHO
492   show a positive trend in most regions (Figure 11~~Figure 11~~), consistent with the results of Liu et
493   al (2022) using a different GEOSCCM simulation. Liu et al (2022) highlighted the importance
494   of formaldehyde trends for analyzing the simulated trends in tropospheric ozone. Considering
495   different latitude bands, the highest trends are simulated between 30º S and 60º N, consistent
496   with calculated trends based on satellite observations (see sec. 3.4). In contrast, the simulated
497   NO_2 and CO trends are mostly negative, although positive trends are simulated over East Asia.
498   The largest NO_2 negative trends are in the northern hemisphere between 30ºN and 60ºN. The
499   decrease in NO_2 trends is consistent with the successful measures to curb emissions of pollution
500   criteria in the US and Europe~~The decreasing NO₂ trends but increasing O₃ and HCHO trends in~~
501   ~~the northern hemisphere are due to the NO-sensitive conditions prevailing over Europe and the~~
502   ~~USA. ~~. The increased trends in TrC-O_3 but decreased trends in TrC-NO_2, and TC-CO might
503   indicate STE contribution (Trickl et al., 2020; Li et al., 2024) in addition to the local chemistry.

504

505

506
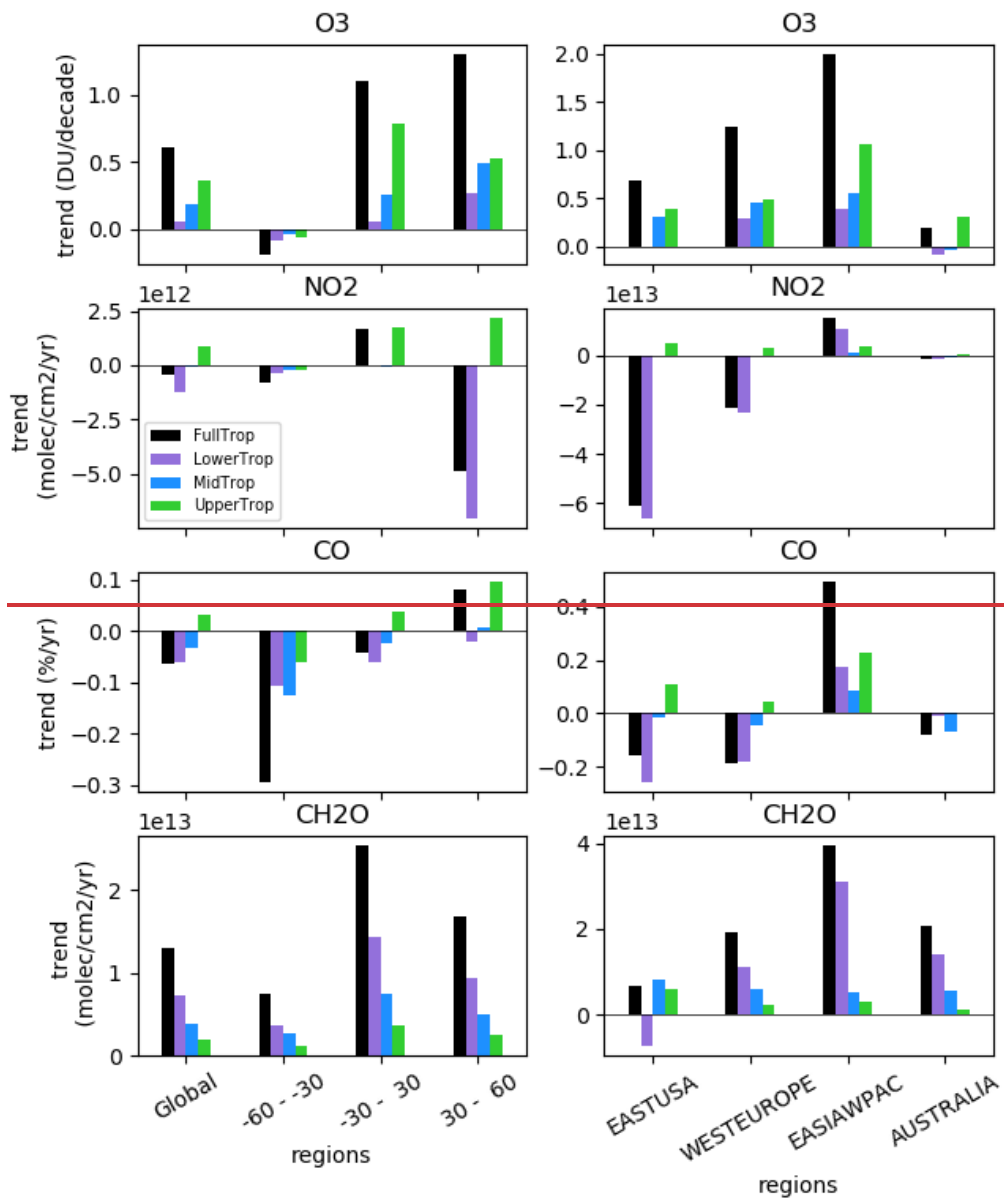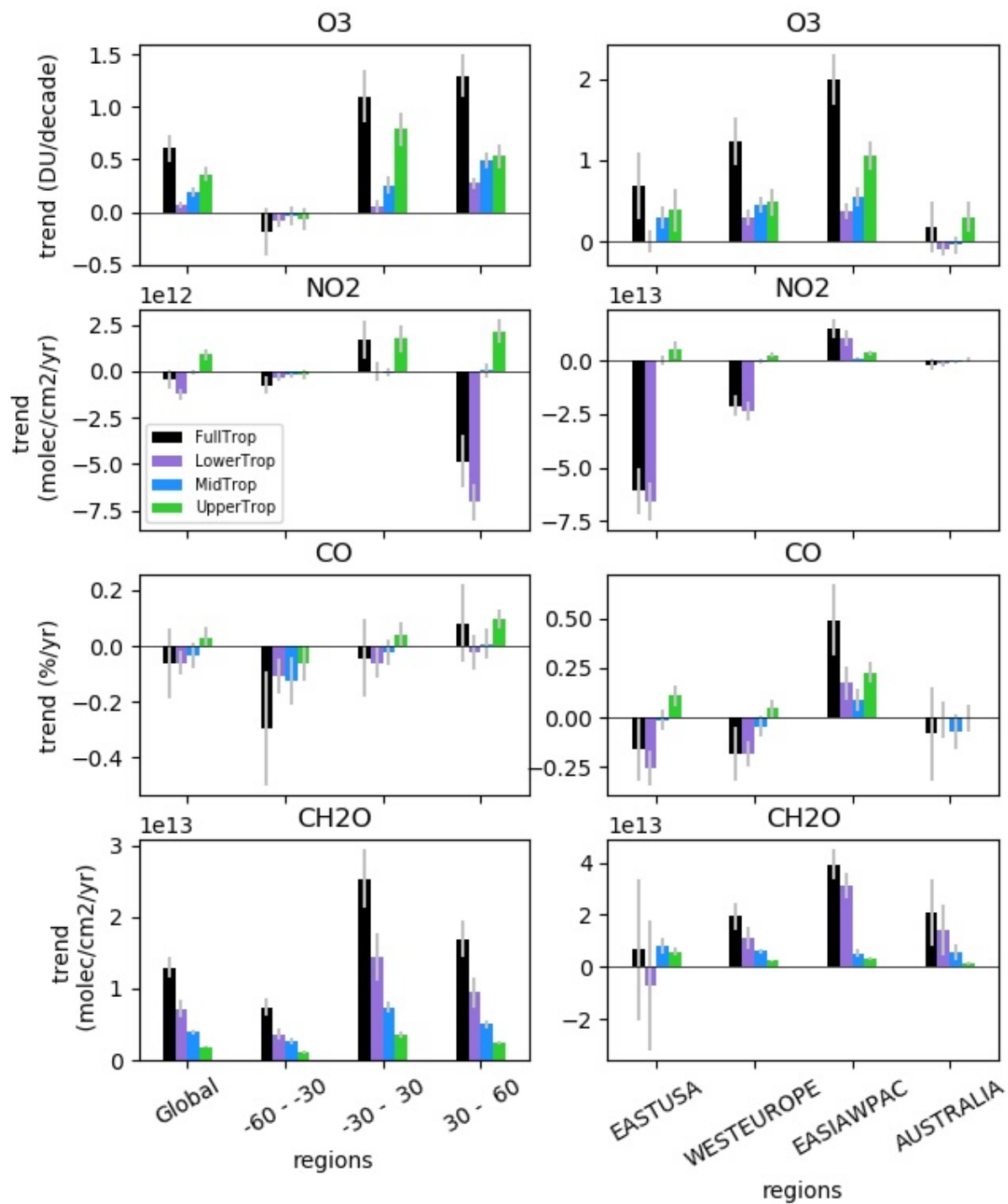
508 Figure 11: Global and regional trends in O_3, NO_2, CO, and HCHO calculated from the GEOS-
509 GMI simulation for the tropospheric column (black), lower troposphere (purple), middle
510 troposphere (blue), and upper troposphere (green) from 2005 to 2019. The lower, middle, and
511 upper troposphere are defined as in Figure 5.

512

513 The GEOS-GMI simulation provides an estimate of the relative contribution from different
514 portions of the tropospheric column to the column trends and shows that this contribution varies

515   by region and constituent. The middle and upper troposphere make the largest contributions to
516   the simulated TrC-O₃ trend globally, with large contributions from the upper troposphere driving
517   the simulated TrC-O₃ trend at 30°S-30°N ~~and counteracting the negative TrC-O₃ trend in the~~
518   ~~southern midlatitudes~~ (Figure 11~~Figure 11~~). ~~However, the middle and lower troposphere make~~
519   ~~larger contributions to the positive TrC-O₃ trends in the northern middle and high latitudes.~~ The
520   middle and upper troposphere contribute most of the simulated positive TrC-O₃ trend over the
521   eastern USA, while ~~the lower and middle troposphere are more important over western Europe,~~
522   ~~and~~ all three levels contribute over western Europe and East Asia. The upper troposphere makes
523   the primary contribution to the simulated trend over Australia. Simulated TrC-O₃ trends are also
524   quite comparable to those observed by OMI/MLS within the measurement model uncertainty
525   (see Figure 10 and Figure 7). Over Australia, the OMI/MLS trend of 1.05±1.44 DU/decade is
526   higher than the model trend of about 0.~~2~~ 18±0.308 DU/decade (see Figure 11~~Figure 11~~).
527   However, since OMI/MLS trend has a calculated uncertainty (2σ) of 1.44 DU/decade, both the
528   model and OMI/MLS for Australia are not statistically different.

529   While the upper troposphere is a major driver of the simulated TrC-O₃ trends, the lower
530   troposphere is the largest contributor to the simulated trends in the tropospheric NO₂, CO, and
531   HCHO ~~trends~~ globally and over many regions (Figure 11~~Figure 11~~). Exceptions include the
532   simulated NO₂ in the tropics (30°S-30°N), which is dominated by the upper troposphere, the
533   simulated HCHO column over the ~~e~~Eastern USA, which is driven by the middle and upper
534   troposphere; an important role for upper tropospheric CO over East Asia; and the CO trend over
535   Australia driven by the middle tropospheric contribution. Figure 11~~Figure 11~~ also shows that in
536   some regions, such as the eastern USA for all 3 precursors, the upper and lower tropospheric
537   trends counteract each other, reducing the magnitude of the column trend. In the following
538   sections, we investigate trends and variability in O₃ precursors, NO₂, CO, and HCHO.

539   ### 3.4.4.   NO₂ Trends

540   The TrC-NO₂ trends over 2005-2019 are shown in Figure 12 with a regional summary in Figure
541   13. On a global scale, there is a strong spatial variability of the TrC-NO₂ trends. About a third of
542   the oceans show significantly increasing TrC-NO₂ (at 95% confidence level), especially at mid-
543   latitude, with trends up to +0.01 Pmolec/cm²/yr, while only a few cells in the equatorial Pacific
544   show a significant decrease.
545

546
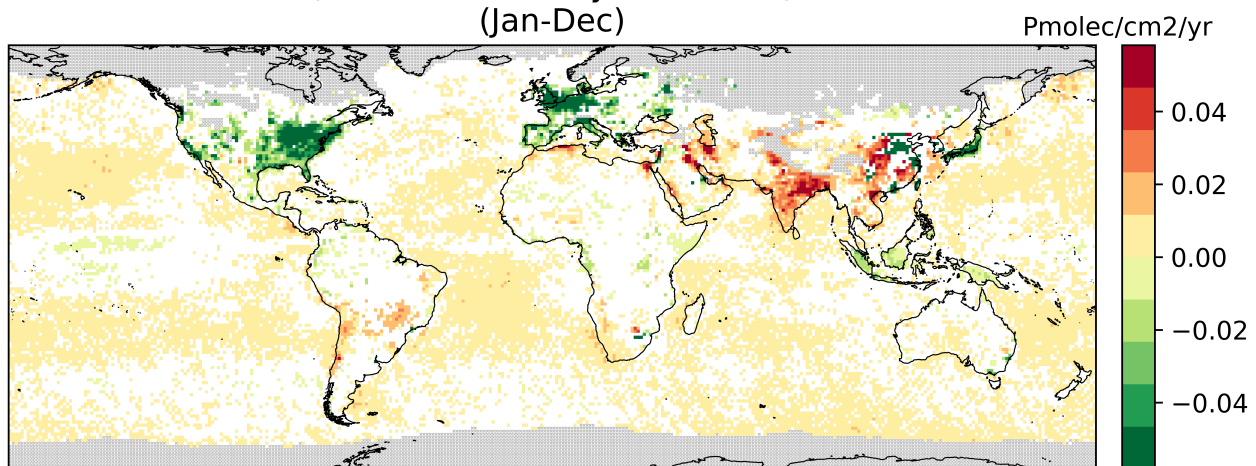
Figure 12: Global trends of OMI NO$_2$ tropospheric column (TrC-NO$_2$) over 2005-2019 (see text for details on the calculation of the trends). Grey areas correspond to areas without enough data, white areas correspond to regions where the trends remain statistically insignificant at a 95% confidence level.

Regional trends are shown in Figure 13. For significant trends in a given region, the numbers correspond to the percentiles 5/50/95 of trends among the different cells of the region where trends are significant. Each region is tagged with a circle whose size is proportional to the p50 of the significant trends (red for positive and green for negative), which allows us to quickly see regions where the trend is strong. For instance, for Eastern Asia (this region includes 1442 1°x1° grid cells) about 15% of the grid cells (about 216 grid cells) in this region show a significant decrease in TrC-NO$_2$. Over these specific 216 cells with a significant decrease of TrC-NO$_2$, the 5th and 95th percentile of the trend is -0.34 and -0.01, respectively, Pmolec/cm^2/yr. About 28% of the grid cells in this region show a significant increase of TrC-NO$_2$ (which means about 403 grid cells). Over these specific 403 cells with a significant increase of TrC-NO$_2$, the 5th (resp 95th) percentile of the trend is +0.01 (resp 0.05) Pmolec/cm^2/yr. Therefore, the Eastern Asia region shows sub-regions with significantly decreasing TrC-NO$_2$, others with significantly increasing TrC-NO$_2$, and the rest with non-significant (positive and negative) trends. This figure allows us to quickly understand the distribution of the trends within a~~this~~ given region while the overall regional trend is given by the 50th percentile and the circles tagging each region. It's a regional summary of what is shown in the trend global map. In Eastern Asia, the area where trends are significantly positive is more extended than for the significant decrease (28% versus 15%), but the trend values tend to be smaller (at least when comparing the 50th percentiles, -0.05 versus +0.01 Pmolec/cm^2/yr). The map of regions is included in the supplement. Canada is included in northern America but as shown in the trend map, most of Canada does not have OMI data

Over continental areas, significant positive and negative trends are found in about 15-20% of the grid cells each (Figure 12). Regions with predominantly decreasing TrC-NO$_2$ include western and southern Europe (where about 50-60% of cells with a significant decrease), northern America (40% of cells with a significant decrease, mostly located in the eastern United States), Japan, and Indonesia. In absolute terms, these negative trends reach values of about -0.03 Pmolec/cm^2/yr. Specific eastern regions of China also show similar significant TrC-NO$_2$ decreases but overall, a larger part of the country faces increasing trends up to +0.03 Pmolec/cm^2/yr. Similar p~~P~~ositive trends ~~of similar magnitude~~ are observed over most of India, as well as in specific parts of south-eastern Asia (mainly Vietnam) and the Middle East (mainly Iran and Iraq). Conversely, TrC-NO$_2$ trends in Africa and South America remain mainly insignificant, except in a few specific regions with significant increases (e.g. South Africa, ~~Chile,~~ Morocco, Chile, and parts of Brazil).

~~————~~The trends in NO$_2$ have varying effects on the tropospheric ozone column, which is related to the different local chemistry in each region. The concomitant ~~increase or~~ decrease in TrC-O$_3$ and TrC-NO$_2$ trends over some parts of~~the~~ the eastern US, and western~~central~~ Europe is ~~due to~~consistent with ~~the dominant NO-sensitive condition due to~~ the strict NO$_x$ control measures that were applied over the last two decades. STE can also contribute to increased TrC-O$_3$ trends, especially in the mid-latitudes. ~~The~~ A decreasing trend of TrC-NO$_2$ but an increasing trend of TrC-O$_3$ is present in some ~~in~~ other~~some~~ regions such as ~~in~~ the central US, which might be due to local chemistry and STE.~~, e.g., over Chicago is due to the high NO$_x$ conditions in these regions (e.g., Elshorbany et al., 2021 and references therein). The increasing TrC-O$_3$ trends as~~

595
596

Overview of OMI TrC-NO2 annual trends
(Pmolec/cm2/yr; based on monthly anomalies)

Region	Significant decrease value	Significant increase value
All (+0.00)	-0.01 [-0.12;-0.00]	+0.01 [+0.00;+0.01]
All oceans (+0.00)	-0.00 [-0.03;-0.00]	+0.01 [+0.00;+0.01]
All continents (+0.00)	-0.02 [-0.13;-0.00]	+0.01 [+0.00;+0.04]
America (-0.00)	-0.02 [-0.11;-0.00]	+0.01 [+0.00;+0.02]
Northern America (-0.01)	-0.03 [-0.13;-0.01]	+0.01 [+0.00;+0.01]
Central America (-0.00)	-0.01 [-0.04;-0.00]	+0.01 [+0.00;+0.01]
South America (+0.00)	-0.01 [-0.02;-0.00]	+0.01 [+0.00;+0.02]
Caribbean (-0.00)	-0.01 [-0.01;-0.00]	+0.00 [+0.00;+0.01]
Europe (-0.01)	-0.03 [-0.15;-0.01]	+0.01 [+0.00;+0.01]
Northern Europe (-0.00)	-0.04 [-0.21;-0.01]	+0.01 [+0.00;+0.02]
Southern Europe (-0.01)	-0.02 [-0.10;-0.01]	+0.01 [+0.00;+0.01]
Western Europe (-0.03)	-0.05 [-0.18;-0.01]	
Eastern Europe (-0.00)	-0.02 [-0.07;-0.01]	+0.01 [+0.00;+0.01]
Africa (+0.00)	-0.01 [-0.02;-0.00]	+0.01 [+0.00;+0.02]
Northern Africa (+0.00)	-0.00 [-0.01;-0.00]	+0.01 [+0.00;+0.04]
Middle Africa (-0.00)	-0.01 [-0.02;-0.00]	+0.01 [+0.00;+0.01]
Southern Africa (+0.01)	-0.03 [-0.18;-0.01]	+0.01 [+0.00;+0.01]
Western Africa (-0.00)	-0.00 [-0.01;-0.00]	+0.01 [+0.00;+0.01]
Eastern Africa (-0.00)	-0.01 [-0.02;-0.00]	+0.01 [+0.00;+0.01]
Asia (+0.00)	-0.01 [-0.20;-0.00]	+0.01 [+0.00;+0.05]
Central Asia (+0.00)	-0.00 [-0.01;-0.00]	+0.01 [+0.00;+0.03]
Southern Asia (+0.01)	-0.01 [-0.01;-0.01]	+0.02 [+0.01;+0.07]
South-Eastern Asia (-0.00)	-0.01 [-0.02;-0.00]	+0.01 [+0.00;+0.03]
Western Asia (+0.00)	-0.01 [-0.06;-0.00]	+0.01 [+0.00;+0.07]
Eastern Asia (+0.00)	-0.05 [-0.34;-0.01]	+0.02 [+0.01;+0.05]
Oceania (+0.00)	-0.01 [-0.03;-0.00]	+0.01 [+0.00;+0.01]
Australia and New Zealand (+0.00)	-0.01 [-0.03;-0.00]	+0.01 [+0.00;+0.01]
Melanesia (+0.00)	-0.01 [-0.01;-0.00]	+0.00 [+0.00;+0.01]
Micronesia (+0.00)	-0.00 [-0.00;-0.00]	+0.00 [+0.00;+0.00]
Polynesia (+0.00)		+0.00 [+0.00;+0.01]

Percentage of 1deg x 1deg grid cells

- ■ Significant decrease
- ■ Non-significant decrease
- ■ Non-significant increase
- ■ Significant increase

597

598 Figure 13: Summary of the statistically significant and insignificant regional trends of OMI NO₂
599 tropospheric column (TrC-NO₂) trends over 2005-2019, at a 95% confidence level (see text for
600 details on the calculation of the trends). For each region, the trend on the bars is in the format:
601 p50 [p5; p95], which represents the 50th[5th, and 95th] percentiles of the trends.

602

603 Figure 14~~Figure 14~~ shows the time series of regional mean tropospheric NO₂ concentrations from
604 three satellite instruments, OMI for 2005-2020, GOME-2 for 2007-2018, and SCIAMACHY for
605 2005-2012. All the instruments exhibit common large seasonal and year-to-year variations over
606 both industrial regions and biomass-burning areas. Slight systematic differences among the

607   instruments can mainly be attributed to the different overpass times. The satellite observations
608   show positive trends over China by 2010, followed by a continued decrease. Over the USA and
609   Europe, all the retrievals show a downward trend over the analysis period. Over the US, the
610   observed TrC-NO$_2$ levels decreased rapidly during 2005–2009 and subsequently show weaker
611   reductions, as discussed by Jiang et al. (2018). A similar slowdown trend is found in Europe. Over
612   India, the OMI observations show positive trends over the 14 years (+1.6 % yr^{-1}). The seasonal
613   and year-to-year variations over Southeast Asia and northern and central Africa are associated with
614   changes in biomass-burning activity (Ghude et al., 2009).
615
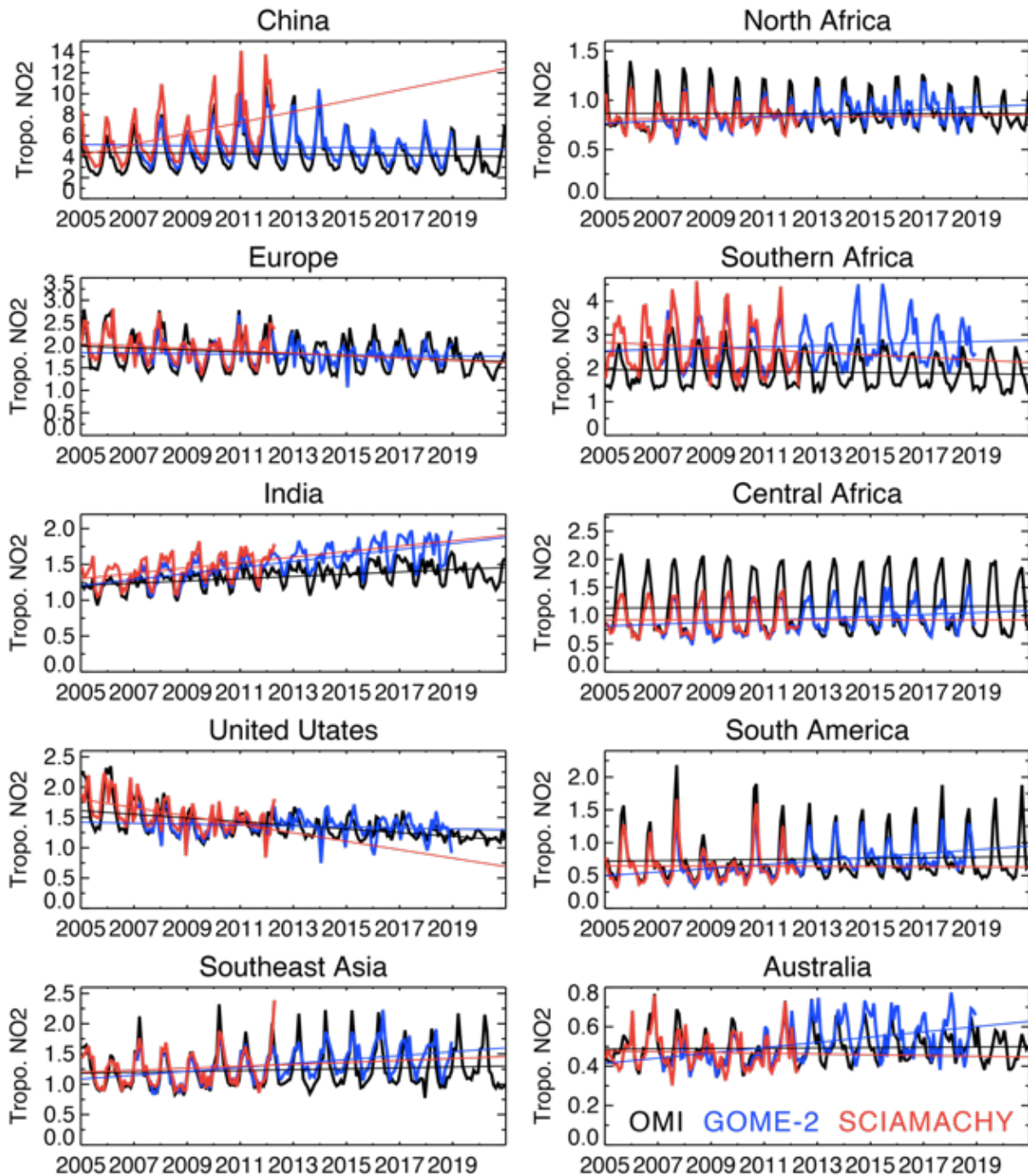
616

617 Figure 14: Time series of regional monthly mean tropospheric NO$_2$ columns (in 10^{15} molecules
618 cm^{-2}) averaged over China (110–123° E, 30–40° N), Europe (10° W–30° E, 35–60° N), the US
619 (70–125° W, 28–50° N), India (68–89° E, 8–33° N), South America (50–70° W, 20° S–Equator),
620 northern Africa (20° W–40° E, Equator–20° N), central Africa (10–40° E, Equator–20° S),
621 southern Africa (25–34° E, 22–31° S), southeastern Asia (96–105° E, 10–20° N), and Australia
622 (113–155° E, 11–44° S) obtained from OMI (black), GOME-2 (blue), and SCIAMACHY (red).

3.4.5.   ~~Carbon Monoxide~~CO Trends

CO trends are calculated based on MOPITT v9 products ~~(adapted from Buchholz et al. (2021),~~
~~see sec. 2.2.1)~~. Observed CO trends below show a slowing in the trend compared to ~~the~~a
previous analysis (Buchholz et al. (2021). ~~In the northern hemisphere, CO trends are largely~~
~~negative over the US and Europe, which is consistent with the implemented policies to reduce air~~
~~pollution since 2005.~~ In the northern hemisphere, CO trends are largely negative over the US and
Europe, which is consistent with improvements in combustion efficiency and policies
implemented to reduce air pollution since 2004. Except for small sporadic positive trends, no
significant trends can be calculated over Central Asia (India and China), while there is a strong
negative trend in East China due to the recent strong focus on air quality improvement, and no
significant trend in the SH ~~(relative to slope error)~~.
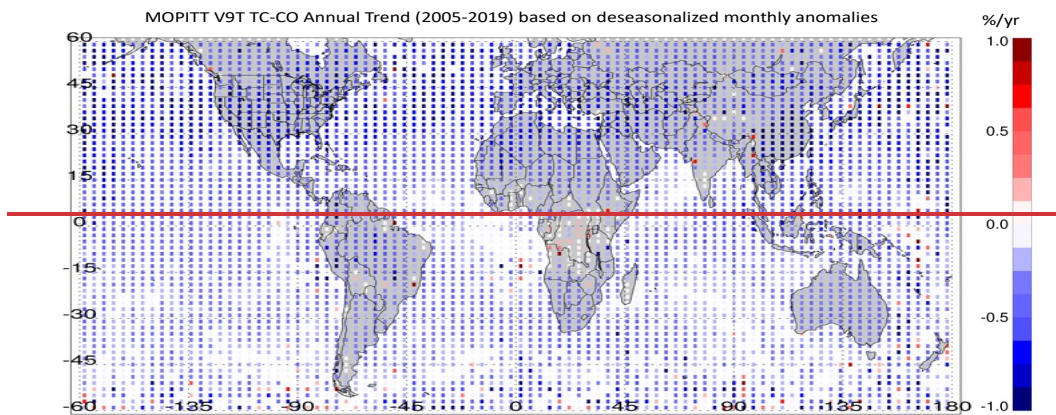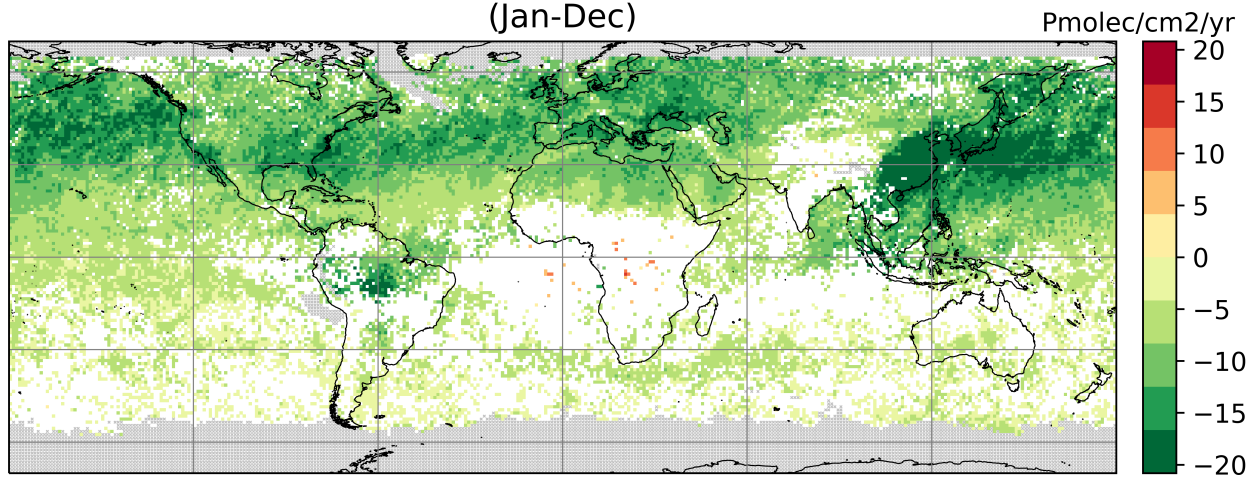
Figure 15: Trends in TC-CO from MOPITT V9JT data, 2005-2019 (see text for details on the calculation of the trends). Grey areas correspond to areas without enough data, white areas correspond to regions where the trends remain statistically insignificant at a 95% confidence level.

Trends are computed from deseasonalized monthly anomalies.

Calculated global CO trends are driven mainly by the decreasing trends in the NH. Shown below are the trends in the MOPITT column average volume mixing ratio (VMR) anomalies from 2005 to 2019 (Figure 16) using QR as well as Weighted least squares (WLS)) as Buchholz et al. (2021). The region boundaries are the same as used in Fig. 10 and 11. Results show a significant decreasing trend in the NH (-0.35 ±0.1% annually), a smaller decreasing trend in the Mid-latitudes (-0.26 ±0.1% annually) and no significant trend in the SH (-0.14 ±0.1% annually). The three anthropogenic regions investigated in the NH all show strong decreases in CO. The larger negative trend over Australia (-0.2 ±0.1% annually) than the average SH, suggests sources from the other two land regions (Southern Africa and South America) may be counteracting negative trends in CO for the SH.

We also compare CO trends with Community Earth System Model (CESM) simulations (Supplement Fig S1). While the magnitude of modeled CO tends to be underestimated relative to observations, the anomalies between model and measurements are comparable, indicating the model reproduces interannual variability well. The negative trends in the NH are also reproduced by CESM, although to a smaller degree than observations, suggesting that the trends in sources or loss processes (such as OH oxidation) are underestimated in the model. These processes will impact the feedback into modeled ozone and the resulting interpretation of driving factors for ozone abundance and variability. Interestingly, CESM correctly represents a negative trend in CO for the NH and East Asia while GEOS GMI has a positive CO trend in those regions (Fig. 11), likely due to the well-known misrepresentation of East Asia air quality improvements in models (Yin et al, 2015; Strode et al., 2016; Zheng et al, 2019). In the SH, CESM does not predict significant trends.

A regional summary of the trends in the global map is shown in Figure 16. CO trends are predominantly negative everywhere except for some sporadic positive trends over middle Africa. Decreasing TC-CO trends are highest in Europe, followed by Asia and America with about 86%, 75%, and 69% of their cells being negative, respectively. The 50 percentiles of the trends in these cells are -12.01, -10.21, and -10.16 Pmolec/cm^2/yr, respectively. Africa shows the lowest decreasing trends as the negative trends in North Africa are being offset by small increasing trends in middle Africa. Overall, about 41% of the cells in Africa show decreasing trends, and 50% of the trends in these cells account for -8.71 Pmolec/cm^2/yr. Thus, even though the NH accounts for most of CO emissions, decreasing trends of TC-CO are evident in these regions.
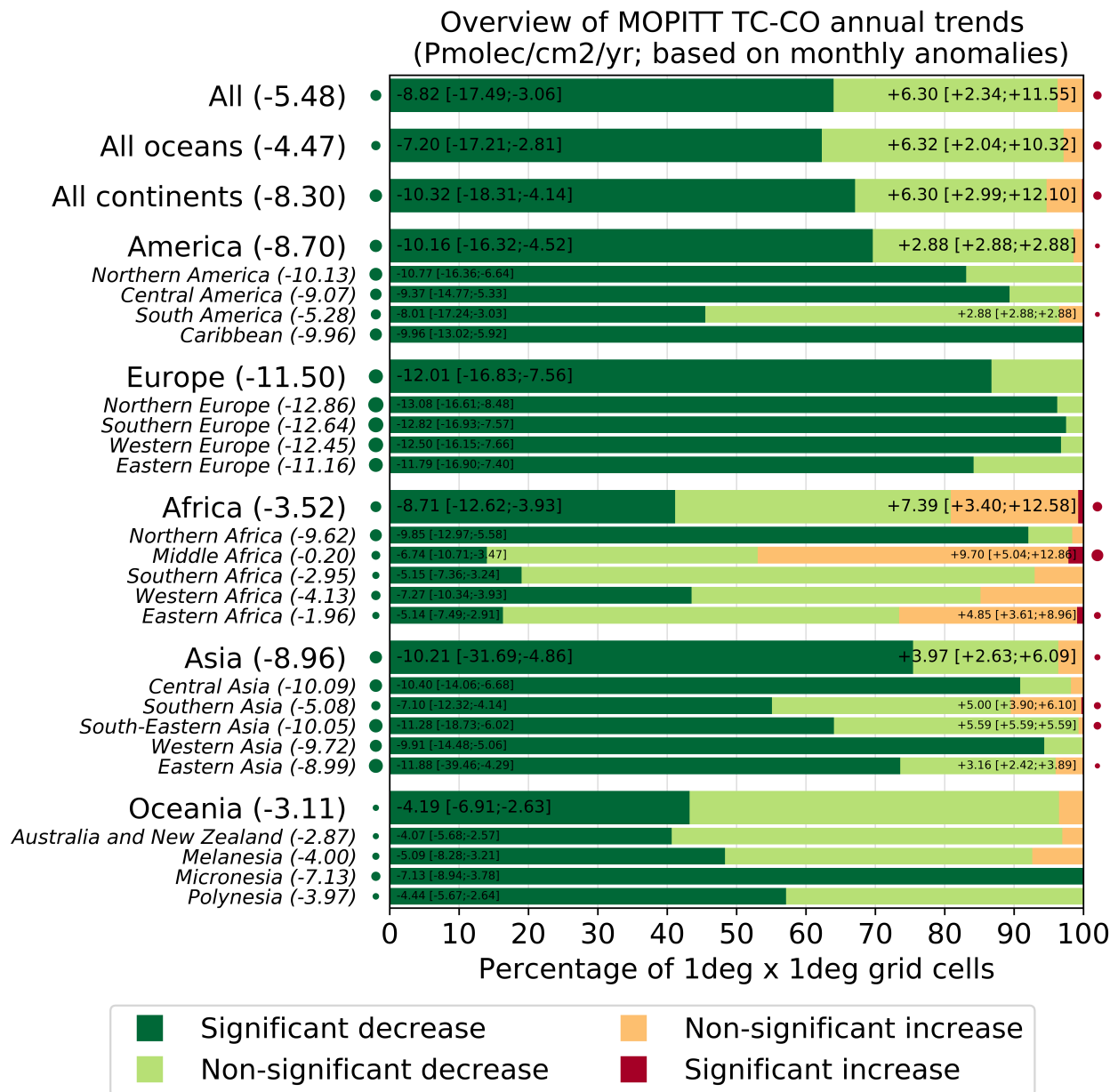
Figure 16: Summary of the statistically significant and insignificant regional trends of MOPITT TC-CO trends over 2005-2019, at a 95% confidence level (see text for details on the calculation of the trends). For each region, the trends reported on the left (resp. right) represent the [5]th, 50th and 9[5]th percentiles of the trends calculated over the different grid cells showing a significant TC-CO increase or decrease.

Shown below are also the trends in the MOPITT column average volume mixing ratio (VMR) anomalies from 2005 to 2019 (Figure 17) using QR as well as Weighted least squares (WLS)) as Buchholz et al. (2021). The region boundaries are the same as used in Fig. 10 and 11. Results show a significant decreasing trend in the NH (-0.35 ±0.1% annually), a smaller decreasing trend in the Mid-latitudes (-0.26 ±0.1% annually) and no significant trend in the SH (-0.14 ±0.1% annually). The three anthropogenic regions investigated in the NH all show strong decreases in CO. The larger negative trend over Australia (-0.2 ±0.1% annually) than the average SH,

  suggests sources from the other two land regions (Southern Africa and South America) may be
  counteracting negative trends in CO for the SH.

691

692

693

694

Figure 17: MOPITT monthly average CO anomalies in column average volume mixing ratio (VMR, ppb), 2005-2021 (black). Updated dataset based on Buchholz et al. (2021). Data is Level 3, monthly average daytime observations, using version 9 joint NIR/TIR retrievals (V9J). Regions are defined in Figure 10 and Figure 11Figure 11. Trends are calculated on anomalies 2005-2019. The weighted Least Squares trend (red) is weighted by the monthly regional standard deviation. The quantile regression trend is also shown (pink). Grey dashed lines indicate a zero trend.

We also compare CO trends with Community Earth System Model (CESM) simulations (Supplement Fig S1). While the magnitude of modeled CO tends to be underestimated relative to observations, the anomalies between the model and measurements are comparable, indicating the model reproduces interannual variability well. The negative trends in the NH are also reproduced by CESM, although to a smaller degree than observations, suggesting that the trends in sources or loss processes (such as OH oxidation) are underestimated in the model. These processes will impact the feedback into modeled ozone and the resulting interpretation of driving factors for

710 ozone abundance and variability. Interestingly, CESM correctly represents a negative trend in
711 CO for the NH and East Asia while GEOS-GMI has a positive CO trend in those regions (Fig.
712 11), likely due to the well-known misrepresentation of East Asia air quality improvements in
713 emission inventories (Yin et al, 2015; Strode et al., 2016; Zheng et al, 2019). In the SH, CESM
714 does not predict significant trends.

715

3.4.6. HCHO Trends

717 HCHO, mainly a photochemical product results from hydrocarbon oxidation. HCHO is itself a
718 source of OH and ozone through its photolysis producing HO_2, which can be recycled back to
719 OH if sufficient NO levels are present.

720 R 3.4-1 $HCHO$ $+$ $h\nu \, (\lambda < 325 \text{ nm})$ $\rightarrow$ H $+$ HCO

721 R 3.4-2 H $+$ O_2 $+$ M $\rightarrow$ HO_2 $+$ M

722 R 3.4-3 HCO $+$ O_2 $\rightarrow$ HO_2 $+$ CO

723 R 3.4-4 HO_2 $+$ NO $\rightarrow$ OH $+$ NO_2
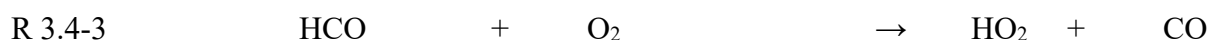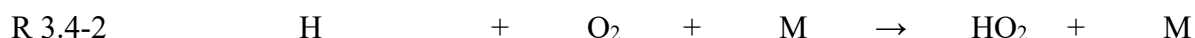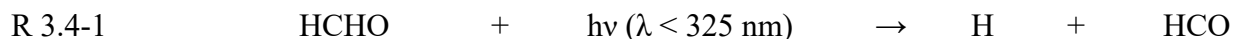
724 Unlike higher aldehydes, the OH reaction with HCHO leads also to the formation of a formyl
725 radical (HCO), which ultimately forms HO_2 (R 3.4-3R 3.4-3).

726 R 3.4-5 $HCHO$ $+$ OH $\rightarrow$ H_2O $+$ HCO

727 Due to its solubility, the variability of HCHO also depends on the presence of clouds, and wet
728 deposition ultimately represents another important sink for HCHO (Lelieved and Crutzen, 1991).
729 Overall, HCHO plays a key role in the O_3 budget, both in polluted and remote regions.

730 Trends of the OMI HCHO tropospheric columns (hereafter referred to as TrC-HCHO) are
731 computed as described for OMI TrC-NO$_2$. TrC-HCHO trends over 2005-2019 are shown in
732 Figure 1817Figure 17 with a regional summary in Figure 1918Figure 18. The first global feature
733 to highlight on the global trends map is the presence of stripes along the OMI orbits. The number
734 of rows affected by the OMI row anomaly has increased over the years (Boersma et al., 2018).
735 The affected rows are filtered out in the HCHO data, but the change in the sampling and the
736 related increase in the noise impact the trend analysis. Along orbit stripes in the trend analysis
737 should be ignored but zonal trends are still valid (Figure 1817Figure 17).

738

Annual trend of OMI TrC-HCHO
(based on monthly anomalies)
(Jan-Dec)

739
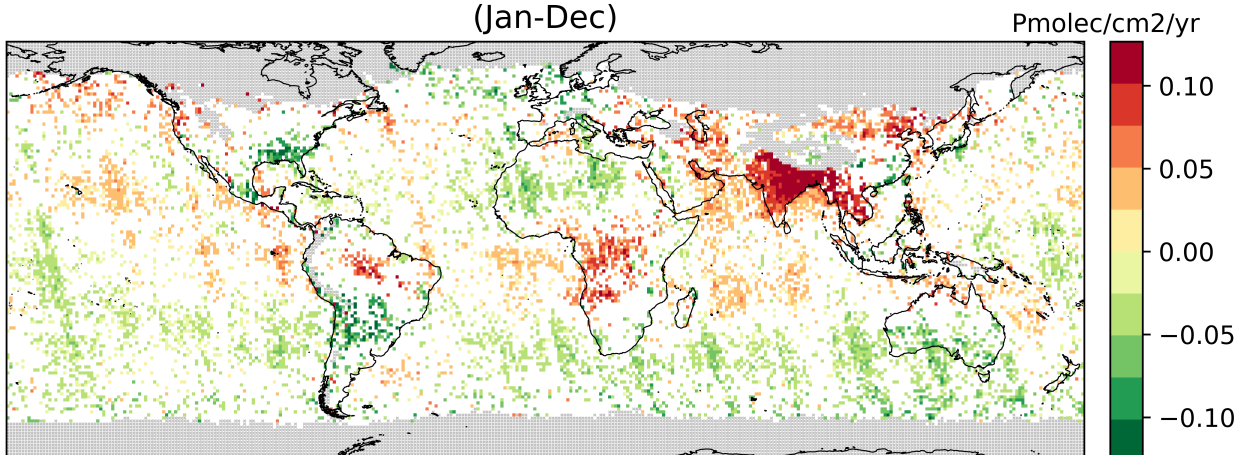
740 Figure 18̶1̶7̶: Global trends of OMI HCHO tropospheric column (TrC-HCHO) over 2005-2019
741 (see text for details on the calculation of the trends). Grey areas correspond to areas without
742 enough data, white areas correspond to regions where the trends remain statistically insignificant
743 at a 95% confidence level.

744 Despite the fact that TrC-HCHO trends remain insignificant over a large part of the globe,
745 specific regions do highlight clear trends. The region with clearest changes is unambiguously
746 southern Asia where about 65% of the cells show increasing trends with a median of +0.09
747 Pmolec/cm^2/yr. The other regions with a large portion (25-30% of the cells) of increasing trends
748 include the rest of Asia and ~~Middle~~ central Africa, with median TrC-HCHO trends ranging
749 between +0.05 and +0.08 Pmolec/cm^2/yr, as well as some parts of central Brazil (Amazonians).
750 Conversely, some significant decreases of TrC-HCHO are observed in the south-eastern US, the
751 southern half of Southern America, North and western Africa, and southern Australia, although
752 part of them overlap with the aforementioned stripes and might thus not be real.

753
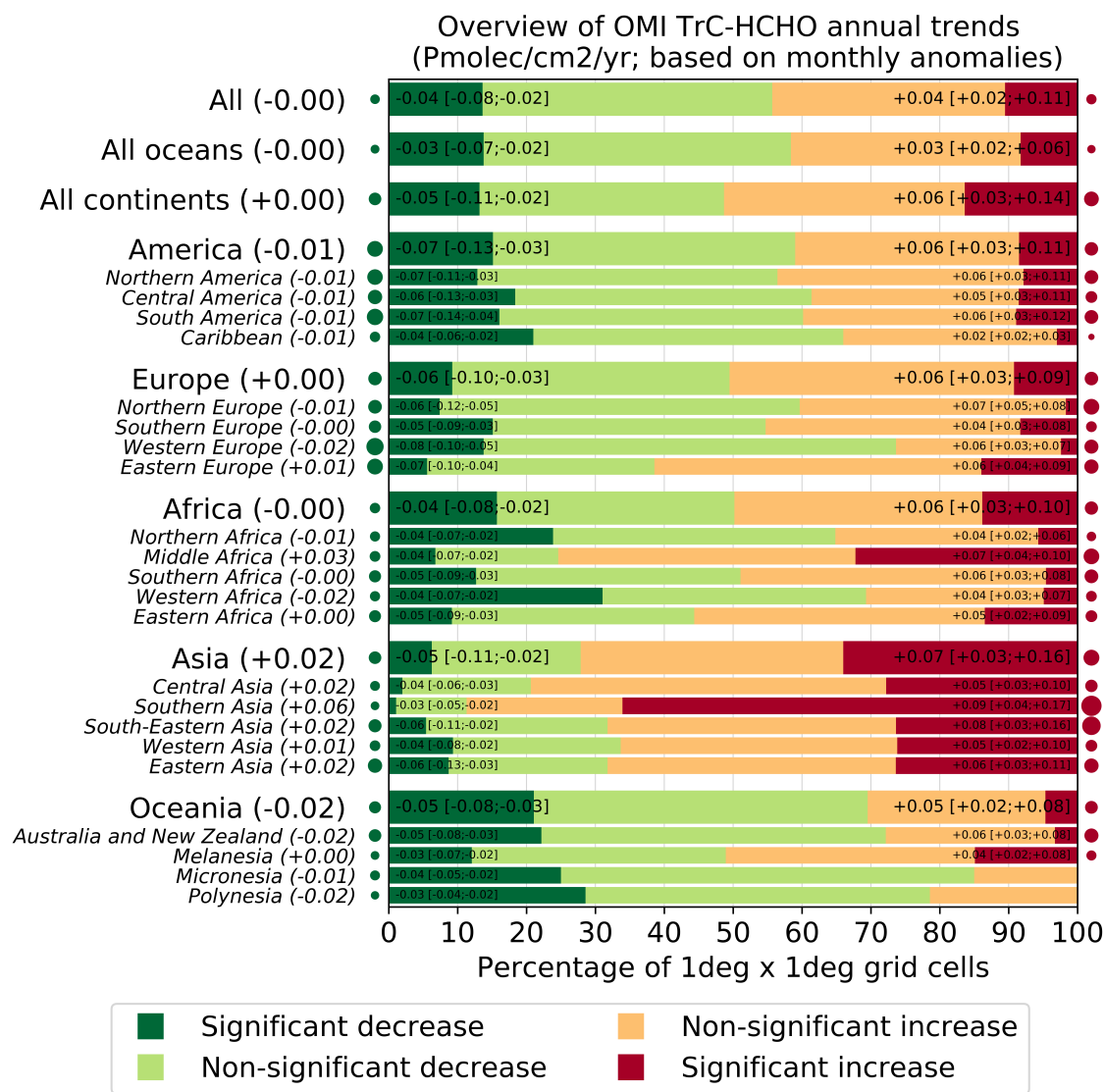
Figure 1918: Summary of the statistically significant and insignificant regional trends of OMI
HCHO tropospheric column (TrC-HCHO) trends over 2005-2019, at a 95% confidence level
(see text for details on the calculation of the trends). For each region, the trends reported on the
left (resp. right) represent the 5th, 50th and 95th percentiles of the trends calculated over the
different grid cells showing a significant TrC-HCHO increase or decrease.

HCHO trends are inconsistent with that of O$_3$ (sec. 3.4.1) in some regions which might be due to
several factors, such as their different sensitivity to NO$_x$ and hydrocarbons (Luecken et al., 2018)
but also possible STE contribution to tropospheric ozone levels, especially in midlatitudes
(Willimas et al., 2019; Li et al., 2024). For example, while TrC-O$_3$ is increasing in the
southeastern US, TrC-NO$_2$, TC-CO, and TrC-HCHO are decreasing, which, in addition to the
local chemistry, might indicate a STE signal. O$_3$ and HCHO trends are consistent with NO$_2$ over
Eastern US and Europe. However, TrC-NO$_2$ trends are decreasing over the northern coast of
Australia while thatose of TrC-O$_3$ and TrC-HCHO are increasing. While the increase of
HCHO/NO$_2$ might indicate a trend toward NO-limited conditions (see below), the increase of
TrC-O$_3$ trends in this region might also indicate increasing trends of STE contribution (Li et al.,

771 2024). Similarly, while NO₂ trends are slightly increasing over central and southern Australia,
772 trends of TrC-O₃ and TrC-HCHO ~~are~~were decreasing, which indicates a trend toward VOC-
773 limited conditions (see below). ~~The decreasing trends of HCHO and O₃ as NO₂ increases is~~
774 ~~evidence of the VOC-limited conditions in these regions. Under these conditions, increased NO₂~~
775 ~~levels lead to a reduction of OH via OH+NO₂=HNO₃, which decreases the oxidation capacity~~
776 ~~and thus lowers the photochemical formation of HCHO and O₃.~~

777

778 **3.4.7.   HCHO/NO₂**

779 ~~Since the pioneer study of Martin et al. (2004), t~~The ratio of TrC-HCHO/TrC-NO₂ observed from
780 space (e.g., Martin et al., 2004) has been used in a number of studies to give insights on the O₃
781 chemical regime, higher (resp. lower) TrC-HCHO/TrC-NO₂ ratios ~~coming with more~~indicate
782 NO$_x$-limited (resp. RO$_x$-limited) regimes. Although imperfect (e.g. Souri et al., 2023), this
783 indicator yet provides some qualitative information on the evolution of the O₃ regime over the last
784 years (Nussbaumer et al., 2023). We note that this analysis does not consider variations in the
785 ratios and their trends with respect to season or altitude. The mean TrC-HCHO/TrC-NO₂ over
786 2005-2019 are shown in Figure 2019~~Figure 19~~, and the trend results in Figure 2120~~Figure 20~~ with
787 a regional summary in Figure 2221~~Figure 21~~. The highest ratios are observed in the tropical regions
788 due to strong TrC-HCHO ~~due to high~~from biogenic sources and fire NMVOC emissions in tropical
789 South America and Africa combined with relatively low TrC-NO₂. Conversely, lower TrC-
790 HCHO/TrC-NO₂ ratios are observed across western Europe and north-eastern Asia, and to a lesser
791 extent, the north-eastern US.

792
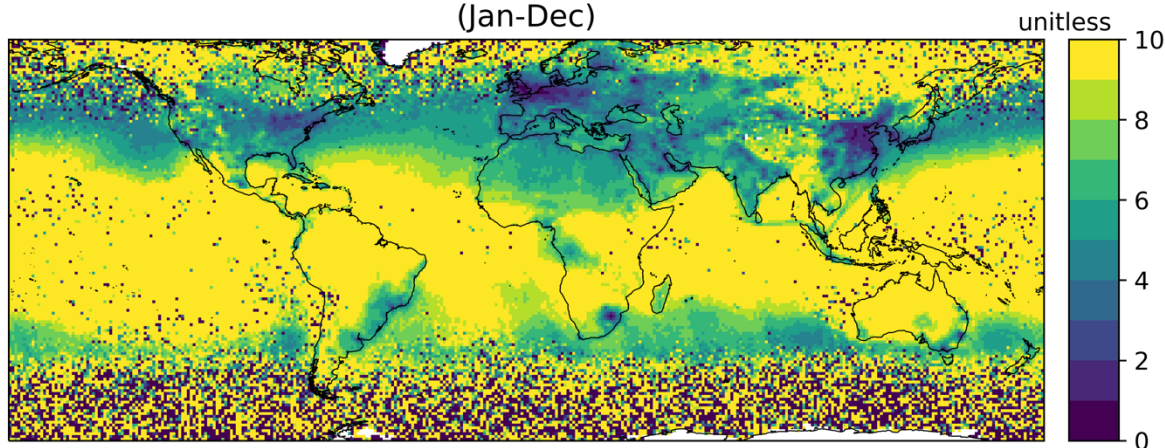
793
794 Figure 20~~19~~: Global mean OMI HCHO/NO₂ tropospheric column ratio over 2005-2019.

795
796 At a global scale, the significant changes in TrC-HCHO/TrC-NO₂ ~~ratios~~trends (Figure 2120-
797 Figure 2221) mostly go in the direction of a reduction, with about 25% of the grid cells showing a
798 median trend of -0.52 yr⁻¹. (while only 5% of the cells show a significant increase of +0.03 yr⁻¹) as
799 shown in Figure 2221. This suggests that these areas are evolving toward ~~more NOx~~VOC-sensitive
800 conditions (which does not necessarily imply that they are already in this regime). This situation
801 is observed over a large part of Oceania (especially Polynesia) and specific parts of Africa, Asia,
802 and South America. The opposite significant trends, toward more ~~RO$_x$~~NO-sensitive conditions,
803 are mainly observed over Europe and northern America, as well as south~~-eastern~~ Asia. We note

804 that the mean TrC-HCHO/TrC-NO$_2$ indicates the mean status of the chemical regime over this
805 period of time (2005-2019). However, the trends of the TrC-HCHO/TrC-NO$_2$ ratio show the
806 changing sensitivity of the chemical regime over this period of time. For example, while the ratio
807 in Eastern US indicates VOC-sensitive conditions, the trends of TrC-HCHO/TrC-NO$_2$ indicate a
808 direction toward NO-sensitive conditions.

809

810

Annual trend of OMI TrC-HCHO/NO2
(based on monthly anomalies)
(Jan-Dec)
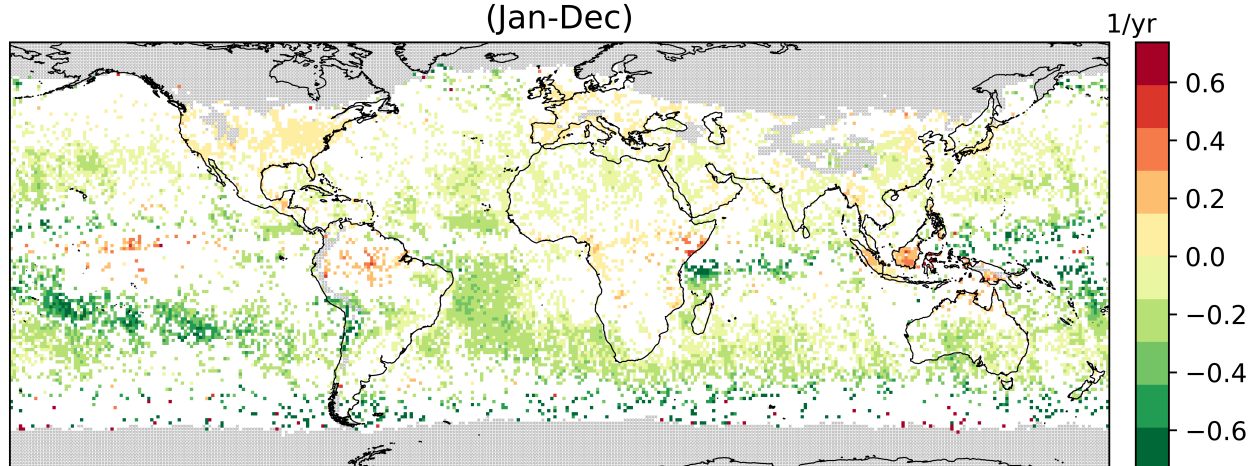
811

812 Figure 21~~20~~: Global trends of OMI HCHO/NO$_2$ tropospheric column ratio over 2005-2019 (see
813 text for details on the calculation of the trends). Grey areas correspond to areas without enough
814 data, white areas correspond to regions where the trends remain statistically insignificant at a
815 95% confidence level.

816

817 The~~se~~ trends on the TrC-HCHO/-TrC-NO$_2$ ratio ~~can be~~is mainly driven by specific trends on TrC-
818 HCHO and/or TrC-NO$_2$, depending on the region. The ratio increase in southern and western
819 Europe and southeast Asia appears primarily due to decreasing TrC-NO$_2$, since TrC-HCHO does
820 not change significantly. Over North America, observed TrC-HCHO values ~~do~~ decrease but ~~the~~
821 less than TrC-NO$_2$, which thus drives the ratio toward an increase. Conversely, the increase of
822 ~~TrC~~ TrC-HCHO/TrC-NO$_2$ in equatorial Africa and Amazonians appears mainly driven ~~to~~by
823 increasing TrC-HCHO. The regions where TrC-HCHO/TrC-NO$_2$ is significantly decreasing
824 include Chile and Australia, due to both decreasing TrC-HCHO and increasing TrC-NO$_2$ (Figure
825 2221), indicating a trend towards a VOC-limited regime. Note that over the US, Jin et al. (2020)
826 demonstrated the reasonable ability of the OMI-based TrC-HCHO/TrC-NO$_2$ trends to capture the
827 transition from RO$_x$-limited to NO$_x$-limited regimes over main US cities and found a relatively
828 good consistency between observed changes of the surface O$_3$ and space-based HCHO/NO$_2$
829 increasing trends. ~~The regions where TrC- TrC-HCHO/TrC-NO$_2$ is significantly decreasing~~
830 ~~include southwestern America and Australia, due to both decreasing TrC-HCHO and increasing~~
831 ~~TrC-NO$_2$ (Figure 21).~~
832
833
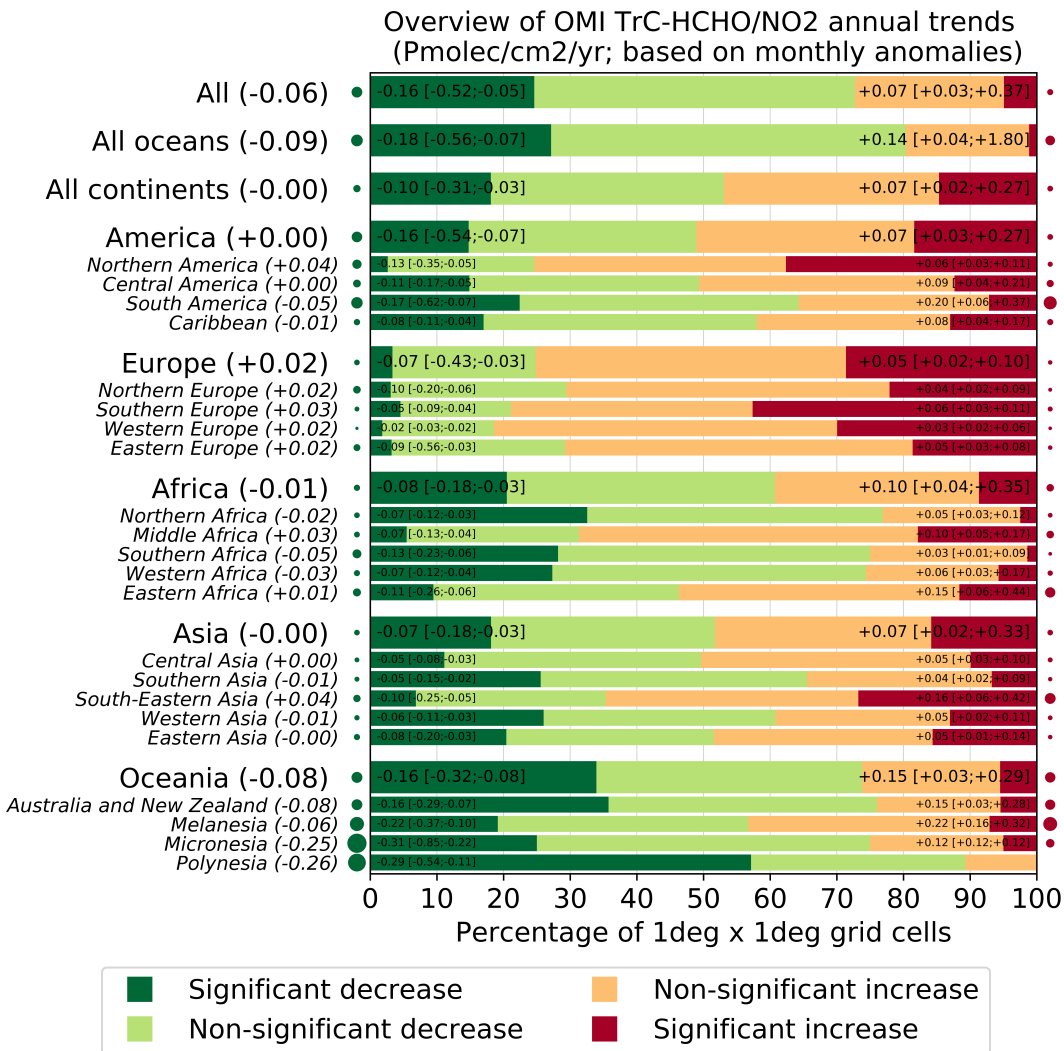
Figure 2221: Summary of the statistically significant and insignificant regional trends of OMI TrC-HCHO/TrC-NO₂ tropospheric column ratio trends over 2005-2019, at a 95% confidence level (see text for details on the calculation of the trends). For each region, the trends reported on the left (resp. right) represent the 5th, 50th and 95th percentiles of the trends calculated over the different grid cells showing a significant TrC-HCHO/TrC-NO₂ increase or decrease.

842

3.5. Lightning NO$_x$ and Its Effects on ~~NO$_x$ and~~ Tropospheric NO$_x$ and O$_3$

Nitric oxide (NO) is produced in lightning flash channels and quickly comes into equilibrium with NO$_2$. Cloud-scale simulations of thunderstorms indicate that 55-75% of lightning NO$_x$ (LNO$_x$) is detrained above 8 km (Pickering et al., 1998) where it enhances upper tropospheric NO$_y$, OH, and O$_3$ (Labrador et al., 2005; Allen et al., 2010; Liaskos et al., 2015) and contributes to enhanced longwave radiative absorption ~~positive radiative forcing~~ by O$_3$ (Lacis et al., 1990; Finney et al., 2018) ~~and negative radiative forcing by CH$_4$.~~ Enhanced OH leads to a decrease in CH$_4$ lifetime and decreased longwave radiative absorption (Fiore et al., 2006; Finney et al., 2018). The lifetime of NO$_x$ in the upper troposphere is controlled by the chemical cycling of NO$_x$ with reservoir species and is 10-20 days away from deep convection (Prather and Jacob, 1997) but only 2-12 hours in the vicinity of convection (Nault et al., 2016, 2017). This chemical recycling provides a source of NO$_x$ downwind of thunderstorms, which causes the ozone production efficiency of emitted NO$_x$ to be 4-20 times higher in the upper troposphere than at the surface. Thus, LNO$_x$ has a disproportionate impact on the tropospheric O$_3$ budget (Pickering et al., 1990; Grewe et al., 2001; Sauvage et al., 2007).

The distribution of lightning is fairly well known over much of the Earth due to remote sensing observations and an increase in the number and capability of ground-based lightning networks. However, the LNO$_x$ production efficiency (PE, mol fl^{-1}) is a continued source of uncertainty. Schumann and Huntrieser (2007) reviewed the literature on LNO$_x$ production, finding a best estimate of 250 moles per flash, with uncertainty factors ranging from 0.13 to 2.7. The PE can be estimated from theoretical and laboratory considerations (Price et al., 1997; Koshak et al., 2014), using thunderstorm anvil observations by aircraft (Ridley et al., 2004; Huntrieser et al., 2008, 2011; Pollack et al., 2016; Nault et al., 2017; Allen et al., 2021a), based on satellite data (Bucsela et al., 2010; Beirle et al., 2010; Pickering et al., 2016; Bucsela et al., 2019; Lapierre et al., 2020; Zhang et al., 2020; Allen et al., 2019, 2021b), or using cloud-resolved (e.g., DeCaria et al., 2000; 2005; Fehr et al., 2004; Ott et al., 2007, 2010; Cummings et al., 2013; Pickering et al., 2023) or global model simulations with chemistry (e.g. Martin, et al., 2007; Murray et al., 2012; Miyazaki et al., 2014; Marais et al., 2018). These various techniques have yielded PE estimates ranging from <50 to >1000 mol fl^{-1}, with most estimates in the 100-400 mol fl^{-1} range. Miyazaki et al. (2014) assimilated OMI NO$_2$, MLS and TES O$_3$, and MOPITT CO into a chemical transport model to provide comprehensive constraints on the global LNO$_x$ source, resulting in an estimate of mean PE of 310 moles per flash. Marais et al. (2018) used cloud-sliced upper tropospheric NO$_2$ from OMI together with the GEOS-Chem model to estimate a mean LNO$_x$ PE of 280 moles per flash. Lightning is the dominant source of NO$_x$ in the tropical upper troposphere year-round and in the northern mid-latitudes in summer. Lightning is responsible for 10-15% of NO$_x$ emissions globally. Assuming 100-400 mol fl^{-1}, the global LNO$_x$ production is likely 2 – 8 Tg N a^{-1} (Schumann and Huntrieser, 2007; Verma et al., 2021).

LNO$_x$ impacts air quality and deposition (Kaynak et al., 2008; Allen et al., 2012). On average LNO$_x$ adds 1-2 ppbv to surface O$_3$ (Kang et al., 2019b), although contributions as large as 18 ppbv have been seen for individual events (Murray et al., 2016). Allen et al. found that the addition of LNO$_x$ to the Community Multiscale Air Quality (CMAQ) model increased wet deposition of oxidized nitrogen at National Atmospheric Deposition Program (NADP) sites by 43%, reducing low biases from 33% to near-zero. Kang et al. (2019b) found similar improvements for wet deposition and also found that including LNO$_x$ resulted in smaller biases with respect to ozonesondes and aircraft profiles taken during the NASA DISCOVER-AQ field campaign (Flynn

et al., 2016). Thus, to accurately assess its impacts on air quality, it is critical that LNO_x-producing deep convection is accurately simulated.

Lightning is the dominant source of NO_x in the tropical upper troposphere year-round and in the northern mid-latitudes in summer. Lightning is responsible for 10-15% of NO_x emissions globally. This is 2 – 8 Tg N a^{-1} (Schumann and Huntrieser, 2007; Verma et al., 2021) or 100 to 400 mol per flash. Much of the uncertainty stems from limited knowledge of lightning NO_x PE per flash or per unit flash length. Most LNO_x is injected into the mid- and upper-troposphere where (away from deep convection) its lifetime is longer relative to lower troposphere NO_x. LNO_x plays an important role in determining mid- and upper-tropospheric concentrations of the hydroxyl radical (OH), the atmosphere's cleanser; CH_4, an especially potent greenhouse gas; and O_3, a greenhouse gas and pollutant.

Only in recent years with the advent of satellite observations of lightning flashes and improved coverage by ground-based lightning networks has there been sufficient data to make estimates of trends in the occurrence of lightning. However, it is unknown whether trends in LNO_x production are similar to those of lightning itself. Lightning characteristics such as the ratio of intracloud (IC) flashes to cloud-to-ground (CG) flashes, the multiplicity (i.e., the number of strokes per flash), and the peak current or energy associated with flashes may vary over time. All of these lightning characteristics may have effects on the magnitude of LNOx production. We have insufficient data to take into account these possible effects on LNO_x production over large spatial domains or over sufficiently long periods of time.

3.5.1. Global Historical ~~trends~~ Trends of ~~Lightning~~LNOx

The first attempts at an examination of trends in thunderstorm activity were conducted in terms of thunder-days (in Japan by Kitagawa et al., 1989; in Brazil by Pinto et al., 2013). A more recent global analysis was conducted by Lavigne et al. (2019), who analyzed trends in thunder-days (number of days with audible thunder at weather observation stations) over 43 years and in flashes recorded by the Lightning Imaging Sensor (LIS) on the Tropical Rainfall Measuring Mission (TRMM) for 16 years. Thunder-days increased since the 1970s in the Amazon Basin, the Maritime Continent, India, Congo, Central America, and Argentina. Decreases in thunder-days were found in China, Australia, and the Sahel region of Africa. Lavigne et al. (2019) do not provide a global trend in thunder days, but an average trend computed over the nine primary lightning regions that they considered, weighted by the mean annual thunder days in each region, yields a near global estimate of +3.8% per decade. How well do thunder-days represent lightning flash rate? Lavigne et al. found a positive correlation between thunder-days and LIS flash rates in China, the Maritime Continent, South Africa and Argentina, but disagreement on the trend in India and West Africa.

Large-scale (±38° latitude) trends in lightning flashes have been examined in the data collected by the LIS on the TRMM satellite (January 1998 – December 2014) and on the International Space Station (February 2017 – December 2021). Füllekrug et al. (2022; see Figure SB2.1b) demonstrate that the annual mean deviations from the 1998 – 2021 mean are no more than ~5% except for ~-10% in 2020 and ~-8% in 2021. However, no long-term trend is evident from the LIS data. The possibility that these larger negative deviations in 2020 and 2021 are due to Covid-19 lockdowns and general declines in economic activity has been speculated. The link may be provided by changes in Aerosol Optical Depth (AOD) as suggested by Liu et al. (2021) who demonstrated 10-20% flash reductions in March – May 2020 relative to the 2018 – 2021 mean for those months from the GLD360 and WWLLN ground-based lightning networks. Regional lightning reductions were consistent with AOD reductions noted by Sanap (2021). Larger reductions in lightning were noted over Africa/Europe and Asia/Maritime Continent and lesser reductions over the Americas.

3.5.2. Regional Historical Trends of Lightning~~LNO~~_x

Widely varying trends in lightning over China have been reported in the literature. To some extent, whether the trend in lightning is upward or downward depends on the particular region studied and on the period of time considered. Yang and Li (2014) were the first to report on lightning trends in China. They used lightning data from the TRMM/LIS sensor and human-observed thunderstorm day occurrence over the period 1990 to 2012 in southeastern China. Thunderstorms and lightning occurrence increased over the period as well as LIS precipitation radar echo tops heights. These increases were accompanied by decreases in visibility, indicating increases in pollution aerosol. Detailed work on lightning trends in China has been performed in relation to aerosols. Shi et al. (2020) correlated flashes from the TRMM/LIS Low-Resolution Monthly Time Series (2.5 deg. resolution) with AOD from MODIS-Terra V6.1 Level 3 over the period 2001 to 2014. For AOD < 1.0, r = 0.64, indicating a likely microphysical effect on lightning flash rate. For AOD > 1.0, r = -0.06, which could indicate that with higher aerosol concentration there is a radiation effect stabilizing the atmosphere and/or a decrease in the number of graupel particles in the mixed-phase region of the storms that is important for charging. Flashes were also correlated with surface relative humidity and Convective Available Potential Energy (CAPE). As AOD generally increased over much of the early portion of this time period and then decreased, lightning flash rates followed similar trends. Wang et al. (2021) examined a 9-year record (2010- 2018) of CG lightning from the China Lightning Detection Network in three polluted urban areas of China (Chengdu, Wuhan, and Jinan). They found decreasing trends (see Wang et al., 2021) in CG lightning and total AOD (from the MERRA-2 reanalysis). Annual mean lightning density in these three regions decreased by 50 – 75% as annual mean AOD fell from 0.70 – 0.75 to 0.53 to 0.62.

Qie et al. (2022) analyzed the OTD/LIS record from 1996 through 2013, and found that lightning increased over the eastern Tibetan Plateau by $0.072 \pm .069$ fl km^2 yr^{-1}. Over the 18 years, this increase amounted to a total of 1.3 fl km^2 yr^{-1}, compared with a climatological value of 7.7 fl km^2 yr^{-1}, thereby indicating a significant increase. The ground-based World Wide Lightning Location Network (WWLLN) also showed an increase in strokes in this region. The increase in lightning frequency in this region was found to be due to an increase in thunderstorm frequency, and not due to increased storm intensity. ~~Xue et al. (2021) found a highly significant downward trend of thunder and lightning days observed at surface weather stations in China between 1961 and 2013, particularly in the warm season. The decrease amounted to 6.5 days per decade, averaged over mainland China. Factors thought to be contributing to this decrease include a decrease in the north-south geopotential height gradient, weakening of the westerly jet stream, decreased relative humidity in the lower troposphere and a decrease in the vertical wind shear between the surface and 6 km altitude.~~

Koshak et al. (2015) analyzed National Lightning Detection Network (NLDN) CG flashes over the contiguous United States (CONUS) from 2003 to 2012. The five-year mean flashes over 2008 to 2012 decreased by 12.8% from the five-year mean for 2003 to 2007 (Table 1). The CONUS average wet bulb temperature also trended downward during this period, which may have led to lesser or weaker storms. However, US Environmental Protection Agency air quality trends show an 18% decrease in PM2.5 concentrations over CONUS between the two subperiods, which also could have had an influence on the flash rates. ~~The decrease in CG flashes was slightly larger (14.8%) over the region of CONUS south of 38 deg. N latitude. However, the TRMM/LIS instrument, which detects both CG and IC flashes, showed little change in flashes over the period of interest south of 38 degrees, suggesting that perhaps the number of IC flashes increased in this region.~~ A recent effort to update the Koshak et al. (2015) analysis is underway. NLDN flashes have been reprocessed (Kenneth Cummins, personal communication) from 2015 through 2021 to

981 ensure that the classification of IC and CG flashes is done consistently with data prior to 2015.
982 Trend analysis of NLDN CG flashes from 2003 (a major upgrade of the NLDN network hardware)
983 through 2022 (William Koshak, personal communication) shows a significant reduction in CG
984 flashes over CONUS, comparing the mean CG flashes over 2003-2004 with the mean over 2021 -
985 2022. Within this period a major decrease (~25%) in CONUS CG flashes occurred from 2011 to
986 2012. Flashes in 2013 remained low, but recovered by 2014-2015. A major decrease (~27%)
987 occurred from 2019 to 2020, with a small increase in 2021. These results have been obtained from
988 ongoing efforts by Dr. William Koshak of the NASA Marshall Space Flight Center, and are
989 presently part of a draft manuscript by lead author Koshak that extends and refines the earlier work
990 in Koshak et al. (2015). Details concerning these trends will be contained in that manuscript.

991 A possible contributing factor to the CONUs decline in CG flashes over 2003 to 2021 is the
992 substantial decrease in aerosol. Surface annual average PM2.5 concentrations averaged over
993 CONUS decreased by 37% from 2000 to 2021 according to the EPA National Air Quality Trends
994 Report (https://www.epa.gov/air-trends/air-quality-national-summary). However, no decrease in
995 CONUS annual average PM2.5 was seen from 2019 to 2020. As mentioned previously, AOD may
996 be a better indicator of the aerosol amount that may become incorporated into thunderstorm clouds.
997 Sanap (2021) showed negative anomalies of AOD of ~0.1 in portions of CONUS in March and
998 April 2020 and 0.1 to 0.2 in May 2020. The major decrease in CONUS CG flashes from 2011 to
999 2012 has been related to drought conditions during Summer 2012 over the South Central and
1000 Southeastern US (Koshak et al., 2015). The reason for the number of CONUS flashes remaining
1001 lower in 2013 is uncertain. Koehler (2020) analyzed 26 years (1993 – 2018) of NLDN CG
1002 lightning data to construct a thunder-day climatology for CONUS. Positive anomalies from the
1003 26-year mean were found from Texas to Colorado during 2003 to 2007, and negative anomalies
1004 in this region during 2008 to 2012. These anomalies were consistent with precipitation anomalies
1005 associated with ENSO.

1006

1007 Table 1. The 5-year flash counts and associated percent changes over CONUS. From Koshak et
1008 al. (2015).

Period	NLDN	NLDN (up to 38°N)	LIS (raw)	LIS (corrected*)
2003 - 2007	25,204,345.8	15,931,940.6	92,655.0	46,997,805.4
2008 - 2012	21,986,578.8	13,574,876.0	92,659.4	47,175,192.4
Change (%)	-12.77	-14.79	0.005	0.38

1009 *Corrected for detection efficiency and view time
1010

1011

1012 Holzworth et al. (2021) analyzed primarily CG lightning data from WWLLN for June, July, and
1013 August for the years 2010 through 2020. The ratio of lightning strokes north of 65° N latitude to
1014 the total global strokes increased by a factor of three over this period. This increase occurred as
1015 the surface temperature anomaly in this region increased by 0.3°C (see Holzworth et al., 2021).
1016 These results suggest a substantial increase in upper tropospheric NO_x and subsequent ozone
1017 production at high northern latitudes.

1018

1019 **3.5.3.   Future LightningLNO_x trendsTrends**

1020 Price (2013) discusses an apparent paradox concerning lightning in future climate. On one hand
1021 increased tropical convection will transport more water vapor to the upper troposphere where it is

1027   Parameterizations in global chemistry and climate models have been developed for
1028 lightning flash rate. These schemes typically use kinematic, thermodynamic or microphysical
1029 variables from the model as predictors. In some studies such predictors have simply been applied
1030 to output from multiple climate models. This is the case with the Romps et al. (2014) work, which
1031 showed that when a lightning parameterization scheme using CAPE x Precipitation Rate is applied
1032 to 11 climate models an increase in CG lightning by 12 +/- 5% per degree Celsius of climate
1033 warming was computed. This work simply used the 12-hour resolution time series of spatial means
1034 of these variables over CONUS as input. Changes in IC lightning flashes were not considered. IC
1035 flashes typically outnumber CG flashes by a factor of 3 averaged over CONUS. Therefore, the
1036 result of this work is unknown with respect to the amount of change in LNO_x emission. Romps et
1037 al. (2018) updated their analysis using CAPE from 3-hourly North American Regional Reanalysis
1038 (NARR) data and hourly precipitation from NOAA River Forecast Centers, finding that CAPE x
1039 Precipitation Rate captures the spatial, seasonal, and diurnal variations of NLDN CG flash rate
1040 over land, but does not predict the pronounced land-ocean contrast in flash rates. Therefore, these
1041 analyses are of limited value in estimating trends of LNO_x over broader-scale regions. Romps et
1042 al (2019) tested four lightning proxies in a cloud-resolved 4-km resolution simulation over
1043 CONUS with the Weather Research and Forecasting (WRF) model, and over the tropical oceans
1044 with a Radiative Convective Equilibrium model. The proxies were CAPE x Precipitation Rate,
1045 precipitation with vertical velocity > 10 m/s, vertical ice flux at the 260K isotherm, and vertical
1046 integral of cloud ice and graupel product. The fractional change in proxy values per 1 degree
1047 Celsius of warming over CONUS was +8 to +16%. Over the tropical oceans the changes in proxy
1048 values per degree ranged from +12% for CAPE x Precipitation Rate to -1% for ice flux and -3%
1049 for the cloud ice and graupel product. Therefore, over broad regions of the Earth, there is great
1050 uncertainty on future trends in lightning.

1051   Finney et al. (2016; 2018) compared lightning projections for 2100 using vertical ice flux
1052 (Finney et al., 2014) and cloud-top height parameterizations for flash rate in the UK Chemistry
1053 and Aerosols Model. They obtained -15% global change in total flash rate with ice flux under a
1054 strong global warming scenario (see Finney et al., 2018), which was composed of a greater
1055 decrease in the tropics and small increases in mid-latitudes. In terms of LNO_x emissions this work
1056 using the ice flux scheme produced -0.15 TgN K^{-1} change over the years from 2000 to 2100,
1057 implying less O_3 production. With the cloud-top height scheme they obtained +0.44 TgN K^{-1} LNO_x
1058 change, implying increased O_3 production. However, the ice flux scheme provided a more realistic
1059 representation of global lightning for present day. Therefore, the negative LNO_x emissions change
1060 from this scheme may be more realistic. If indeed the ice flux scheme better represents the current
1061 distribution of lightning, both the Romps and Finney results suggest no significant increase in
1062 LNO_x emission in future climate, and possibly a small global decrease. Murray (2018) points out
1063 that the ice flux scheme is a closer representation of the underlying charging mechanism, but this
1064 scheme needs to be tested in multiple global chemistry and climate models.

1065

1066   ### 3.5.4.   Recent findings concerning LNOx PE

1067   Recent satellite-based estimates of LNO$_x$ production (Figure 2322Figure 22) have suggested a
1068   possible flash rate dependence of LNO$_x$ production per flash (Bucsela et al., 2019; Allen et al.,
1069   2019; 2021). Smaller values of LNO$_x$ PE in these studies were found to be associated with high
1070   flash rates, likely due to smaller flashes in these conditions (Bruning and Thomas, 2015). Allen et
1071   al. (2021a) noted positive correlations (Figure 2322Figure 22) of LNO$_x$ PE with flash energy and
1072   with flash multiplicity (number of strokes per flash). Laboratory studies by Wang et al. (1998)
1073   found a positive correlation between peak current and LNO$_x$ production. Koshak et al. (2015)
1074   found an 8% increase in peak current from the 2003-2007 period to the 2008-2012 period that
1075   accompanied the 12.8% decrease in CG flashes. These findings make it difficult to project future
1076   LNO$_x$ production given only a prediction of future lightning flashes.

1077
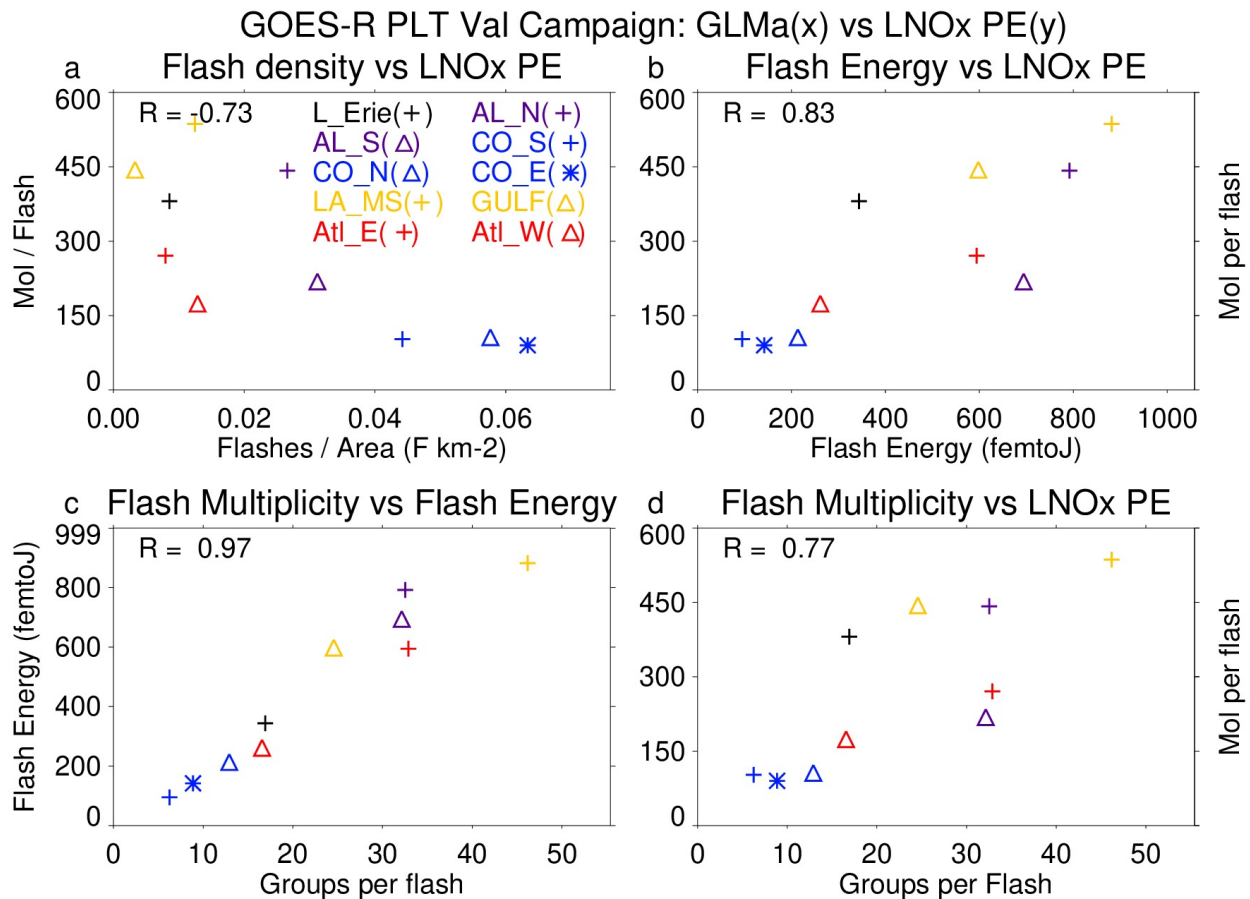
1078

1079   Figure 2322. Scatterplots showing the GLMa-derived relationship between (a) LNO$_x$ PE (mol
1080   per flash) and flash density (flashes km−2), (b) LNO$_x$ PE and flash energy (fJ), (c) flash energy
1081   and flash multiplicity, and (d) LNO$_x$ PE and flash multiplicity. Colors are used to separate flight
1082   days while symbols are used to separate system within each flight day. Correlations are shown in
1083   the upper right. LNO$_x$ PE derived from airborne remote sensor, the Geo-CAPE Airborne
1084   Simulator (GCAS) during the GOES-R Post-launch Test field campaign. GLMa indicates
1085   Geostationary Lightning Mapper data adjusted for missing data. From Allen et al. (2021a).

1086

3.5.5. Impacts of LNOx on upper tropospheric O₃

The literature concerning the effects of lightning NO_x production on upper tropospheric ozone focuses on photochemical ozone production in storm outflow The STERAO-A storm simulation by DeCaria et al. (2005) indicated that additional ozone production attributable to lightning NO within the storm cloud during the lifetime of the storm was very small (~2 ppbv). However, simulation of the photochemistry over the 24 hours following the storm showed that an additional 10 ppbv of ozone production in the upper troposphere can be attributed to lightning NO production. Convective transport of HO_x precursors led to the generation of a HO_x plume, which substantially aided the downstream ozone production. Ott et al. (2007) simulated the July 21, 1998 EULINOX thunderstorm. During the storm, the inclusion of lightning NO_x in the model combined with convectively-transported boundary layer NO_x from the Munich, Germany region resulted in sufficiently large NO_x mixing ratios to cause a small titration loss of ozone (on average less than 4 ppbv) at all model levels. Simulations of the chemical environment in the 24 hours following the storm show on average a small increase in the net production of ozone at most levels resulting from lightning NO_x, maximizing at approximately 5 ppbv per day at 5.5 km. Between 8 and 10.5 km, lightning NO_x caused decreased net ozone production. Ren et al. (2008) found that net tropospheric ozone production proceeded at a median rate of ~11 ppbv per day above 9 km in the Intercontinental Transport Experiment (INTEX-A) in which the effects of frequent deep convection over the United States dominated the upper troposphere. Apel et al. (2012) noted that a box model calculation indicated a net ozone increase of ~10 ppbv over a few hours following observed convection with lightning over Canada in the Arctic Research of the Composition of the Troposphere from Aircraft and Satellite (ARCTAS) experiment. Apel et al. (2015) performed box modeling of the chemistry downwind of two DC3 storms in northeast Colorado on June 22, 2012 , finding ~~The northern storm ingested fresh biomass burning smoke, and the southern storm was affected by more aged biomass burning emissions. The model predicted substantial downwind ozone production in the UT for both storms. The southern storm was predicted to produce more~~greater ozone production over 2 days (14 ppbv) in the southern storm with more LNO_x than in the northern storm (11 ppbv) ~~despite having lower VOC OH reactivity. Sensitivity tests showed that this was principally due to more NO_x being present in the southern storm outflow because of LNO_x~~. Brune et al. (2018) studied ozone production in ~~found general agreement between observed and modeled OH and HO_2 in~~ the outflow of the June 21, 2012 DC3 mesoscale convective system. Their ~~In this study the DC-8 made multiple passes through the outflow as it moved downwind.~~ Box model calculations yielded a 13 ppbv increase in ozone over 5 hours, similar to the observed 14 ppbv increase ~~(see Brune et al, 2018)~~. This rate of increase is larger than others in the literature, perhaps because for a portion of the 5 hours the outflow was in cirrus cloud, in which photolysis rates may have been larger than clear-sky values due to multiple scattering. Using a regional chemistry model, Pickering et al. (2023) estimated that net ozone production in the upper tropospheric outflow of a severe high flash rate storm observed over Oklahoma proceeded at a rate of 10-11 ppbv day^{-1} during the first 24 hours of downwind transport. Downwind photochemical production of ozone due to LNO_x accounted for much of the recovery of upper tropospheric ozone following large reductions due to convective transport of lower ozone boundary layer air.

3.5.6. Summary of LNOx

LNO_x is responsible for the largest fraction of upper tropospheric ozone in the tropics year-round and in the mid-latitudes in summer. Effects on longwave radiation ~~Radiative forcing~~ due to ozone are~~is~~ most sensitive due to the ozone near the tropopause. Therefore, it is of great importance to have knowledge of the trends in ozone in this region that are due to changes in frequency and characteristics of lightning flashes. Considerable~~While~~ uncertainty remains concerning trends in

1134 global thunder days~~flash rates~~. No long-term trend in global flash rates has been found. However,~~,~~
1135 regionally important trends have been noted in CONUS and in China, which tend to be correlated
1136 to the decreasing atmospheric aerosol content. An increasing trend at Arctic latitudes has been
1137 noted, as that region rapidly warms. Future trends in flash rate also are uncertain, with conflicting
1138 predictions coming from models with differing flash rate parameterizations. Flash characteristics
1139 (e.g., flash rate, flash extent, flash energy or peak current, intracloud fraction) have been found to
1140 have important implications for LNO_x production per flash. Insufficient knowledge of these
1141 characteristics on a global scale makes it highly uncertain to estimate changes in LNO_x production,
1142 even with knowledge of flash rate trends.

1143

1144 **3.6. Soil NO and HONO emissions and their impacts on O_3**

1145 Nitrous acid (HONO) is produced from microbial activity in soils with a similar mechanism and
1146 strength as NO (Oswald et al., 2013). This emission source may partially account for the current
1147 mismatch between observed and simulated HONO levels in the lower troposphere (Su et al.,
1148 2011; Yang et al., 2020). Zhang et al. (2016) estimate a 29 % contribution of soil-HONO to the
1149 HONO sources in China. This may also contribute significantly to OH production with important
1150 implications for the HO_x and O_3 budget. To account for this emission source and assess the
1151 global potential for atmospheric pollution soil-HONO emissions have been parameterized based
1152 on the HONO/NO emission ratio measured at multiple field samples (taken from different
1153 regions of the world) and up-scale it to the 4 major land cover types applied to the whole globe.
1154 The study estimates a global emission source of 7 TgN/yr from soil-HONO in 2009 (Emmerichs
1155 et al., 2023). This is at the lower end of the estimated range of 7.4-12 TgN/yr presented by Wu et
1156 al. (2022) for 2017 who employ an empirical and statistical model in combination with
1157 observations. Due to the importance of NO and HONO soil emissions for the O_3 budget their
1158 variability and historical and future trends are described here and linked to O_3. Additionally, we
1159 discuss a modification of the soil NO emission scheme.

1160 **3.6.1.   Global modeling of reactive nitrogen emissions from soil**

1161 In this section, we present a short overview of the soil-NO emission algorithms and estimates for
1162 regional and global emissions. The emission of nitrogen oxides (NO) from the soil is the major
1163 source of NO_x in unpolluted regions accounting for 15-25 % of global emissions (Weng et al.,
1164 2020, Vinken et al., 2014). Thereby, NO is produced from the nitrification in soil (microbial
1165 activity) and depends non-linearly on soil properties like pH, carbon and nutrient content,
1166 temperature, and soil moisture (Gödde and Conrad 2000, Oswald et al. 2013). Model algorithms
1167 estimate soil-NO emissions with a function dependent on biological and meteorological drivers.
1168 The common empirical approach by Yienger and Levy (1995), which is used in the current
1169 CMIP6 simulations (Szopa et al. 2022), is based on a biome-specific emission factor, soil
1170 temperature, precipitation, and the canopy uptake reduction factor. The resulting global estimate
1171 is in the range of 3.3-7.7 TgN/yr which is, however, only at the lower end of the more recent
1172 model and observation-based estimates. The Yienge and Levy (1995) approach generally
1173 underestimates soil NO for all landcover types except in the tundra and rainforest due to the
1174 pulsing parameterization, which describes a large NOx release at the wetting of very dry soil and
1175 the subsequent rapid decay (Steinkamp et al., 2009). This is accounted for in the more
1176 mechanistic approach by Hudman et al. (2012) representing pulsing of the emissions following
1177 dry spells and N-inputs from chemical fertilizer and atmospheric N-deposition. This approach
1178 calculates spatial and temporal patterns of soil moisture, temperature, pulsing, fertilizer, manure
1179 and atmospheric N deposition and biome overall replacing the emission factors by Yienger and

1180 Levy (1995) which yields in comparison 34 % more annual global soil emissions of nitrogen
1181 oxide (10.7 TgN/yr). Satellite top-down estimates range from 7.9 TgN/yr (Miyazaki et al., 2017:
1182 2005-2014, assimilation of satellite data sets) to 16.7 TgN/yr (Vinken et al., 2014; GEOS-Chem
1183 and OMI). The emission of soil-NO varies regionally with small sources in Australia (~0.5
1184 TgN/yr), Europe, Russia and Southern Hemisphere (SH) Africa (0.7 TgN/yr, 0.8 TgN/yr),
1185 America (0.9-1 TgN/yr) and high values in S.E. Asia and Northern Hemisphere (NH) Africa (2-
1186 2.1 TgN/yr). The emission estimates (here for 0.25° lat. × 0.3125° lon.) increase with resolution
1187 in some regions like Europe by 38 % (Weng et al., 2020).

1188 Nitrous acid (HONO), a major OH source, is also produced from microbial activity in soils with
1189 a similar mechanism and strength as NO (Oswald et al., 2013). This additional emission source
1190 may account for the current mismatch between models and measurements representing HONO
1191 levels in the lower troposphere (Su et al., 2011; Yang et al., 2020). Soil emissions of HONO play
1192 a major role in the daytime-HONO concentrations in rural areas (in the lowest layers) where
1193 traffic emissions and NO_2 heterogeneous reactions occur less than in urban areas (Wu et al.
1194 2022). HONO photolysis is a main OH source and impacts the oxidation capacity of the
1195 atmosphere (Zhang 2016, 2019). Therefore, this may also contribute significantly to OH
1196 production with important implications for the HO_x and O_3 budget.

3.6.2.   Variability and trends of soil emissions of NO and HONO in the last 15 years

1198 The magnitude of soil emissions varies strongly with season where the emissions rise from
1199 January and July by a factor of 2.5 (Weng et al., 2020). This follows the meteorological
1200 variability as for instance, heavy rainfall over dry grasslands/forests causes a pulse of soil NO
1201 emissions coupled with the usage of fertilizer (Hudman et al., 2012). According to the CCMI
1202 simulations by Jöckel et al. (2016) (following the future ('medium high') climate scenario
1203 RCP6.0 the soil NO emissions show a positive trend since pre-industrial times with a steeper
1204 increase of up to 0.3 TgN/decade from the year 2000. As soil emissions of HONO rely on the
1205 same biogeochemical process with similar dependencies on temperature and water content as NO
1206 also increased from 2000 to 2019.

1207 For soil-HONO, however, the trend over 2005-2019 is much smaller, most pronounced in
1208 Central Africa (Figure 2524Figure 24). Thereby, the highest positive monthly anomalies occur
1209 mainly in the 5 most recent years which is likely due to the more frequent heat wave occurrence,
1210 e.g. in Europe and North America. Overall, Africa relates the most (~30%) to the global anomaly
1211 (Figure 2423Figure 23 - Figure 2524Figure 24).

1212
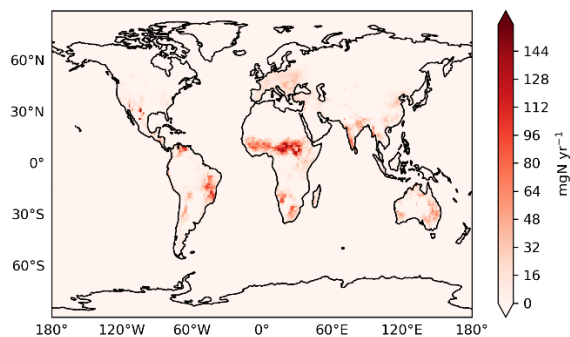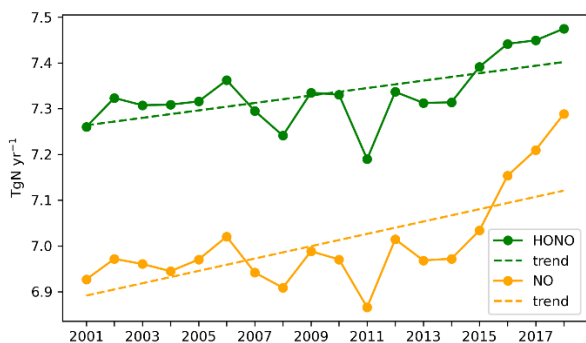
1213

1214 Figure 2423: Time series of soil-HONO and soil-NO emissions and their trends (left) and the
1215 mean global distribution of the soil-HONO emission trend for 2005-2019 based on monthly
1216 anomalies (right).

1217

1218 ~~Since soil-HONO emissions contribute 10-20 % to surface O₃, most significantly in the Southern~~
1219 ~~Hemisphere (Wu et al., 2022), its positive emission trends may have contributed to the decrease~~
1220 ~~in O₃ over the last 15 years (see other sections).~~

1221
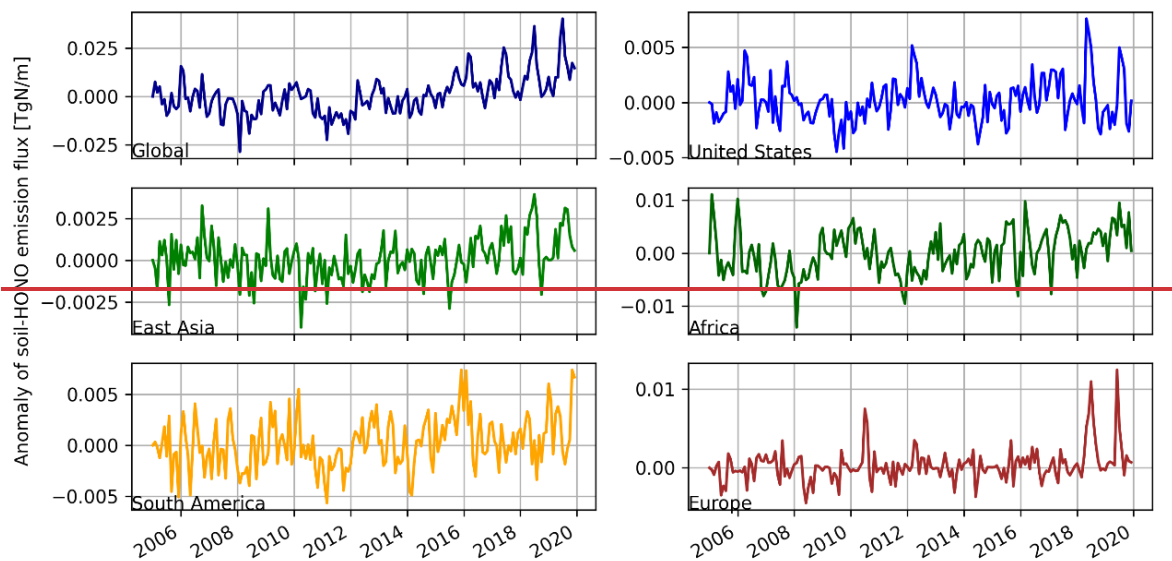
1222
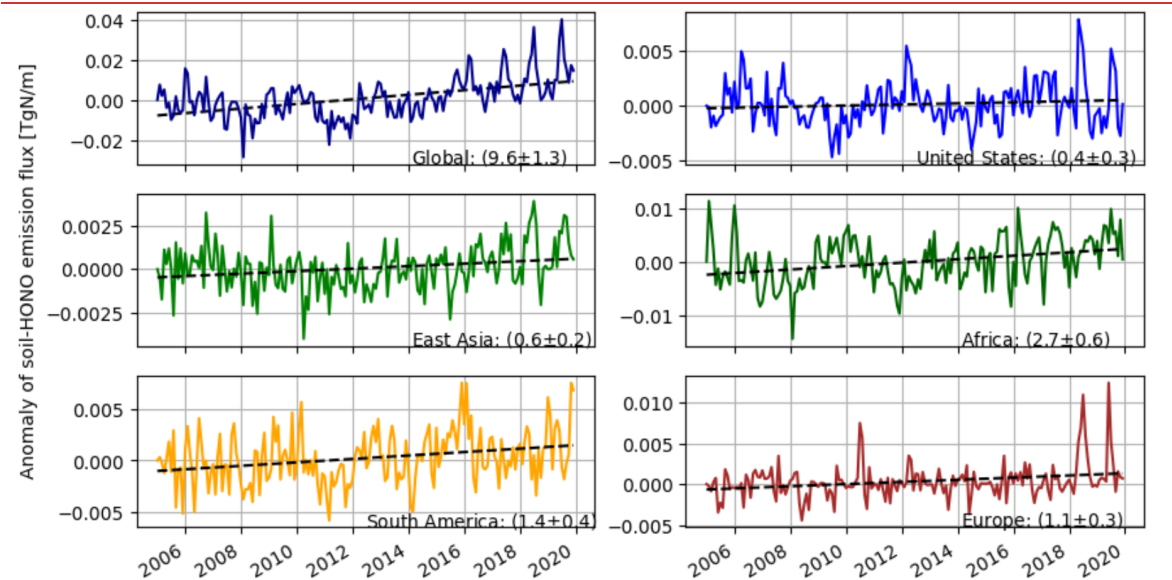
1223

1224 Figure 2524: Monthly anomalies of HONO emissions from soil (de-seasonalized). The trend is
1225 given in 10^{-5}, including the uncertainty estimate (2*standard deviation).

1226

1227

1228 ### ~~3.6.5.~~3.6.3. Canopy Reduction Factor

1229 Most NO soil emission models (Yienger and Levy, 1995; Hudman et al., 2012) rely on an
1230 empirical canopy reduction scheme which represents loss processes in plants as the diffusion of
1231 NO_2 through the stomata and direct deposition to the cuticle. In particular, a large fraction of
1232 NO_x (and peroxyacyl nitrate) loss during the night may be only explainable by non-stomatal
1233 processes (Delaria et al., 2020b). Mechanistically, the canopy reduction can be described by an
1234 efficient NOx deposition to plants. Thus, Delaria et al. (2020a) points out that models already
1235 represent the uptake by vegetation and do not need to use a canopy reduction scheme. The
1236 potential change of NO soil emissions is shown by employing the global model
1237 ECHAM/MESSy (1°x1°) with an explicit trace gas uptake at stomata and cuticle (Emmerichs et
1238 al., 2021) for two different seasons in 2005 and 2006. Removing the canopy reduction factor in
1239 the model leads to a significant increase of soil NO emissions highest over tropical forests
1240 (Figure 2625~~Figure 25~~). The temporal variation follows the vegetational growth as in the
1241 Northern Hemisphere summer 50% higher emissions occur. These findings are reasonable as
1242 Hudman et al. (2012) estimated that the canopy reduction scheme overall lowers the NO
1243 emissions by 10-15% at grasslands and up to 85% over forests (GEOS-Chem at 2°×2.5° in
1244 2006). Consequently, improper accounting for the canopy reduction factor may imply a strong
1245 underestimation of the soil-N in densely forested regions and globally by about 31% (2005-
1246 2006).

1247
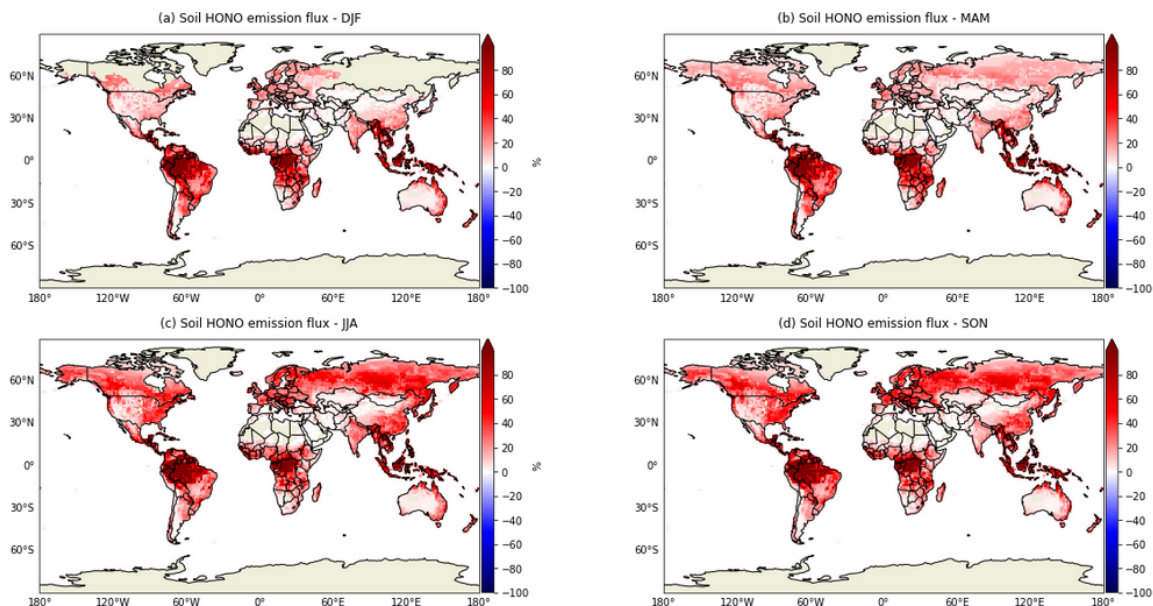
1248
1249 Figure 26~~25~~: Relative difference Canopy Reduction soil HONO

1250

1251 ### ~~3.6.6.~~3.6.4. Projections of soil NO and variability in different climates

1252 The future land use is predicted to change as a consequence of the growing demand for
1253 nutrition and biofuels which implies an increasing use of fertilizer. Consequently, NO soil
1254 emissions are estimated to rise by ~28% during the century to 11.5 TgN/yr at the end of 2100
1255 (Fowler et al., 2015). Similarly, Liu et al. (2021) estimate an increasing soil NO emission of 8.9
1256 TgN/yr by the year 2050 due to intensive nitrification processes.

An increase of LAI by 10 %, in contrast, would lead to 1% lower emissions. In addition, several responses are expected from the changing climate. In fact, the 1°C higher temperature would cause ~5% increase of emissions (Weng et al., 2020). Following the future ('medium high') climate scenario RCP6.0 (Representative Concentration Pathway, 6 W/m2 radiative forcing until 2500, stabilization after 2150) used for the CMIP5 (Climate Model Intercomparison Project) simulations. Jöckel et al. (2016) suggest an increase of ~15 % soil NO emissions due to increasing soil temperature (an increase of soil microbes) since present-day (2010) until 2100. However, the most significant implications for large-scale denitrification activity are changing rainfall and the regional hydrological cycles (Fowler et al., 2015). In general, soil NOx will play a more important role for the global budget in the troposphere due to the decreasing anthropogenic emissions in the future. Therefore, increasing NOx-soil emissions may slow down the decrease of O3 in response to declining anthropogenic emissions (Wu et al. 2022).

~~3.6.7.~~3.6.5. Next steps with biogeochemical models implemented in ESMs

Uncertainties of modeling soil nitrogen emissions are associated with the model input and parameters (Wang and Chen 2012). Process-based biogeochemical models which also consider the complexity of soil emission processes as DNDC (Denitrification–Decomposition) are needed (Li et al., 2011). The capability to represent interactive biogeochemical cycles allows for instance for the online calculation of crop nutrition from soil. Also, a model like CLM5 distinguishes between natural and agricultural soils which more accurately predicts the fertilizer usage (Fung et al., 2022). Resolving the soil and litter biogeochemical dynamics vertically, in addition, lead to a more efficient retainment and recycling of N by the ecosystem (Koven et al., 2013). However, these models should be calibrated to multiple sites (Wang et al., 2019) which is limited by the availability of measurement data, especially when it comes to global modeling.

4. Conclusion

In this article, we investigate temporal and spatial trends and variability of tropospheric ozone in relation to its precursors using satellite products, ozonesonde measurements, and model simulations. Our results show that ozone has positive trends at all latitudes and column depths regardless of the tropopause height within ±100 hPa. The positive trends in the 30-60ºN band are due to increasing trends over Canada and Alaska and are slightly offset by the small negative trends over the northe~~E~~astern US and Europe. The ~~decreasing~~ lower trends ~~above~~ in the bands 30-60ºN and 30-60ºS are due to the offsetting impact of negative trends over Eastern US and Europe in the north, and Australia and South Africa in the south, respectively. The decreasing trends of TrC-O$_3$ over parts of the northe~~E~~astern US and Europe are ~~consistent with~~likely due to the decreasing trend of TrC-NO$_2$, which is due to the effective measures applied over the last two decades to mitigate air pollution in these regions. ~~The decrease of TrC-O$_3$ as a result of decreasing TrC-NO$_2$ trends is due to the NO-sensitive conditions dominating most of these regions. The increasing trends of TrC-O$_3$ in the other regions of the world where TrC-NO$_2$ is decreasing as a result of VOC-sensitive conditions, especially over East Asia.~~ TrC-HCHO trends are decreasing in the Eastern US, some parts of northern and western Africa, and western and northern Europe, and increasing in South Asia, central Africa, northern Australia, and Brazil. TrC-HCHO trends are consistent with that of TrC-O$_3$ over Eastern US and Europe. ~~The decreasing trends of HCHO and O$_3$ as NO$_2$ increases is evidence of the VOC-limited conditions in these regions. Under these conditions, increased NO$_2$ levels lead to a reduction of OH, which~~

decreases the oxidation capacity and thus lowers the photochemical formation of HCHO and O_3. Simulated O_3 and its precursors are in good agreement with satellite measurements. Considering different latitude bands, the TrC-O_3 highest trends are simulated between 30º S and 60º N, consistent with calculated trends based on satellite observations. The middle and upper troposphere make the largest contributions to the simulated TrC-O_3 trend globally, with large contributions from the upper troposphere driving the simulated TrC-O_3 trend at 30°S-30°N and counteracting the negative TrC-O_3 trend in the southern midlatitudes.

We have also shed light on NO_X lightning and its relation to ozone trends. LNO_x is responsible for the largest fraction of upper tropospheric ozone in the tropics year-round and in the mid-latitudes in summer. Ozone Radiative forcing is due to the ozone near the tropopause. An increasing trend of LNO_x at Arctic latitudes has been noted, as that region rapidly warms. However, future trends in flash rate are uncertain, with conflicting predictions coming from models with differing flash rate parameterizations. Soil HONO emissions had their highest positive monthly anomalies mainly in the 5 most recent years which is likely due to the more frequent heat wave occurrence, e.g. in Europe and North America. Soil HONO trends are highest in Africa accounting for ~30% of the global anomaly. Soil NO_x emissions could play an important role in the tropospheric NO_x global budget due to the decreasing anthropogenic emissions in the future. Therefore, the expected increase in NO_x-soil emissions may slow down the decrease of O_3 in response to declining anthropogenic emissions. Overall, this study presented a comprehensive overview of tropospheric ozone trends in relation to its precursors in different spatial and temporal scales.

Competing interests: At least one of the (co-)authors is a member of the editorial board of Atmospheric Chemistry and Physics

Acknowledgment

This study was partially funded by the NSF AGS, grant number 1900795, USF Creative Scholarship Grant 2022. A part of the research was conducted at the Jet Propulsion Laboratory, California Institute of Technology, under a contract with NASA. HP has received funding from the Ministerio de Ciencia e Innovación through the MITIGATE project (grant no. PID2020-113840RA-I00 funded by MCIN/AEI/10.13039/501100011033) and the Ramon y Cajal grant (RYC2021-034511-I, MCIN / AEI / 10.13039/501100011033 and European Union NextGenerationEU/PRTR). The GEOS-GMI simulation was supported by the NASA's Making Earth System Data Records for Use in Research Environments (MEaSUREs) program and the high-performance computing resources for GEOS-GMI were provided by the NASA Center for Climate Simulation (NCCS).

5.   References

Allen, D., Pickering, K., Duncan, B., and Damon, M. (2010), Impact of lightning NO emissions on North American photochemistry as determined using the Global Modeling Initiative (GMI) model, *J. Geophys. Res.*,115, D22301, doi:10.1029/2010JD014062.

Allen, D. J., Pickering, K. E., Pinder, R. W., Henderson, B. H., Appel, K. W., and Prados, A. (2012), Impact of lightning-NO on eastern United States photochemistry during the summer of 2006 as determined using the CMAQ model, *Atmos. Chem. Phys.*, 12, 1737-1758, doi:10.5194/acp-12-1737-2012.

Allen, D. J., Pickering, K. E., Bucsela, E., van Geffen, J., Lapierre, J., Koshak, W., & Eskes, H. (2021b). Observations of Lightning NOx production from Tropospheric Ozone Monitoring Instrument Case Studies over the United States, *J. Geophys. Res.*, 126 (10), https://doi.org/10.1029/2020JD034174.

Allen, D. J., Pickering, K. E., Lamsal, L., Mach, D., Quick, M. G., Lapierre, J., Janz, S., Koshak, W., Kowalewski, M. & Blakeslee, R. (2021a), Observations of Lightning NO_x production from GOES-R Post Launch Test Field Campaign Flights, *J. Geophys. Res.*, 126 (8), https://doi.org/10.1029/2020JD033769.

Allen, D., J., Pickering, K. E., Bucsela, E., Krotkov, N., and Holzworth, R. (2019), Lightning NO_x Production in the Tropics as Determined Using OMI NO_2 Retrievals and WWLLN Stroke Data, J. Geophys. Res., https://doi.org/10.1029/2018JD029824.

Apel, E. C., J. R. Olson, J. H. Crawford, R. S. Hornbrook, A. J. Hills, C. A. Cantrell, L. K. Emmons, D. J. Knapp, S. Hall, R. L. Mauldin III, A. J. Weinheimer, A. Fried, D. R. Blake, J. D. Crounse, J. M. St. Clair, P. O. Wennberg, G. S. Diskin, H. E. Fuelberg, A. Wisthaler, T. Mikoviny, W. Brune, and D. D. Riemer, (2012) Impact of the deep convection of isoprene and other reactive trace species on radicals and ozone in the upper troposphere, *Atmos. Chem. Phys.*, 12, 1135–1150, www.atmos-chem-phys.net/12/1135/2012/doi:10.5194/acp-12-1135-2012.

Apel, E. C., et al. (2015), Upper tropospheric ozone production from lightning NOx-impacted convection: Smoke ingestion case study from the DC3 campaign, *J. Geophys. Res. Atmos.*, 120, doi:10.1002/2014JD022121.

Archibald, A.T., et al. 2020.Tropospheric Ozone Assessment Report: A critical review of changes in the tropospheric ozone burden and budget from 1850 to 2100. Elem Sci Anth, 8: 1. DOI: https://doi.org/10.1525/elementa.2020.034, 2020.

ASDC, MOPITT CO gridded monthly means (Near and Thermal Infrared Radiances) V009 [Data set]. NASA Langley Atmospheric Science Data Center DAAC. Retrieved from https://doi.org/10.5067/TERRA/MOPITT/MOP03JM.009, 2024.

Barret, B., De Mazière, M., and Mahieu, E.: Ground-based FTIR measurements of CO from the Jungfraujoch: characterisation and comparison with in situ surface and MOPITT data, Atmos. Chem. Phys., 3, 2217–2223, https://doi.org/10.5194/acp-3-2217-2003, 2003.

Bauwens, M.; Compernolle, S.; Stavrakou, T.; Müller, J.; Gent, J.; Eskes, H.; Levelt, P.F.; van der A, R.; Veefkind, J.P.; Vlietinck, J.; et al. Impact of Coronavirus Outbreak on NO2 Pollution Assessed Using TROPOMI and OMI Observations. Geophys. Res. Lett. 2020, 47.

Beirle, S., H. Huntrieser, and T Wagner (2010), Direct satellite observation of lightning-produced NOx, *Atmos. Chem. Phys.*, 10(22), 10965-10986, doi:10.5194/acp-10-10965.

Boersma, K., Eskes, H., Richter, A., De Smedt, I., Lorente, A., Beirle, S., Van Geffen, J., Peters, E., Van Roozendael, M., and Wagner, T.: QA4ECV NO_2 tropospheric and stratospheric vertical column data from OMI (Version 1.1) (data set), Royal Netherlands Meteorological Institute (KNMI), https://doi.org/10.21944/qa4ecv-no2-omi-v1.1, 2017a.

Boersma, K., Eskes, H., Richter, A., De Smedt, I., Lorente, A., Beirle, S., Van Geffen, J.,
Peters, E., Van Roozendael, M., and Wagner, T.: QA4ECV NO_2 tropospheric and
stratospheric vertical column data from GOME-2 (Version 1.1) (data set), Royal
Netherlands Meteorological Institute (KNMI), https://doi.org/10.21944/qa4ecv-no2-
gome2a-v1.1, 2017b.

Boersma, K., Eskes, H., Richter, A., De Smedt, I., Lorente, A., Beirle, S., Van Geffen, J.,
Peters, E., Van Roozendael, M., and Wagner, T.: QA4ECV NO_2 tropospheric and
stratospheric vertical column data from SCIAMACHY (Version 1.1) (data set), Royal
Netherlands Meteorological Institute (KNMI), https://doi.org/10.21944/qa4ecv-no2-
scia-v1.1, 2017c.

Boersma, K. F., Eskes, H. J., Richter, A., De Smedt, I., Lorente, A., Beirle, S., van Geffen, J.
H. G. M., Zara, M., Peters, E., Van Roozendael, M., Wagner, T., Maasakkers, J. D.,
van der A, R. J., Nightingale, J., De Rudder, A., Irie, H., Pinardi, G., Lambert, J.-C.,
and Compernolle, S. C.: Improving algorithms and uncertainty estimates for satellite
NO2 retrievals: results from the quality assurance for the essential climate variables
(QA4ECV) project, Atmos. Meas. Tech., 11, 6651–6678, https://doi.org/10.5194/amt-
11-6651-2018, 2018.

Brune, W. H., et al. (2018) Atmospheric oxidation in the presence of clouds during the Deep

Convective Clouds and Chemistry (DC3) study, Atmos. Chem. Phys., 18, 14493–14510,
2018, https://doi.org/10.5194/acp-18-14493-2018.

Bruning, E. C. & Thomas, R. J. (2015), Lightning channel length and flash energy
determined from moments of the flash area distribution, *J. Geophys. Res. Atmos.*,
120, 8925–8940, doi:10.1002/2015JD023766

Buchholz, R.R.; Deeter, M.N.;Worden, H.M.; Gille, J.; Edwards, D.P.; Hannigan, J.W.;
Jones, N.B.; Paton-Walsh, C.; Griffith, D.W.T.; Smale, D.; et al. Validation of
MOPITT carbon monoxide using ground-based Fourier transform infrared
spectrometer data from NDACC. Atmos. Meas. Tech. 2017, 10, 1927–1956.

Buchholz, R. R., Worden, H. M., Park, M., Francis, G., Deeter, M. N., Edwards, D. P.,
Emmons, L. K., Gaubert, B., Gille, J., Martinez-Alonso, S., Tang, W., Kumar, R.,
Drummond, J. R., Clerbaux, C., George, M., Coheur, P.-F., Hurtmans, D., Bowman,
K. W., Luo, M., Payne, V. H., Worden, J. R., Chin, M., Levy, R. C., Warner, J., Wei,
Z., and Kulawik, S. S.: Air pollution trends measured from Terra: CO and AOD over
industrial, fire-prone, and background regions, Remote Sens. Environ., 256, 112275,
https://doi.org/10.1016/j.rse.2020.112275, 2021.

Bucsela, E. J., K. E. Pickering, T. L. Huntemann, R. C. Cohen, A. Perring, J. F. Gleason, R.
J. Blakeslee, R. I. Albrecht, R. Holzworth, J. P. Cipriani, D. Vargas-Navarro, I. Mora-
Segura, A. Pacheco-Hernández, S. Laporte-Molina, (2010) Lightning-generated NO_x
seen by OMI during NASA's TC[4] experiment, *J. Geophys. Res.*, 115, D00J10,
doi:10.1029/2009JD013118.

Bucsela, E., Pickering, K. E., Allen, D., Holzworth, R., and Krotkov, N. (2019), Midlatitude
lightning NO_x Production Efficiency Inferred from OMI and WWLLN Data, *J.
Geophys. Res.*, https://doi.org/10.1029/2019JD030561.

Canadell, J.G., P.M.S. Monteiro, M.H. Costa, L. Cotrim da Cunha, P.M. Cox, A.V. Eliseev,
S. Henson, M. Ishii, S. Jaccard, C. Koven, A. Lohila, P.K. Patra, S. Piao, J. Rogelj, S.

Syampungani, S. Zaehle, and K. Zickfeld: Global Carbon and other Biogeochemical Cycles and Feedbacks. In Climate Change 2021: The Physical Science Basis. Contribution of Working Group I to the Sixth Assessment Report of the Intergovernmental Panel on Climate Change [Masson-Delmotte, V., P. Zhai, A. Pirani, S.L. Connors, C. Péan, S. Berger, N. Caud, Y. Chen, L. Goldfarb, M.I. Gomis, M. Huang, K. Leitzell, E. Lonnoy, J.B.R. Matthews, T.K. Maycock, T. Waterfield, O. Yelekçi, R. Yu, and B. Zhou (eds.)]. Cambridge University Press, Cambridge, United Kingdom and New York, NY, USA, pp. 673–816, doi: 10.1017/9781009157896.007, 2021.

Cazorla, M. and Herrera, E.: An ozonesonde evaluation of spaceborne observations in the Andean tropics, Sci Rep, 12, https://doi.org/10.1038/s41598-022-20303-7, 2022.

Chang K-L, Petropavlovskikh I, Cooper OR, Schultz MG, Wang T. Regional trend analysis of surface ozone observations from monitoring networks in eastern North America, Europe and East Asia. Elem Sci Anth. 2017; 5:50. DOI: 10.1525/elementa.243, 2017.

Chang, K.-L., Cooper, O. R., Gaudel, A., Petropavlovskikh, I., and Thouret, V.: Statistical regularization for trend detection: an integrated approach for detecting long-term trends from sparse tropospheric ozone profiles, Atmos. Chem. Phys., 20, 9915–9938, https://doi.org/10.5194/acp-20-9915-2020, 2020.

Chang K-L, Martin G. Schultz, Gerbrand Koren, Niklas Selke, Guidance note on best statistical practices for TOAR analyses, https://doi.org/10.48550/arXiv.2304.14236, 2023.

Chang, K.-L., Cooper, O. R., Gaudel, A., Allaart, M., Ancellet, G., Clark, H., et al. (2022). Impact of the COVID-19 economic downturn on tropospheric ozone trends: An uncertainty weighted data synthesis for quantifying regional anomalies above western North America and Europe. *AGU Advances*, 3, e2021AV000542. https://doi.org/10.1029/2021AV000542, 2022.

Chang K-L, Martin G. Schultz, Gerbrand Koren, Niklas Selke, Guidance note on best statistical practices for TOAR analyses, https://doi.org/10.48550/arXiv.2304.14236, 2023.

Chang, K.-L., Cooper, O. R., Gaudel, A., Petropavlovskikh, I., Effertz, P., Morris, G., and McDonald, B. C.: Technical note: Challenges of detecting free tropospheric ozone trends in a sparsely sampled environment, EGUsphere [preprint], https://doi.org/10.5194/egusphere-2023-2739, 2024.

Chen, Z., Jane Liu, Xiushu Qie, Xugeng Cheng, Mengmiao Yang, Lei Shu, Zhou Zang, Stratospheric influence on surface ozone pollution in China, Nature Communications, 10.1038/s41467-024-48406-x, **15**, 1, 2024.

Christiansen, A., Mickley, L. J., Liu, J., Oman, L. D., and Hu, L.: Multidecadal increases in global tropospheric ozone derived from ozonesonde and surface site observations: can models reproduce ozone trends?, Atmos Chem Phys, 22, 14751–14782, https://doi.org/10.5194/acp-22-14751-2022, 2022.

Cooper, O. R., Schultz, M. G., Schröder, S., Chang, K. L., Gaudel, A., Benítez, G. C., Cuevas, E., Fröhlich, M., Galbally, I. E., Molloy, S., Kubistin, D., Lu, X., McClure-Begley, A., Nédélec, P., O'Brien, J., Oltmans, S. J., Petropavlovskikh, I., Ries, L.,

Senik, I., Sjöberg, K., Solberg, S., Spain, G. T., Spangl, W., Steinbacher, M., Tarasick, D., Thouret, V., and Xu, X.: Multi-decadal surface ozone trends at globally distributed remote locations, Elementa, 8, https://doi.org/10.1525/elementa.420, 2020.

Cummings, K. A., T. L. Huntemann, and K. E. Pickering (2013), Cloud-resolving chemistry simulation of a Hector thunderstorm, *Atmos. Chem. Phys.*, 13(5), 2757-2777, doi:10.5194/acp-13-2757.

DeCaria, A., K. Pickering, G. Stenchikov, J. Scala, J. Stith, J. Dye, B. Ridley, and P. Laroche, A cloud-scale model study of lightning-generated NO$_x$ in an individual thunderstorm during STERAO-A, *J. Geophys. Res.*, 105, 11,601-11,616, 2000.

DeCaria, A. J., K. E. Pickering, G. L. Stenchikov, and L. E. Ott (2005), Lightning-generated NOx and its impact on tropospheric ozone production: A three-dimensional modeling study of a STERAO-A thunderstorm, *J. Geophys. Res.*, *110*, D14303, doi:10.1029/2004JD005556. Deeter, M., Francis, G., Gille, J., Mao, D., Martínez-Alonso, S., Worden, H., Ziskin, D., Drummond, J., Commane, R., Diskin, G., and McKain, K.: The MOPITT Version 9 CO product: sampling enhancements and validation, Atmos. Meas. Tech., 15, 2325–2344, https://doi.org/10.5194/amt-15-2325-2022, 2022.

De Smedt, I., Theys, N., Yu, H., Danckaert, T., Lerot, C., Compernolle, S., Van Roozendael, M., Richter, A., Hilboll, A., Peters, E., Pedergnana, M., Loyola, D., Beirle, S., Wagner, T., Eskes, H., van Geffen, J., Boersma, K. F., and Veefkind, P.: Algorithm theoretical baseline for formaldehyde retrievals from S5P TROPOMI and from the QA4ECV project, Atmos. Meas. Tech., 11, 2395–2426, https://doi.org/10.5194/amt-11-2395-2018, 2018 Fadnavis, S., Sagalgile, A., Sonbawne, S., Vogel, B., Peter, T., Wienhold, F. G., Dirksen, R., Oelsner, P., Naja, M., and Müller, R.: Comparison of ozonesonde measurements in the upper troposphere and lower Stratosphere in Northern India with reanalysis and chemistry-climate-model data, Sci Rep, 13, 7133, https://doi.org/10.1038/s41598-023-34330-5, 2023.

Duncan, B. N., Strahan, S. E., Yoshida, Y., Steenrod, S. D., and Livesey, N.: Model study of the cross-tropopause transport of biomass burning pollution, Atmos. Chem. Phys., 7, 3713–3736, https://doi.org/10.5194/acp-7-3713-2007, 2007.

Elguindi, N., Granier, C., Stavrakou, T., Darras, S., Bauwens, M., Cao, H., Chen, C., Denier van der Gon, H. A. C., Dubovik, O., Fu, T. M., Henze, D. K., Jiang, Z., Keita, S., Kuenen, J. J. P., Kurokawa, J., Liousse, C., Miyazaki, K., Müller, J. F., Qu, Z., Solmon, F., and Zheng, B.: Intercomparison of Magnitudes and Trends in Anthropogenic Surface Emissions From Bottom-Up Inventories, Top-Down Estimates, and Emission Scenarios, Earths Future, 8, e2020EF001520, https://doi.org/10.1029/2020EF001520, 2020.

Elshorbany, Y. F., Kurtenbach, R., Wiesen, P. Lissi, E., Rubio, M., Villena, G., Gramsch, E., Rickard, A. R., Pilling, M. J., Kleffmann. J.: Oxidation capacity of the city air of Santiago, Chile, *Atmospheric Chemistry and Physics*, **9**, 2257-2273, 2009.

Elshorbany, Y. F, Barnes, I., Becker, K. H, Kleffmann, J., and Wiesen, P.: Sources and Cycling of Tropospheric Hydroxyl Radicals-An Overview, *Zeitschrift für Physikalische Chemie*, 224, 967-987, DOI:10.1524/zpch.2010.6136, 2010.

Elshorbany, Y. F., Kleffmann, J., Hofzumahaus, A., Kurtenbach, R., Wiesen, P., Dorn,H.-P., Schlosser, E., Brauers, T., Fuchs, H., Rohrer, F., Wahner, A., Kanaya, Y., Yoshino, A., Nishida, S., Kajii, Y., Martinez, M., Rudolf, M., Harder, H., Lelieveld, J., , Elste, T., Plass-Dülmer, C., Stange, G., and Berresheim, H.: HO_x Budgets during HOxComp: a Case Study of HO_x Chemistry under NO_x limited Conditions, J. Geophys. Res., 117, D03307, doi: 10.1029/2011JD017008, 2012.

Elshorbany, Y. F., Crutzen, P. J., Steil, B., Pozzer, A., Tost, H., and Lelieveld, J.: Global and regional impacts of HONO on the chemical composition of clouds and aerosols, Atmos. Chem. Phys., 14, 1167–1184, https://doi.org/10.5194/acp-14-1167-2014, 2014.

Elshorbany, Y. F.; Hannah C. Kapper; Jerald R. Ziemke;Scott A. Parr; (2021). The Status of Air Quality in the United States During the COVID-19 Pandemic: A Remote Sensing Perspective . Remote Sensing, doi:10.3390/rs13030369, 2021.

Fadnavis et al., 2024, in preparation.

Fehr, T., H. Höller, and H. Huntrieser (2004), Model study on production and transport of lightning-produced NOx in a EULINOX supercell storm, *J. Geophys. Res.*, *109*, D09102, doi:10.1029/2003JD003935.

Finney. D. L., R. M. Doherty, O. Wild, H. Huntrieser, H. C. Pumphrey, and A. M. Blyth (2014), Using cloud ice flux to parameterize large-scale lightning, *Atmos. Chem. Phys.*, 14, 12665–12682, www.atmos-chem-phys.net/14/12665/2014/ doi:10.5194/acp-14-12665-2014.

Finney, D. L., R. M. Doherty, O. Wild, P. J. Young, and A. Butler (2016), Response of lightning NO*x* emissions and ozone production to climate change: Insights from the Atmospheric Chemistry and Climate Model Intercomparison Project, *Geophys. Res. Lett.*, 43, 5492–5500, doi:10.1002/2016GL068825.

Finney, D. L., R. M. Doherty, O. Wild, D. S. Stevenson, I. A. MacKenzie, and A. M. Blyth (2018), A projected decrease in lightning under climate change, *Nature Climate Change*, 8, 210-213.

Fiore, A. M., Jacob, D. J., Field, B. D., Streets, D. G., Fernandes, S. D., and Jang, C.: Linking air pollution and climate change: The case for controlling methane, Geophys. Res. Lett., 29, 1919, doi:10.1029/2002GL015601, 2002.

Fiore, A. M., L. W. Horowitz, E. J. Dlugokencky, and J. J. West (2006), Impact of meteorology and emissions on methane trends, 1990–2004, *Geophys. Res. Lett.*, 33, L12809, doi:10.1029/2006GL026199.

Fisher, B. L., Lamsal, L. N., Fasnacht, Z., Oman, L. D., Joiner, J., Krotkov, N. A., ... & Yang, E. S.: Revised estimates of NO2 reductions during the COVID-19 lockdowns using updated TROPOMI NO2 retrievals and model simulations. Atmospheric Environment, 326, 120459, 2024.

Fleming, Z.L., Doherty, R.M., von Schneidemesser, E., Malley, C.S., Cooper, O.R., Pinto, J.P., Colette, A., Xu, X., Simpson, D., Schultz, M.G., Lefohn, A.S., Hamad, S., Moolla, R., Solberg, S. and Feng, Z., Tropospheric Ozone Assessment Report: Present-day ozone distribution and trends relevant to human health. 2018. Elem Sci Anth, 6(1), p.12. DOI: 10.1525/elementa.73.

Flynn, C. M., K. E. Pickering, J. H. Crawford, A. Weinheimer, K. L. Thornhill, C. Loughner, P. Lee, Variability of O_3 and NO_2 profile shapes during DISCOVER-AQ: Implications for satellite observations and comparisons to model-simulated profiles, *Atmos. Environ.*, 147, 133-156, 2016.

Fortems-Cheiney, A., Chevallier, F., Pison, I., Bousquet, P., Szopa, S., Deeter, M. N., and Clerbaux, C.: Ten years of CO emissions as seen from Measurements of Pollution in the Troposphere (MOPITT), J. Geophys. Res., 116, D05304, https://doi.org/10.1029/2010JD014416, 2011.

Fortems-Cheiney, A., Chevallier, F., Pison, I., Bousquet, P., Saunois, M., Szopa, S., Cressot, C., Kurosu, T. P., Chance, K., and Fried, A.: The formaldehyde budget as seen by a global-scale multi-constraint and multi-species inversion system, Atmos. Chem. Phys., 12, 6699–6721, https://doi.org/10.5194/acp-12-6699-2012, 2012.

Forster, P., T. Storelvmo, K. Armour, W. Collins, J.-L. Dufresne, D. Frame, D.J. Lunt, T. Mauritsen, M.D. Palmer, M. Watanabe, M. Wild, and H. Zhang, 2021: The Earth's Energy Budget, Climate Feedbacks, and Climate Sensitivity. In Climate Change 2021: The Physical Science Basis. Contribution of Working Group I to the Sixth Assessment Report of the Intergovernmental Panel on Climate Change [Masson-Delmotte, V., P. Zhai, A. Pirani, S.L. Connors, C. Péan, S. Berger, N. Caud, Y. Chen, L. Goldfarb, M.I. Gomis, M. Huang, K. Leitzell, E. Lonnoy, J.B.R. Matthews, T.K. Maycock, T. Waterfield, O. Yelekçi, R. Yu, and B. Zhou (eds.)]. Cambridge University Press, 923 Cambridge, United Kingdom and New York, NY, USA, pp. 923–1054, doi:10.1017/9781009157896.009, 2021.

Fullekrug, M. E. Williams, C. Price, S. Goodman, R. Holzworth, K. Virts, and D. Buechler (2022) Sidebar 2.1: Lightning, in State of the Climate: 2021, *Bull. Amer. Meteor. Soc*., 108, S79-S81, doi:10.1175/BAMS-D-22-0092.1

Fung, K. M., Val Martin, M., and Tai, A. P. K.: Modeling the interinfluence of fertilizer-induced NH3 emission, nitrogen deposition, and aerosol radiative effects using modified CESM2, Biogeosciences, 19, 1635–1655, https://doi.org/10.5194/bg-19-1635-2022, 2022.

Gaubert, B., Emmons, L. K., Raeder, K., Tilmes, S., Miyazaki, K., Arellano Jr., A. F., Elguindi, N., Granier, C., Tang, W., Barré, J., Worden, H. M., Buchholz, R. R., Edwards, D. P., Franke, P., Anderson, J. L., Saunois, M., Schroeder, J., Woo, J.-H., Simpson, I. J., Blake, D. R., Meinardi, S., Wennberg, P. O., Crounse, J., Teng, A., Kim, M., Dickerson, R. R., He, H., Ren, X., Pusede, S. E., and Diskin, G. S.: Correcting model biases of CO in East Asia: impact on oxidant distributions during KORUS-AQ, Atmos. Chem. Phys., 20, 14617–14647, https://doi.org/10.5194/acp-20-14617-2020, 2020.

Ghude, S.D., Van der A, R.J., Beig, G., Fadnavis, S., Polade, S.D.: Satellite derived trends in NO2 over the major global hotspot regions during the past decade and their inter-comparison. Environ. Pollut. 157, 1873–1878. https://doi.org/10.1016/j. envpol.2009.01.013, 2009.

Gaudel, A., Cooper, O.R., Ancellet, G., Barret, B., Boynard, A., Burrows, J.P., Clerbaux, C., Coheur, P.-F., Cuesta, J., Cuevas, E., Doniki, S., Dufour, G., Ebojie, F., Foret, G., Garcia, O., Granados Muños, M.J., Hannigan, J.W., Hase, F., Huang, G., Hassler, B., Hurtmans, D., Jaffe, D., Jones, N., Kalabokas, P., Kerridge, B., Kulawik, S.S., Latter,

B., Leblanc, T., Le Flochmoën, E., Lin, W., Liu, J., Liu, X., Mahieu, E., McClure-
Begley, A., Neu, J.L., Osman, M., Palm, M., Petetin, H., Petropavlovskikh, I., Querel,
R., Rahpoe, N., Rozanov, A., Schultz, M.G., Schwab, J., Siddans, R., Smale, D.,
Steinbacher, M., Tanimoto, H., Tarasick, D.W., Thouret, V., Thompson, A.M.,
Trickl, T., Weatherhead, E., Wespes, C., Worden, H.M., Vigouroux, C., Xu, X.,
Zeng, G. and Ziemke, J., Tropospheric Ozone Assessment Report: Present-day
distribution and trends of tropospheric ozone relevant to climate and global
atmospheric chemistry model evaluation, 2018. Elem Sci Anth, 6(1), p.39. DOI:
10.1525/elementa.291, 2018.

Granier, C., Bessagnet, B., Bond, T., D'Angiola, A., Denier van der Gon, H., Frost, G. J., ...
& van Vuuren, D. P.: Evolution of anthropogenic and biomass burning emissions of
air pollutants at global and regional scales during the 1980–2010 period. *Climatic
change, 109*, 163-190, 2011.

Gelaro, Ronald, et al. "The modern-era retrospective analysis for research and applications,
version 2 (MERRA-2)." *Journal of climate* 30.14 (2017): 5419-5454.

Gödde and Conrad: https://doi.org/10.1007/s003740000247

Grewe, V., Brunner, D., Dameris, M., Grenfell, J. L., Hein, R., Shindell, D., & Staehelin, J.
(2001), Origin and variability of upper tropospheric nitrogen oxides and ozone at
northern mid-latitudes, *Atmos. Env.*, 35, 3421-3433.

Griffiths, P. T., Murray, L. T., Zeng, G., Shin, Y. M., Abraham, N. L., Archibald, A. T.,
Deushi, M., Emmons, L. K., Galbally, I. E., Hassler, B., Horowitz, L. W., Keeble, J.,
Liu, J., Moeini, O., Naik, V., O'Connor, F. M., Oshima, N., Tarasick, D., Tilmes, S.,
Turnock, S. T., Wild, O., Young, P. J., and Zanis, P.: Tropospheric ozone in CMIP6
simulations, Atmos. Chem. Phys., 21, 4187–4218, https://doi.org/10.5194/acp-21-
4187-2021, 2021.

Gulev, S.K., P.W. Thorne, J. Ahn, F.J. Dentener, C.M. Domingues, S. Gerland, D. Gong,
D.S. Kaufman, H.C. Nnamchi, J. Quaas, J.A. Rivera, S. Sathyendranath, S.L. Smith,
B. Trewin, K. von Schuckmann, and R.S. Vose: Changing State of the Climate
System. In Climate Change 2021: The Physical Science Basis. Contribution of
Working Group I to the Sixth Assessment Report of the Intergovernmental Panel on
Climate Change [Masson-Delmotte, V., P. Zhai, A. Pirani, S.L. Connors, C. Péan, S.
Berger, N. Caud, Y. Chen, L. Goldfarb, M.I. Gomis, M. Huang, K. Leitzell, E.
Lonnoy, J.B.R. Matthews, T.K. Maycock, T. Waterfield, O. Yelekçi, R. Yu, and B.
Zhou (eds.)]. Cambridge University Press, Cambridge, United Kingdom and New
York, NY, USA, pp. 287–422, doi: 10.1017/9781009157896.004, 2021.

Hoor, P., Borken-Kleefeld, J., Caro, D., Dessens, O., Endresen, O., Gauss, M., Grewe, V.,
Hauglustaine, D., Isaksen, I. S. A., Jöckel, P., Lelieveld, J., Myhre, G., Meijer, E.,
Olivie, D., Prather, M., Schnadt Poberaj, C., Shine, K. P., Staehelin, J., Tang, Q., van
Aardenne, J., van Velthoven, P., and Sausen, R.: The impact of traffic emissions on
atmospheric ozone and OH: results from QUANTIFY, Atmos. Chem. Phys., 9, 3113–
3136, https://doi.org/10.5194/acp-9-3113-2009, 2009.

Holzworth, R. H., Brundell, J. B., McCarthy, M. P., Jacobson, A. R., Rodger, C. J., &
Anderson, T. S. (2021). Lightning in the Arctic. *Geophysical Research Letters*, 48,

e2020GL091366. https://doi.org/10.1029/2020GL091366.

Hubert, D., Heue, K.-P., Lambert, J.-C., Verhoelst, T., Allaart, M., Compernolle, S., Cullis, P. D., Dehn, A., Félix, C., Johnson, B. J., Keppens, A., Kollonige, D. E., Lerot, C., Loyola, D., Maata, M., Mitro, S., Mohamad, M., Piters, A., Romahn, F., Selkirk, H. B., da Silva, F. R., Stauffer, R. M., Thompson, A. M., Veefkind, J. P., Vömel, H., Witte, J. C., and Zehner, C.: TROPOMI tropospheric ozone column data: geophysical assessment and comparison to ozonesondes, GOME-2B and OMI, Atmos Meas Tech, 14, 7405–7433, https://doi.org/10.5194/amt-14-7405-2021, 2021.

Hudman et al., (2012) www.atmos-chem-phys.net/12/7779/2012/

Huntrieser, H., U. Schumann, H. Schlager, H. Höller, A. Giez, H.-D. Betz, D. Brunner, C. Forster, O. Pinto Jr., and R. Calheiros (2008), Lightning activity in Brazilian thunderstorms during TROCCINOX: Implications for NOx production, *Atmos. Chem. Phys.*, *8*, 21–953.

Huntrieser, H., H. Schlager, M. Lichtenstern, P. Stock, T. Hamburger, H. Hoeller, K. Schmidt, H.-D. Betz, A. Ulanovsky, and F. Ravegnani (2011) Mesoscale convective systems observed during AMMA and their impact on the NOx and O3 budget over West Africa, Atmos. Chem. Phys., 11, 2503–2536, www.atmos-chem-phys.net/11/2503/2011, doi:10.5194/acp-11-2503-2011

Ichoku, C., & Ellison, L.: Global top-down smoke-aerosol emissions estimation using satellite fire radiative power measurements. *Atmospheric Chemistry and Physics*, *14*(13), 6643-6667, 2014.

IPCC, AR5, chrome-extension://efaidnbmnnnibpcajpcglclefindmkaj/https://www.ipcc.ch/site/assets/uploads/2018/03/TAR-06.pdf, 2018.

Isaksen, I.S.A.; Berntsen, T.K.; Dalsøren, S.B.; Eleftheratos, K.; Orsolini, Y.; Rognerud, B.; Stordal, F.; Søvde, O.A.; Zerefos, C.; Holmes, C.D. Atmospheric Ozone and Methane in a Changing Climate. Atmosphere, 5, 518-535. https://doi.org/10.3390/atmos5030518, 2014.

Janssens-Maenhout, G., Pagliari, V., Guizzardi, D., & Muntean, M.: Global emission inventories in the emission database for global atmospheric research (EDGAR)– Manual (I). *Gridding: EDGAR emissions distribution on global gridmaps, Publications Office of the European Union, Luxembourg, 775, 2013.*

Jin, X., Fiore, A., Boersma, K. F., Smedt, I. D., and Valin, L.: Inferring Changes in Summertime Surface Ozone–NOx –VOC Chemistry over U.S. Urban Areas from Two Decades of Satellite and Ground-Based Observations, Environmental Science Technology, 54, 6518–6529, https://doi.org/10.1021/acs.est.9b07785, 2020

J. Jung, Y. Choi, S. Mousavinezhad, D. Kang, J. Park, A. Pouyaei, *et al.:* Changes in the ozone chemical regime over the contiguous United States inferred by the inversion of NOx and VOC emissions using satellite observation, Atmos. Res., 270, 106076, https://doi.org/10.1016/j.atmosres.2022.106076, 2022

Kang, D., K. Foley, R. Mathur, S. Roselle, K. Pickering, and D. Allen, Lightning NO$_X$ Production in CMAQ Part II – Performance Evaluations, *Geosci. Model Devel.*, 12, 4409–4424, https://doi.org/10.5194/gmd-12-4409-2019, 2019.

Kaynak, B., Hu, Y., Martin, R. V., Russell, A. G., Choi, Y., & Wang, Y. (2008). The effect of lightning NOx production on surface ozone in the continental United States. Atmospheric Chemistry and Physics, 8, 5151–5159.

Koven et al., (2013) https://bg.copernicus.org/articles/10/7109/2013/

Kitagawa, N., (1989) Long-term variations in thunder-day frequencies in Japan. J. Geophys. Res., 94, 13 183–13 189, https://doi.org/10.1029/JD094iD11p13183.

Koehler, T. L. (2020) Cloud-to-Ground Lightning Flash Density and Thunderstorm Day Distributions over the Contiguous United States Derived from NLDN Measurements: 1993–2018, *Mon. Weather Rev.*, DOI: 10.1175/MWR-D-19-0211.1

Kopacz, M., Jacob, D. J., Fisher, J. A., Logan, J. A., Zhang, L., Megretskaia, I. A., Yantosca, R. M., Singh, K., Henze, D. K., Burrows, J. P., Buchwitz, M., Khlystova, I., McMillan, W. W., Gille, J. C., Edwards, D. P., Eldering, A., Thouret, V., and Nedelec, P.: Global estimates of CO sources with high resolution by adjoint inversion of multiple satellite datasets (MOPITT, AIRS, SCIAMACHY, TES), Atmos. Chem. Phys., 10, 855–876, https://doi.org/10.5194/acp-10-855-2010, 2010.

Koshak, W., Peterson, H., Biazar, A., Khan, M., & Wang, L. (2014). The NASA Lightning Nitrogen Oxides Model (LNOM): application to air quality modeling. *Atmospheric Research*, *135*, 363-369.

Koshak, W.J., Cummins, K.L., Buechler, D.E., Vant-Hull, B., Blakeslee, R.J., Williams, E.R. and Peterson, H.S. (2015) Variability of CONUS lightning in 2003–12 and associated impacts. *Journal of Applied Meteorology and Climatology*, **54**, 15– 41,

https://doi.org/10.1175/JAMC-D-14-0072.1.

Krizan, P. and Lastovicka, J.: Trends in positive and negative ozone laminae in the Northern Hemisphere, Journal of Geophysical Research: Atmospheres, 110, https://doi.org/https://doi.org/10.1029/2004JD005477, 2005.

Labow, G. J., Ziemke, J. R., McPeters, R. D., Haffner, D. P., and Bhartia, P. K.: A total ozone-dependent ozone profile climatology based on ozonesondes and Aura MLS data, Journal of Geophysical Research: Atmospheres, 120, 2537–2545, https://doi.org/10.1002/2014JD022634, 2015.

Labrador, L. J., Kuhlmann, R. V., and Lawrence, M. G. (2005), The effects of lightning-produced NOx and its vertical distribution on atmospheric chemistry: sensitivity simulations with MATCH-MPIC, *Atmos. Chem. Phys.*, 5, 1815-1834.

Lacis, A. A., Wuebbles, D. J., and Logan, J. A. (1990), Radiative forcing of climate by changes in the vertical distribution of ozone, *J. Geophys. Res.*, 95, 9971-9982.

Lamsal, L. N, Duncan, B. N., Yoshida, Y., Krotkov, N. A., Pickering, K. E., Streets, D. G., Zifeng Lu, Z.: U.S. NO2 trends (2005–2013): EPA Air Quality System (AQS) data versus improved observations from the Ozone Monitoring Instrument (OMI), Atmospheric Environment, https://doi.org/10.1016/j.atmosenv.2015.03.055, 2015.

Lapierre, J. L., Laughner, J. L., Geddes, J. A., Koshak, W. J., Cohen, R. C., Pusede, S. E.
(2020), Observing U.S. regional variability in lightning NO_2 production rates, J.
Geophys. Res., 125 (5), https:/doi.org/10.1029/2019JD031362.

Lavigne, T., C. Liu, and N. Liu, (2019) How does the trend in thunder days relate to
the variation of lightning flash density? J. Geophys. Res. Atmos., 124, 4955–
4974, https://doi.org/10.1029/2018JD029920

Lefohn, AS, Malley, CS, Smith, L, Wells, B, Hazucha, M, Simon, H, Naik, V, Mills, G,
Schultz, MG, Paoletti, E, De Marco, A, Xu, X, Zhang, L, Wang, T, Neufeld, HS,
Musselman, RC, Tarasick, D, Brauer, M, Feng, Z, Tang, H, Kobayashi, K, Sicard, P,
Solberg, S and Gerosa, G, 2018. Tropospheric ozone assessment report: Global ozone
metrics for climate change, human health, and crop/ecosystem research. Elem Sci
Anth, 6: 28. DOI: 10.1525/elementa.279.

Lelieveld, J.; P. J. Crutzen (1991). The role of clouds in tropospheric photochemistry. , 12(3),
229–267. doi:10.1007/bf00048075

Liaskos, C. E., Allen, D. J., & Pickering, K. E. (2015), Sensitivity of tropical tropospheric
composition to lightning NOx production as determined by replay simulations with
GEOS-5, *J. Geophys. Res. Atmos*., 120, 8512–8534, doi:10.1002/2014JD022987.

Liu, J., Jose M. Rodriguez, Luke D. Oman, Anne R. Douglass, Mark A. Olsen, Lu
Hu, Stratospheric impact on the Northern Hemisphere winter and spring ozone
interannual variability in the troposphere, Atmospheric Chemistry and Physics,
10.5194/acp-20-6417-2020, **20**, 11, 6417-6433, 2020.

Liu, Y., Williams, E. R., Guha, A., & Said, R. (2021), How will lightning change during the
pollution-reduced COVID-19 pandemic period? A data study on the global lightning
activity, AGU Fall Meeting 2021.

Liu et al., (2021) https://acp.copernicus.org/articles/21/17743/2021/

Liu, J., Strode, S. A., Liang, Q., Oman, L.D., Colarco, P. R., Fleming, E. L., et al. (2022).
Change in tropospheric ozone in the recent decades and its contribution to global total
ozone. Journal of Geophysical Research: Atmospheres, 127, e2022JD037170.
https://doi.org/10.1029/2022JD037170

Li et al. (2011) https://doi.org/10.1016/j.chnaes.2010.11.006

Luecken, D. J.; Napelenok, S. L.; Strum, M.; Scheffe, R.; Phillips, S. Sensitivity of ambient
atmospheric formaldehyde and ozone to precursor species and source types across the
united states. *Environ. Sci. Technol.*, *52*, 4668– 4675, DOI: 10.1021/acs.est.7b05509,
2018

Marais, E. A., Jacob, D. J., Choi, S., Joiner, J., Belmonte-Rivas, M., Cohen, R. C., et al.
(2018). Nitrogen oxides in the global upper troposphere: interpreting cloud-sliced
NO_2 observations from the OMI satellite instrument, *Atmospheric Chemistry and
Physics*, https://doi.org/10.5194/acp-18-17017-2018

Marais, E. A., Jacob, D. J., Kurosu, T. P., Chance, K., Murphy, J. G., Reeves, C., Mills, G.,
Casadio, S., Millet, D. B., Barkley, M. P., Paulot, F., and Mao, J.: Isoprene emissions
in Africa inferred from OMI observations of formaldehyde columns, Atmos. Chem.
Phys., 12, 6219–6235, https://doi.org/10.5194/acp-12-6219-2012, 2012.

Martin, R. V., Sauvage, B., Folkins, I., Sioris, C. E., Boone, Bernath, C. P., & Ziemke, J. (2007), Space-based constraints on the production of nitric oxide by lightning, *J. Geophys. Res.*, 112, D09309, doi:10.1029/2006JD007831.

Matandirotya, N.R., Burger, R. An assessment of NO_2 atmospheric air pollution over three cities in South Africa during 2020 COVID-19 pandemic. *Air Qual Atmos Health* **16**, 263–276 (2023). https://doi.org/10.1007/s11869-022-01271-3

McDuffie, E. E., Smith, S. J., O'Rourke, P., Tibrewal, K., Venkataraman, C., Marais, E. A., Zheng, B., Crippa, M., Brauer, M., and Martin, R. V.: A global anthropogenic emission inventory of atmospheric pollutants from sector- and fuel-specific sources (1970–2017): an application of the Community Emissions Data System (CEDS), Earth Syst. Sci. Data, 12, 3413–3442, https://doi.org/10.5194/essd-12-3413-2020, 2020.

Meng, L., Liu, J., Tarasick, D. W., Randel, W. J., Steiner, A. K., Wilhelmsen, H., Wang, L., and Haimberger, L. (2021). Continuous rise of the tropopause in the Northern Hemisphere over 1980–2020. Science Advances, https://doi.org/10.1126/sciadv.abi8065, 2021.

Mills G, Pleijel H, Malley CS, Sinha B, Cooper OR, Schultz MG, Neufeld HS, Simpson D, Sharps K, Feng Z, Gerosa G, Harmens H, Kobayashi K, Saxena P, Paoletti E, Sinha V, Xu X,. Tropospheric Ozone Assessment Report: Present-day tropospheric ozone distribution and trends relevant to vegetation. Elem Sci Anth. 2018;6(1):47. DOI: 10.1525/elementa.302.

Miyazaki, K., H. J. Eskes, K. Sudo, and C. Zhang, (2014) Global lightning NO_x production estimated by an assimilation of multiple satellite data sets, *Atmos. Chem Phys.*, 14, 3277–3305, www.atmos-chem-phys.net/14/3277/2014/doi:10.5194/acp-14-3277-2014.

Miyazaki, K., Bowman, K., Sekiya, T., Eskes, H., Boersma, F., Worden, H., Livesey, N., Payne, V. H., Sudo, K., Kanaya, Y., Takigawa, M., and Ogochi, K.: Updated tropospheric chemistry reanalysis and emission estimates, TCR-2, for 2005–2018, Earth Syst. Sci. Data, 12, 2223–2259, https://doi.org/10.5194/essd-12-2223-2020, 2020.

McPeters, R. D. and Labow, G. J.: Climatology 2011: An MLS and sonde derived ozone climatology for satellite retrieval algorithms, Journal of Geophysical Research: Atmospheres, 117, n/a-n/a, https://doi.org/10.1029/2011JD017006, 2012.

Molod, A., Takacs, L., Suarez, M., and Bacmeister, J.: Development of the GEOS-5 atmospheric general circulation model: evolution from MERRA to MERRA2, Geosci. Model Dev., 8, 1339–1356, https://doi.org/10.5194/gmd-8-1339-2015, 2015.

Murray, L. T. (2018), An uncertain future for lightning, *Nature Climate Change*, 8, 191-192.

Murray, L. T. (2016), Lightning NO_x and Impacts on Air Quality, Curr Pollution Rep (2016) 2:115–133, DOI 10.1007/s40726-016-0031-7

Murray, L. T., D. J. Jacob, J. A. Logan, R. C. Hudman, and W. J. Koshak (2012), Optimized regional and interannual variability of lightning in a global chemical transport model constrained by LIS/OTD satellite data, *J. Geophys. Res.*, 117, D20307, doi:10.1029/2012JD017934.

Nault, B. A., Garland, C., Wooldridge, J. L., Brune, W. H., Campuzano-Jost, P., Crounse, J. D., et al. (2016). Observational Constraints on the Oxidation of NO_x in the Upper Troposphere, *The Journal of Physical Chemistry A*, *120* (9), 1468-1478, doi: 10.1021/acs.jpca.5b07824

Nault, B. A., Laughner, J. L., Wooldridge, P. J., Crounse, J. D., Dibb, J., Diskin, et al. (2017). Lightning NO_x emissions: reconciling measured and modeled estimates with updated NO_x chemistry. *Geophysical Research Letters*, 44, 9479–9488.

Newton, R., Vaughan, G., Ricketts, H. M. A., Pan, L. L., Weinheimer, A. J., and Chemel, C.: Ozonesonde profiles from the West Pacific Warm Pool: measurements and validation, Atmos Chem Phys, 16, 619–634, https://doi.org/10.5194/acp-16-619-2016, 2016.

Nielsen, J. Eric, et al. "Chemical mechanisms and their applications in the Goddard Earth Observing System (GEOS) earth system model." *Journal of Advances in Modeling Earth Systems* 9.8 (2017): 3019-3044.

Nussbaumer, C. M., Fischer, H., Lelieveld, J., and Pozzer, A.: What controls ozone sensitivity in the upper tropical troposphere?, Atmos. Chem. Phys., 23, 12651–12669, https://doi.org/10.5194/acp-23-12651-2023, 2023.

Oleribe OO, Suliman AAA, Taylor-Robinson SD, Corrah T. Possible Reasons Why Sub-Saharan Africa Experienced a Less Severe COVID-19 Pandemic in 2020. *J Multidiscip Healthc*. 2021;14:3267-3271, https://doi.org/10.2147/JMDH.S331847, 2021.

Oltmans, SJ, Lefohn, AS, Shadwick, D, Harris, JM, Scheel, HE, et al.: Recent tropospheric ozone changes — A pattern dominated by slow or no growth, *Atmos. Environ*, 2013.

Orbe, C., Oman, L. D., Strahan, S. E., Waugh, D. W., Pawson, S., Takacs, L. L., and Molod, A. M. (2017). Large-scale atmospheric transport in GEOS replay simulations. Journal of Advances in Modeling Earth Systems, 9, 2545–2560. https://doi.org/10.1002/2017MS001053

Ott, L. E., K. E. Pickering, G. L. Stenchikov, H. Huntrieser, and U. Schumann (2007), Effects of lightning NOx production during the 21 July European Lightning Nitrogen Oxides Project storm studied with a three-dimensional cloud-scale chemical transport model, *J. Geophys. Res.*, *112*, D05307, doi:10.1029/2006JD007365.

Ott, L. E., K. E. Pickering, G. L. Stenchikov, D. J. Allen, A. J. DeCaria, B. Ridley, R.-F. Lin, S. Lang, and W.-K. Tao (2010), Production of lightning NOx and its vertical distribution calculated from three-dimensional cloud-scale chemical transport model simulations, *J. Geophys. Res.*, *115*, D04301,doi:10.1029/2009JD011880Philipona, R., C. Mears, M. Fujiwara, P. Jeannet, P. Thorne, G. Bodeker, L. Haimberger, M. Hervo, C. Popp, G. Romanens, W. Steinbrecht, R. Stubi, R. Van Malderen, adiosondes show that after decades of cooling, the lower stratosphere is now warming. J. Geophys. Res. Atmos. 123, 12509–12522 (2018).

Pickering, K. E, A. M. Thompson, R. R. Dickerson, W. T. Luke, D. P. McNamara, J. P. Greenberg, and P. R. Zimmerman, Model calculations of tropospheric ozone production potential following observed convective events, *J. Geophys. Res.*, 95:14,049-14,062, 1990.

Pickering, K. E., Y. Wang, W.-K. Tao, C. Price, and J.-F. Mueller, Vertical distributions of lightning NO_x for use in regional and global chemical transport models, *J. Geophys. Res.*, 103: 31,203-31,216, 1998.

Pickering, K. E., E. Bucsela, D. Allen, A. Ring, R. Holzworth, and N. Krotkov (2016), Estimates of lightning NO*x* production based on OMI NO_2 observations over the Gulf of Mexico, *J. Geophys. Res. Atmos.*, 121, doi:10.1002/2015JD024179.

Pickering, K. E., Y. Li, K. A. Cummings, M. C. Barth, D. J. Allen, E. Bruning, (2023) Lightning NO_x in the May 29-30, 2012 Deep Convective Clouds and Chemistry (DC3) Severe Storm and its Downwind Chemical Consequences, *J. Geophys. Res.-Atmos.*, to be submitted.

Pinto, O., Jr., K. P. Naccarato, and I. R. C. A. Pinto, 2013: Thunderstorm incidence in southeastern Brazil estimated from different data sources. Ann. Geophys., 31, 1213–1219, https://doi.org/10.5194/angeo-31-1213-2013.

Prodromos Zanis, Dimitris Akritidis, Steven Turnock, Vaishali Naik, Sophie Szopa, Aristeidis K Georgoulias, Susanne E Bauer, Makoto Deushi, Larry W Horowitz, James Keeble, Climate change penalty and benefit on surface ozone: a global perspective based on CMIP6 earth system models, Environmental Research Letters, Volume 17, Number 2, Environmental Research Letters, Volume 17, Number 2, DOI: https://doi.org/10.1088/1748-9326/ac4a34.

Pollack, I. B., C. R. Homeyer, T. B. Ryerson, K. C. Aikin, J. Peischl, E. C. Apel, T. Campos, F. Flocke, R. S. Hornbrook, D. J. Knapp, et al. (2016), Airborne quantification of upper tropospheric NO*x* production from lightning in deep convective storms over the United States Great Plains, *J. Geophys. Res. Atmos.*, 121, 2002–2028, doi:10.1002/2015JD023941.

Prather, M. J. and D. J. Jacob (1997) A persistent imbalance in HO_x and NO_x photochemistry of
the upper troposphere driven by deep tropical convection, *Geophys. Res. Lett.*, 24, 3189 – 3192.

Price, C., J. Penner, and M. Prather (1997), NO_x from lightning 1. Global distribution based on lightning physics, *J. Geophys. Res.*, *102* (D5), 5929-5941.

Price, C. G., (2013) Lightning Applications in Weather and Climate Research, *Surv. Geophys*. (2013) 34:755–767, DOI 10.1007/s10712-012-9218-7

Putero, D., Cristofanelli, P., Chang, K.-L., Dufour, G., Beachley, G., Couret, C., Effertz, P., Jaffe, D. A., Kubistin, D., Lynch, J., Petropavlovskikh, I., Puchalski, M., Sharac, T., Sive, B. C., Steinbacher, M., Torres, C., and Cooper, O. R.: Fingerprints of the COVID-19 economic downturn and recovery on ozone anomalies at high-elevation sites in North America and western Europe, Atmos. Chem. Phys., 23, 15693–15709, https://doi.org/10.5194/acp-23-15693-2023, 2023.

Qie, K., Qie, X., & Tian, W. (2021), Increasing trend of lightning activity in the South Asian region, Science Bulletin, 66 (1), 78-84.

Qie, K., Tian, W., Wang, W., Wu, X., Yuan, T., Tian, H., Luo, J., Zhang, R., & Want, T. Regional trends of lightning activity in the tropics and subtropics, Atmos. Res., 242 (2020), Article 104960, 10.1016/j.atmosres.2020.104960

Randel, W. J., L. Polvani, F. Wu, D. E. Kinnison, C.-Z. Zou, C. Mears, Troposphere stratosphere temperature trends derived from satellite data compared with ensemble simulations from WACCM. J. Geophys. Res. Atmos. 122, 9651–9667 (2017).

Ren, X., J. R. Olson, J. H. Crawford, W. H. Brune, J. Mao, R. B. Long, G. Chen, M. A. Avery, G. W. Sachse, J. D. Barrick, G. S. Diskin, L. G. Huey, Alan Fried, Ronald C. Cohen, Brian Heikes, Paul Wennberg, Hanwant B. Singh, Donald R. Blake, Richard E. Shetter,(2008) HOx Chemistry during INTEX–A 2004: Observation, Model Calculations and comparison with previous studies, *J. Geophys. Res.*, 113, D05310, doi:10.1029/2007JD009166.

Ridley, B., Ott, L., Pickering, K., Emmons, L., Montzka, D., Weinheimer, A., et al. (2004), Florida thunderstorms: A faucet of reactive nitrogen to the upper troposphere, J. Geophys. Res., 109 (D17), 10.1029/2004JD004769.

Romps, D. M., Seeley, J. T., Vollaro, D., & Molinar, J. (2014), Projected increase in lightning strikes in the United States due to global warming, *Science*, 851-854.

Romps, D. M., Charn, A. B., Holzworth, R. H., Lawrence, W. E.,Molinari, J., & Vollaro, D. (2018). CAPE times P explains lightning over land but not the land-ocean contrast. *Geophysical Research Letters*, *45*, 12,623–12,630. https://doi.org/10.1029/2018GL080267

Romps, D. M. (2019). Evaluating the future of lightning in cloud-resolving models. *Geophysical Research Letters*, *46,* https://doi.org/10.1029/2019GL085748

Sanap, S. D. (2021) Global and regional variations in aerosol loading during COVID-19 imposed lockdown, *Atmos. Environ.*, 246, https://doi.org/10.1016/j.atmosenv.2020.118132.

Sauvage, B., R. V. Martin, A. van Donkelaar, and J. R. Ziemke (2007) Quantification of the factors controlling tropical tropospheric ozone and the South Atlantic maximum, *J. Geophys. Res.*, 112, D11309, doi:10.1029/2006JD008008.

Sanap, S. D. (2021) Global and regional variations in aerosol loading during COVID-19 imposed lockdown, *Atmos. Environ.*, 246, https://doi.org/10.1016/j.atmosenv.2020.118132.

Sauvage, B., R. V. Martin, A. van Donkelaar, and J. R. Ziemke (2007) Quantification of the factors controlling tropical tropospheric ozone and the South Atlantic maximum, *J. Geophys. Res.*, 112, D11309, doi:10.1029/2006JD008008.

Sanap, S. D. (2021) Global and regional variations in aerosol loading during COVID-19 imposed lockdown, *Atmos. Environ.*, 246, https://doi.org/10.1016/j.atmosenv.2020.118132.

Saunois, M., R. Stavert, A., Poulter, B., Bousquet, P., G. Canadell, J., B. Jackson, R., A. Raymond, P., J. Dlugokencky, E., Houweling, S., K. Patra, P., Ciais, P., K. Arora, V., Bastviken, D., Bergamaschi, P., R. Blake, D., Brailsford, G., Bruhwiler, L., M. Carlson, K., Carrol, M., Castaldi, S., Chandra, N., Crevoisier, C., M. Crill, P., Covey, K., L. Curry, C., Etiope, G., Frankenberg, C., Gedney, N., I. Hegglin, M., Höglund-Isaksson, L., Hugelius, G., Ishizawa, M., Ito, A., Janssens-Maenhout, G., M. Jensen,

K., Joos, F., Kleinen, T., B. Krummel, P., L. Langenfelds, R., G. Laruelle, G., Liu, L., MacHida, T., Maksyutov, S., C. McDonald, K., McNorton, J., A. Miller, P., R. Melton, J., Morino, I., Müller, J., Murguia-Flores, F., Naik, V., Niwa, Y., Noce, S., O'Doherty, S., J. Parker, R., Peng, C., Peng, S., P. Peters, G., Prigent, C., Prinn, R., Ramonet, M., Regnier, P., J. Riley, W., A. Rosentreter, J., Segers, A., J. Simpson, I., Shi, H., J. Smith, S., Paul Steele, L., F. Thornton, B., Tian, H., Tohjima, Y., N. Tubiello, F., Tsuruta, A., Viovy, N., Voulgarakis, A., S. Weber, T., Van Weele, M., R. Van Der Werf, G., F. Weiss, R., Worthy, D., Wunch, D., Yin, Y., Yoshida, Y., Zhang, W., Zhang, Z., Zhao, Y., Zheng, B., Zhu, Q., Zhu, Q., and Zhuang, Q.: The global methane budget 2000-2017, Earth Syst Sci Data, 12, https://doi.org/10.5194/essd-12-1561-2020, 2020.

Sauvage, B., R. V. Martin, A. van Donkelaar, and J. R. Ziemke (2007) Quantification of the factors controlling tropical tropospheric ozone and the South Atlantic maximum, *J. Geophys. Res.*, 112, D11309, doi:10.1029/2006JD008008.

Schumann, U., and H. Huntrieser (2007), The global lightning-induced nitrogen oxides source, *Atmos. Chem. Phys.*, 7, 3823-3907.

Seguel, R. J., Castillo, L., Opazo, C., Rojas, N. Y., Nogueira, T., Cazorla, M., Gavidia-Calderón, M., Gallardo, L., Garreaud, R., Carrasco-Escaff, T., and Elshorbany, Y.: Changes in South American Surface Ozone Trends: Exploring the Influences of Precursors and Extreme Events, EGUsphere [preprint], https://doi.org/10.5194/egusphere-2024-328, 2024.

Sen, P (1968). Estimated of the regression coefficient based on Kendall's Tau. J Am Stat Assoc 39:1379-1389

Shi, Z., H. Wang, Y. Tan, L. Li, C. Li, (2020) Influence of aerosols on lightning activities in central eastern parts of China, *Atmos Sci Lett.*, 21:e957, https://doi.org/10.1002/asl.957.

Sokhi, R. S., Singh, V., Querol, X., Finardi, S., Targino, A. C., Andrade, M. de F., Pavlovic, R., Garland, R. M., Massagué, J., Kong, S., Baklanov, A., Ren, L., Tarasova, O., Carmichael, G., Peuch, V. H., Anand, V., Arbilla, G., Badali, K., Beig, G., Belalcazar, L. C., Bolignano, A., Brimblecombe, P., Camacho, P., Casallas, A., Charland, J. P., Choi, J., Chourdakis, E., Coll, I., Collins, M., Cyrys, J., da Silva, C. M., Di Giosa, A. D., Di Leo, A., Ferro, C., Gavidia-Calderon, M., Gayen, A., Ginzburg, A., Godefroy, F., Gonzalez, Y. A., Guevara-Luna, M., Haque, S. M., Havenga, H., Herod, D., Hõrrak, U., Hussein, T., Ibarra, S., Jaimes, M., Kaasik, M., Khaiwal, R., Kim, J., Kousa, A., Kukkonen, J., Kulmala, M., Kuula, J., La Violette, N., Lanzani, G., Liu, X., MacDougall, S., Manseau, P. M., Marchegiani, G., McDonald, B., Mishra, S. V., Molina, L. T., Mooibroek, D., Mor, S., Moussiopoulos, N., Murena, F., Niemi, J. V., Noe, S., Nogueira, T., Norman, M., Pérez-Camaño, J. L., Petäjä, T., Piketh, S., Rathod, A., Reid, K., Retama, A., Rivera, O., Rojas, N. Y., Rojas-Quincho, J. P., San José, R., Sánchez, O., Seguel, R. J., Sillanpää, S., Su, Y., Tapper, N., Terrazas, A., Timonen, H., Toscano, D., Tsegas, G., Velders, G. J. M., Vlachokostas, C., von Schneidemesser, E., VPM, R., Yadav, R., Zalakeviciute, R., and Zavala, M.: A global observational analysis to understand changes in air quality during exceptionally low anthropogenic emission conditions, Environ Int, 157, https://doi.org/10.1016/j.envint.2021.106818, 2021.

Souri, A. H., Johnson, M. S., Wolfe, G. M., Crawford, J. H., Fried, A., Wisthaler, A., Brune, W. H., Blake, D. R., Weinheimer, A. J., Verhoelst, T., Compernolle, S., Pinardi, G., Vigouroux, C., Langerock, B., Choi, S., Lamsal, L., Zhu, L., Sun, S., Cohen, R. C., Min, K.-E., Cho, C., Philip, S., Liu, X., and Chance, K.: Characterization of errors in satellite-based HCHONO2 tropospheric column ratios with respect to chemistry, column-to-PBL translation, spatial representation, and retrieval uncertainties, Atmospheric Chemistry and Physics, 23, 1963–1986, https://doi.org/10.5194/acp-23-1963-2023, 2023

Stauffer, R. M., Thompson, A. M., Kollonige, D., Tarasick, D., Van Malderen, R., Smit, H. G. J., Vömel, H., Morris, G., Johnson, B. J., Cullis, P., and et al.: An Examination of the Recent Stability of Ozonesonde Global Network Data, Earth and Space Science Open Archive, 48, https://doi.org/10.1002/essoar.10511590.1, 2022.

Steinbrecht, W., Claude, H., Köhler, U., and Hoinka, K. P.: Correlations between tropopause height and total ozone: Implications for long-term changes, J. Geophys. Res., 103, 19183–19192, https://doi.org/10.1029/98JD01929, 1998.

Steinbrecht, W., Kubistin, D., Plass-Dülmer, C., Davies, J., Tarasick, D. W., von der Gathen, P., et al.: COVID-19 crisis reduces free tropospheric ozone across the Northern Hemisphere. *Geophysical Research Letters*, 48, e2020GL091987. https://doi.org/10.1029/2020GL091987, 2021

Steiner, A. K., F. Ladst.dter, W. J. Randel, A. C. Maycock, Q. Fu, C. Claud, H. Gleisner, L. Haimberger, S. -P. Ho, P. Keckhut, T. Leblanc, C. Mears, L. M. Polvani, B. D. Santer, T. Schmidt, V. Sofieva, R. Wing, C. -Z. Zou, Observed temperature changes in the troposphere and stratosphere from 1979 to 2018. J. Climate 33, 8165–8194 (2020).

Stohl, A., Bonasoni, P., Cristofanelli, P., Collins, W., Feichter, J., Frank, A., Forster, C., Gerasopoulos, E., Gäggeler, H., James, P., Kentarchos, T., Kromp-Kolb, H., Krüger, B., Land, C., Meloen, J., Papayannis, A., Priller, A., Seibert, P., Sprenger, M., Roelofs, G. J., Scheel, H. E., Schnabel, C., Siegmund, P., Tobler, L., Trickl, T., Wernli, H., Wirth, V., Zanis, P., and Zerefos, C.: Stratosphere-troposphere exchange: A review, and what we have learned from STACCATO, J. Geophys. Res., 108, 8516, https://doi.org/10.1029/2002JD002490, 2003.

Strahan, S. E., Duncan, B. N., and Hoor, P. (2007). Observationally derived transport diagnostics for the lowermost stratosphere and their application to the GMI chemistry and transport model. Atmospheric Chemistry and Physics, 7(9), 2435–2445. https://doi.org/10.5194/acp-7-2435-2007.

Sue et al. 2011: https://doi.org/10.1126/science.1208839

Schultz, M.G., Schröder, S., Lyapina, O., Cooper, O., Galbally, I., Petropavlovskikh, I., von Schneidemesser, E., Tanimoto, H., Elshorbany, Y., Naja, M., Seguel, R., Dauert, U., Eckhardt, P., Feigenspahn, S., Fiebig, M., Hjellbrekke, A.-G., Hong, Y.-D., Christian Kjeld, P., Koide, H., Lear, G., Tarasick, D., Ueno, M., Wallasch, M., Baumgardner, D., Chuang, M.-T., Gillett, R., Lee, M., Molloy, S., Moolla, R., Wang, T., Sharps, K., Adame, J.A., Ancellet, G., Apadula, F., Artaxo, P., Barlasina, M., Bogucka, M., Bonasoni, P., Chang, L., Colomb, A., Cuevas, E., Cupeiro, M., Degorska, A., Ding, A., Fröhlich, M., Frolova, M., Gadhavi, H., Gheusi, F., Gilge, S., Gonzalez, M.Y.,

Gros, V., Hamad, S.H., Helmig, D., Henriques, D., Hermansen, O., Holla, R., Huber, J., Im, U., Jaffe, D.A., Komala, N., Kubistin, D., Lam, K.-S., Laurila, T., Lee, H., Levy, I., Mazzoleni, C., Mazzoleni, L., McClure-Begley, A., Mohamad, M., Murovic, M., Navarro-Comas, M., Nicodim, F., Parrish, D., Read, K.A., Reid, N., Ries, L., Saxena, P., Schwab, J.J., Scorgie, Y., Senik, I., Simmonds, P., Sinha, V., Skorokhod, A., Spain, G., Spangl, W., Spoor, R., Springston, S.R., Steer, K., Steinbacher, M., Suharguniyawan, E., Torre, P., Trickl, T., Weili, L., Weller, R., Xu, X., Xue, L. and Zhiqiang, M., Tropospheric Ozone Assessment Report: Database and Metrics Data of Global Surface Ozone Observations. 2017. Elem Sci Anth, 5, p.58. DOI: 10.1525/elementa.244.

Szopa, S., Naik, V., Adhikary, B., Artaxo, P., Berntsen, T., Collins, W.D., Fuzzi, S., Gallardo, L., Kiendler-Scharr, A., Klimont, Z., Liao, H., Unger, N., and Zanis, P.: Short-Lived Climate Forcers. In *Climate Change 2021: The Physical Science Basis. Contribution of Working Group I to the Sixth Assessment Report of the Intergovernmental Panel on Climate Change* [Masson-Delmotte, V., P. Zhai, A. Pirani, S.L. Connors, C. Péan, S. Berger, N. Caud, Y. Chen, L. Goldfarb, M.I. Gomis, M. Huang, K. Leitzell, E. Lonnoy, J.B.R. Matthews, T.K. Maycock, T. Waterfield, O. Yelekçi, R. Yu, and B. Zhou (eds.)]. Cambridge University Press, Cambridge, United Kingdom and New York, NY, USA, pp. 817–922, doi:10.1017/9781009157896.008, 2021.

Tarasick, D., Galbally, I.E., Cooper, O.R., Schultz, M.G., Ancellet, G., Leblanc, T., Wallington, T.J., Ziemke, J., Liu, X., Steinbacher, M., Staehelin, J., Vigouroux, C., Hannigan, J.W., García, O., Foret, G., Zanis, P., Weatherhead, E., Petropavlovskikh, I., Worden, H., Osman, M., Liu, J., Chang, K.-L., Gaudel, A., Lin, M., Granados-Muñoz, M., Thompson, A.M., Oltmans, S.J., Cuesta, J., Dufour, G., Thouret, V., Hassler, B., Trickl, T. and Neu, J.L., 2019. Tropospheric Ozone Assessment Report: Tropospheric ozone from 1877 to 2016, observed levels, trends and uncertainties. Tropospheric Ozone Assessment Report: Tropospheric ozone from 1877 to 2016, observed levels, trends and uncertainties. Elem Sci Anth, 7(1), p.39. DOI : 10.1525/elementa.376, 2019.

Thompson, A. M., Witte, J. C., Sterling, C., Jordan, A., Johnson, B. J., Oltmans, S. J., Fujiwara, M., Vömel, H., Allaart, M., Piters, A., Coetzee, G. J. R., Posny, F., Corrales, E., Diaz, J. A., Félix, C., Komala, N., Lai, N., Ahn Nguyen, H. T., Maata, M., Mani, F., Zainal, Z., Ogino, S., Paredes, F., Penha, T. L. B., Silva, F. R., Sallons-Mitro, S., Selkirk, H. B., Schmidlin, F. J., Stübi, R., and Thiongo, K.: First Reprocessing of Southern Hemisphere Additional Ozonesondes (SHADOZ) Ozone Profiles (1998–2016): 2. Comparisons With Satellites and Ground-Based Instruments, Journal of Geophysical Research: Atmospheres, 122, https://doi.org/10.1002/2017JD027406, 2017.

Tsivlidou, M., Sauvage, B., Barret, B., Wolff, P., Clark, H., Bennouna, Y., Blot, R., Boulanger, D., Nédélec, P., Le Flochmoën, E., and Thouret, V.: Tropical tropospheric ozone and carbon monoxide distributions: characteristics, origins and control factors, as seen by IAGOS and IASI, Atmos. Chem. Phys. Discuss. (preprint), https://doi.org/10.5194/acp-2022-686, in review, 2022.

Turnock, S. T., Allen, R. J., Andrews, M., Bauer, S. E., Deushi, M., Emmons, L., Good, P., Horowitz, L., John, J. G., Michou, M., Nabat, P., Naik, V., Neubauer, D., O'Connor,

F. M., Olivié, D., Oshima, N., Schulz, M., Sellar, A., Shim, S., Takemura, T., Tilmes, S., Tsigaridis, K., Wu, T., and Zhang, J.: Historical and future changes in air pollutants from CMIP6 models, Atmos. Chem. Phys., 20, 14547–14579, https://doi.org/10.5194/acp-20-14547-2020, 2020.

Theil, H. (1950), "A rank-invariant method of linear and polynomial regression analysis. I, II, III", Nederl. Akad. Wetensch., Proc., 53: 386–392, 521–525, 1397–1412.

Trickl, T., Bärtsch-Ritter, N., Eisele, H., Furger, M., Mücke, R., Sprenger, M., and Stohl, A.: High-ozone layers in the middle and upper troposphere above Central Europe: potential import from the stratosphere along the subtropical jet stream, Atmos. Chem. Phys., 11, 9343–9366, https://doi.org/10.5194/acp-11-9343-2011, 2011.

Verma, S., Yadava, P. K., Lal, D. M., Mall, R. K., Harshbardhan, K., & Payra, S. (2021), Role of Lightning NO_x in ozone formation: A review, Pure and Applied Geophysics, 178, 1425-1443.

Wang, H., Shi, Z., Wang, X., Tan, Y., Wang, H., Li, L., & Lin, X. (2021), Cloud-to-Ground Lightning Response to Aerosol over Air-Polluted Urban Areas in China. *Remote Sens. 13*, 2600. https://doi.org/10.3390/rs13132600

Wang, H., Lu, X., Jacob, D. J., Cooper, O. R., Chang, K.-L., Li, K., Gao, M., Liu, Y., Sheng, B., Wu, K., Wu, T., Zhang, J., Sauvage, B., Nédélec, P., Blot, R., and Fan, S.: Global tropospheric ozone trends, attributions, and radiative impacts in 1995–2017: an integrated analysis using aircraft (IAGOS) observations, ozonesonde, and multi-decadal chemical model simulations, Atmos Chem Phys, 22, 13753–13782, https://doi.org/10.5194/acp-22-13753-2022, 2022.

Wang, Y., A. W. DeSilva, G. C. Goldenbaum, and R. R. Dickerson, (1998) Nitric oxide production by simulated lightning: Dependence on current, energy, and pressure, *J. Geophys. Res.,* 103, 19,149-19,159.

Wilcox, R. (2001). Fundamentals of Modern Statistical Methods: Substantially Improving Power and Accuracy. Springer Science and Business Media.

Williams, R. S., Hegglin, M. I., Kerridge, B. J., Jöckel, P., Latter, B. G., and Plummer, D. A.: Characterising the seasonal and geographical variability in tropospheric ozone, stratospheric influence and recent changes, Atmos. Chem. Phys., 19, 3589–3620, https://doi.org/10.5194/acp-19-3589-2019, 2019.

Wu, D., Zhang, J., Wang, M., An, J., Wang, R., Haider, H., et al. (2022). Global and regional patterns of soil nitrous acid emissions and their acceleration of rural photochemical reactions. Journal of Geophysical Research: Atmospheres, 127, e2021JD036379. https://doi.org/10.1029/2021JD036379

WMO, 1992, International Meteorological Vocabulary (2nd ed.), Geneva: Secretariat of the World Meteorological Organization. 1992. p. 636. ISBN 978-92-63-02182-3)

Wang and Chen, 2012: https://doi.org/10.1016/j.geoderma.2011.11.009

Xue, X., Ren, G. Y., Xu, X. D., Sun, X. B., Yang, G. W., Zhang, P. F., & Zhang, S. Q. (2021), The trends of warm-season thunderstorm and lightning days in China and the influence of environmental factors, J. Geophys. Res., 126 (15), 10.1029/2021JD034950.

Yang, X., and Z. Li, 2014: Increases in thunderstorm activity and relationships with air
pollution in southeast China, *J. Geophys. Res. Atmos.*, 119, 1835–1844,
doi:10.1002/2013JD021224.

Yin, Y., Chevallier, F., Ciais, P., Broquet, G., Fortems-Cheiney, A., Pison, I., and Saunois, M.:
Decadal trends in global CO emissions as seen by MOPITT, Atmos. Chem. Phys., 15,
13433–13451, https://doi.org/10.5194/acp-15-13433-2015, 2015.

Young, P.J., Naik, V., Fiore, A.M., Gaudel, A., Guo, J., Lin, M.Y., Neu, J.L., Parrish, D.D.,
Rieder, H.E., Schnell, J.L., Tilmes, S., Wild, O., Zhang, L., Ziemke, J.R., Brandt, J.,
Delcloo, A., Doherty, R.M., Geels, C., Hegglin, M.I., Hu, L., Im, U., Kumar, R.,
Luhar, A., Murray, L., Plummer, D., Rodriguez, J., Saiz-Lopez, A., Schultz, M.G.,
Woodhouse, M.T. and Zeng, G. Tropospheric Ozone Assessment Report: Assessment
of global-scale model performance for global and regional ozone distributions,
variability, and trends. 2018. Elem Sci Anth, 6(1), p.10. DOI: 10.1525/elementa.265.

Zeng, G., Morgenstern, O., Braesicke, P., Pyle, J.A., 2010. Impact of stratospheric ozone
recovery on tropospheric ozone and its budget: impact of ozone recovery on
tropospheric ozone. Geophys. Res. Lett. 37, n/a-n/a. https://doi.org/10.1029/
2010GL042812.

Yetong Li, Yan Xia, Fei Xie, Yingying Yan, Influence of stratosphere-troposphere exchange
on long-term trends of surface ozone in CMIP6, Atmospheric Research, 297, doi:
https://doi.org/10.1016/j.atmosres.2023.107086, 2024.

Zhang, X., Yin, Y., van der A, R., Lapierre, J. L., Chen, Q., Kuang, X., Yan, S., Chen, J., He,
C., and Shi, R. (2020), Estimates of lightning NO_x production based on high-
resolution OMI NO_2 retrievals over the continental US, Atmos. Meas. Tech., 13,
1709–1734, https://doi.org/10.5194/amt-13-1709-2020 .

Zhang et al., 2020: https://doi.org/10.1016/j.atmosenv.2020.117596

Zhang, L., T. Wang, Q. Zhang, J. Zheng, Z. Xu, and M. Lv (2016), Potential sources of nitrous
acid (HONO) and their impacts on ozone: A WRF-Chem study in a polluted subtropical
region, J. Geophys. Res. Atmos., 121, 3645–3662, doi:10.1002/2015JD024468.

Zheng, B.; Chevallier, F.; Yin, Y.; Ciais, P.; Fortems-Cheiney, A.; Deeter, M.N.; Parker,
R.J.; Wang, Y.; Worden, H.M.; Zhao, Y. Global atmospheric carbon monoxide
budget 2000-2017 inferred from multi-species atmospheric inversions. *Earth Sys. Sci.
Data*, *11*, 1411–1436, https://doi.org/10.5194/essd-11-1411-2019, 2019